Implementation and Algorithm Development of 3D ARFI and SWEI Imaging for in vivo Detection of Prostate Cancer

by

Stephen J. Rosenzweig

Department of Biomedical Engineering
Duke University

Date: ____________________
Approved:

____
Kathryn Nightingale, Supervisor

____
Gregg Trahey

____
G Allan Johnson

____
Brett Byram

____
Wilkins Aquino

____
Rajan Gupta

Dissertation submitted in partial fulfillment of the requirements for the degree of
Doctor of Philosophy in the Department of Biomedical Engineering
in the Graduate School of Duke University
2014

Abstract

Implementation and Algorithm Development of 3D ARFI and SWEI Imaging for in vivo Detection of Prostate Cancer

by

Stephen J. Rosenzweig

Department of Biomedical Engineering
Duke University

Date: __________________________
Approved:

____
Kathryn Nightingale, Supervisor

____
Gregg Trahey

____
G Allan Johnson

____
Brett Byram

____
Wilkins Aquino

____
Rajan Gupta

An abstract of a dissertation submitted in partial fulfillment of the requirements for
the degree of Doctor of Philosophy in the Department of Biomedical Engineering
in the Graduate School of Duke University
2014

Abstract

Prostate cancer (PCa) is the most common non-cutaneous cancer in men with an estimated almost 30,000 deaths occurring in the United States in 2014. Currently, the most widely utilized methods for screening men for prostate cancer include the digital rectal exam and prostate specific antigen analysis; however, these methods lack either high sensitivity or specificity, requiring needle biopsy to confirm the presence of cancer. The biopsies are conventionally performed with only B-mode ultrasound visualization of the organ and no targeting of specific regions of the prostate, although recently, multi-parametric magnetic resonance imaging has shown promise for targeting biopsies. Earlier work has demonstrated the feasibility of acoustic radiation force impulse (ARFI) imaging and shear wave elasticity imaging (SWEI) to visualize cancer in the prostate, however multiple challenges with both methods have been identified.

The aim of this thesis is to contribute to both the technical development and clinical applications of ARFI and SWEI imaging using the latest advancements in ultrasound imaging technology.

The introduction of the Siemens Acuson SC2000™ provided multiple technological improvements over previous generations of ultrasound scanners, including: an improved power supply, arbitrary waveform generator, and additional parallel receive beamforming. In this thesis, these capabilities were utilized to improve both ARFI and SWEI imaging and reduce acoustic exposure and acquisition duration. However,

the SC2000™ did not originally have radiation force imaging capabilities; therefore, a new tool set for prototyping these sequences was developed along with rapid data processing and display code. These tools leveraged the increasing availability of general purpose computing on graphics processing units (GPUs) to significantly reduce the data processing time, facilitating real-time display for ultrasonic research systems.

These technical developments for both acquisition and processing were applied to investigate new methods for ARFI and SWEI imaging. Specifically, the power supply on the SC2000™ allowed for a new type of multi-focal zone ARFI images to be acquired, which are shown to provide improved image quality over an extended depth of field. Additionally, a new algorithm for SWEI image processing was developed using an adaptive filter based on a maximum *a posteriori* estimator, demonstrating increases in the contrast to noise ratio of lesion targets upwards of 50%.

Finally, the optimized ARFI imaging methods were integrated with a transrectal ultrasound transducer to acquire volumetric *in vivo* data in patients undergoing robotic radical prostatectomy procedures in an ongoing study. When the study was initiated, it was recognized that the technological improvements of Siemens Acuson SC2000™ allowed for the off-axis response to the radiation force excitation to be concurrently recorded without impacting ARFI image quality. This volumetric SWEI data was reconstructed retrospectively using the approaches developed in this thesis, but the images were low quality. A further investigation identified multiple challenges with the SWEI sequence, which should be addressed in future studies. The ARFI image volumes were very high quality and are currently being analyzed to assess the accuracy of ARFI to visualize prostate anatomy and clinically significant prostate cancer tumors. After a blinded evaluation of the ARFI image volumes for suspicion of prostate cancer, three readers correctly identified 63% of all clinically significant tumors and 74% of clinically significant tumors in the posterior region,

showing great promise for using ARFI in the context of prostate cancer visualization for targeting biopsies, focal therapy, and watchful waiting.

I would like to dedicate this dissertation to my family.

Contents

List of Tables

List of Figures

List of Abbreviations and Symbols

Symbols

c_o speed of sound

ρ material density

Z acoustic impedance

$\mathbf{F}$ Acoustic radiation force

$\mathbf{I}$ Temporal average acoustic intensity.

α Acoustic amplitude attenuation coefficient

λ Ultrasound wavelength

f_c Center frequency

BW Fractional bandwidth of ultrasound transducer

F F/# of focal configuration ($F = \frac{z}{D}$)

z Focal depth

D Aperture size

c Acoustic or compressional wave speed

$\mathbf{u}$ Displacement

ϵ Strain

σ Stress

E Young's modulus

c_s Shear wave speed.

μ Shear modulus

Abbreviations

US	Ultrasound
ARFI	Acoustic radiation force impulse
SWEI	Shear wave elasticity imaging
CEUS	Contrast-enhanced ultrasound
PA	Photoacoustic
IQ	In-phase and quadrature
RF	Radio-frequency
MBM	Motherboard module
RTC	Real time controller
ASIC	Application specific integrated circuit
FPGA	Field programmable gate array
CPU	Central processing unit
GPU	Graphics processing unit
CUDA	Compute unified device architecture
MP	Multi-processor
SM	Shared memory
PTZ	Lead zirconate titanate
FOV	Field of view
ROE	Region of excitation
ROI	Region of interest
DOF	Depth of field
DDG	Depth dependent gain
TGC	Time gain compensation
PRF	Pulse repetition frequency
PRI	Pulse repetition interval

MI	Mechanical index
TI	Thermal index
TRUS	Transrectal ultrasound
PCa	Prostate cancer
BPH	Benign prostatic hyperplasia
PZ	Peripheral zone
CZ	Central zone
TZ	Transition zone
CG	Central gland
DRE	Digital Rectal Exam
PSA	Prostate specific antigen
MRI	Magnetic resonance imaging
mpMRI	Multi-parametric MRI
DCE	Dynamic contrast enhanced
DWI	Diffusion weighted imaging
ADC	Apparent diffusion coefficient
MRE	Magnetic resonance elastography

Acknowledgements

First and foremost, I would like to thank Kathy for her guidance and support throughout my tenure both as an undergraduate and as a graduate student in her lab. She granted me my start in research and has continued her support of my work and development throughout the ups and downs of my graduate school career, for which I will always be grateful. I would also like to thank the other members of my committee, Gregg, Al, Brett, Wilkins, and Raj for their insights as I have worked toward this dissertation and for their honest comments when I meandered down incorrect paths.

I would also like to thank Mark Palmeri for all the valuable insights on research as well as intermittent conversations about growing up on Long Island and life when it seemed as I might be a Duke student forever. I would like to thank Ned Rouze as well for his calm demeanor and focused approach to research as well as his attention to detail. Additionally, I would like to thank Ned as he provided the insight and inspiration for a significant portion of this dissertation.

I would like to express my gratitude to all of the clinical collaborators that I worked with during my time as a graduate student, in particular, Dr. Thomas Polascik for his patience in the operating room as we acquired patient data before his surgeries and especially when we had equipment failures. Additionally, this dissertation would not have been completed without the entire prostate imaging team including multiple radiologists, pathologists, and the entire OR team of doctors, nurses, and staff.

There are also many mentors and students that I would like to thank for their advice, technical expertise, and other help. My officemates, Kristin Bing, David Bradway, Veronica Rotemberg, and Seung Lee have demonstrated an incredible bandwidth for tolerating my interruptions and have been invaluable in making each day at work enjoyable. Thank you also to the other members of the Wolf, Trahey, and Nightingale labs for their support and for the day to day interactions that provided levity to the otherwise, sometimes mundane grind.

I would also like to thank all the members of the BME department administration, in particular Kathy Barbour, Joyce Franklin, and Susan Story-Hill, for all their help in filing paperwork, travel reimbursement, obtaining department funding, as well as planning department events and providing a fantastic work environment during my time as a graduate student.

I would like to acknowledge NIH grants T32-EB-001040, 2R01-EB-002132, and 1R01-CA142824 for funding my graduate studies, as well as the James B. Duke and Thurstone Medical Imaging Fellowships for providing additional assistance. I would like to thank Siemens Healthcare in Mountain View, CA for a valuable internship experience during my graduate studies.

Lastly, I am incredibly grateful for the support and encouragement I received from my parents, and I would like to thank all of my family and friends for their words of inspiration and encouragement.

1

Introduction

This chapter has been published in the book Imaging and Focal Therapy of Early Prostate Cancer*, and is reproduced here with kind permission of Springer Science + Business Media.*

Rosenzweig, Stephen, Liang Zhai, and Kathryn R. Nightingale. "Prostate Elastrography." Imaging and Focal Therapy of Early Prostate Cancer*. Humana Press, 2013. 165-172.*

1.1 Clinical Importance of Prostate Cancer Detection

Prostate cancer (PCa) is the most common non-cutaneous cancer in men with an estimated 233,000 new cases and 29,480 deaths occurring in the United States in 2014 [1]. Currently, the most widely utilized methods for screening men for prostate cancer include the digital rectal exam (DRE) and prostate specific antigen (PSA) analysis, neither of which have high sensitivity or specificity [77]. Although an abnormal DRE or PSA screening test raises the level of suspicion for prostate cancer, needle biopsies are required to detect the presence of cancer.

To visualize the prostate gland and needle during biopsy, B-mode transrectal ultrasound (TRUS) is used extensively; however, TRUS has limited sensitivity and specificity for prostate cancer detection [69, 25]. Without any ability to target, 6-12 cores are removed from the prostate in a systematic fashion, however, this results in a high rate of false negatives since the organ is insufficiently sampled, also causing future repeated biopsies [77]. Therefore, there are multiple imaging modalities currently being investigated in order to help visualize the cancer and potentially guide TRUS biopsies including advanced methods in both magnetic resonance imaging (MRI) and ultrasound (US).

Generally, cancer has increased vascularity as compared to the surrounding tissue, and therefore, multiple studies have investigated using either color or power Doppler imaging in conjunction with standard B-mode TRUS during biopsy [69, 25, 52]. Although some of the studies showed improved sensitivity or specificity, they concluded that performing guided biopsies with Doppler imaging could not replace standard 6 or 12 core biopsies [69, 52, 49].

Similar to using Doppler ultrasound to visualize increased blood flow, contrast-enhanced ultrasound (CEUS) is currently under evaluation to determine its utility to detect prostate cancer. CEUS involves injecting microbubbles into the vasculature then utilizing specialized ultrasonic pulse sequences to localize the bubbles. Studies have shown that guided biopsies targeting regions of increased microbubble density have a higher yield than systematic biopsy [65, 104, 46].

Another characteristic of prostate cancer is a change in the cell structure, which can cause a change in the backscatter characteristics of the ultrasound signal. By analyzing the radio-frequency spectrum of the received data on a calibrated system, it is possible to detect these changes in the backscatter echoes [57]. Recent work has focused on using more advanced methods of detecting these changes, such as artificial neural networks that account for multiple parameters, which have yielded very promising results. [39, 40, 41]

An ultrasound-based imaging modality that has the potential to take advantage of both the increased blood density and the cell structure changes is photoacoustic (PA) imaging, which utilizes laser light to excite the tissue and a standard TRUS transducer to detect the resulting photoacoustic signal [45, 76]. PA imaging can provide spectroscopic images to assess blood content and oxygenation state [114] and to monitor changes in cell structure and growth in prostate cancer by using targeted nano-scale contrast agents [55].

In addition to increased blood flow and cell structure changes, prostate cancer normally presents as stiffer than the surrounding tissue; the digital rectal exam (DRE) has traditionally been utilized to detect this change in stiffness to diagnose prostate cancer [48, 118]. Ultrasound elastography generates qualitative or quantitative stiffness images, allowing for detection of stiff regions throughout the entire gland. Recent advancements in commercially available elastography tools have encouraged many studies, most of which demonstrated significant increases in sensitivity and specificity (60-90%) for cancer detection [87, 25, 79].

1.2 Prostate Anatomy and Common Pathology

Before detailing the methods for imaging the prostate, it is necessary to review typical prostate anatomy and pathology. The prostate has a complex structure including three primary zones as well as ductal structures traversing the organ as seen in figure 1.1. The prostate is divided into the peripheral zone (PZ), which is the most posterior region of the prostate, the transition zone (TZ), and the central zone (CZ), which is the most anterior region; the combination of the TZ and CZ can also be referred to as the central gland (CG). The prostate also contains the urethra, which runs through the entire prostate, and the ejaculatory ducts, which originate in the seminal vesicles and join the urethra at the verumontanum.

The anatomic zones are clinically important as pathologies such as benign prostatic hyperplasia (BPH), atrophy, inflammation, and prostate cancer (PCa) preferentially occur in different zones. For prostate cancer, most (75-80%) occur in the PZ [5, 63]; however, BPH nodules predominantly develop in the central gland and lead to an increase in the size of the TZ [29].

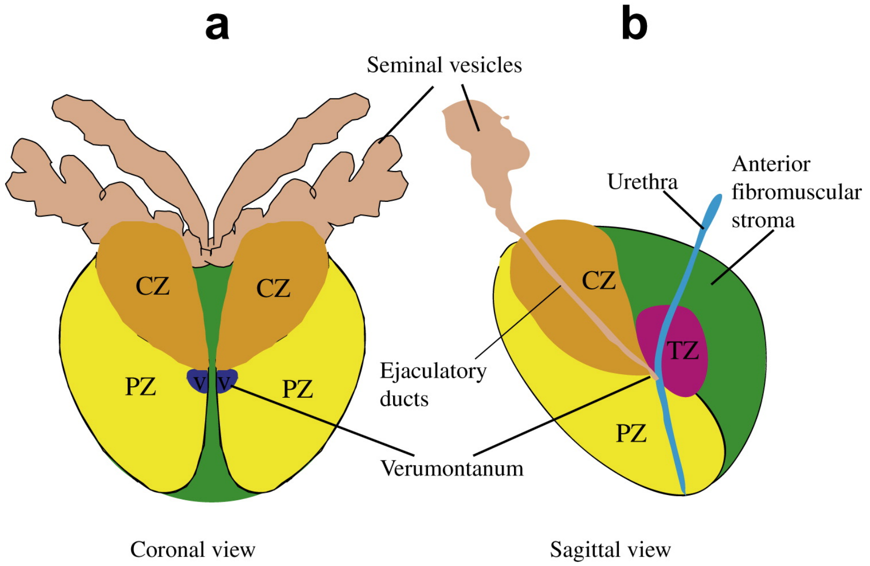

FIGURE 1.1: Zonal anatomy of the prostate, which contains 3 distinct anatomic zones: the peripheral zone (PZ), transition zone (TZ), and central zone (CZ); combined, the central zone and transition zone can also be referred to as the central gland (CG). Additionally, the urethra and ejaculatory ducts both run through the prostate and join at the verumontanum. *Figure reproduced with permission from [119].*

1.3 Current State of the Art Elastography Methods

The digital rectal exam (DRE) is used extensively to diagnose prostate cancer; however, this technique is limited to palpation of the posterior region of the prostate. Elastography extends the idea of palpation by portraying stiffness variations throughout the tissue. Elastographic imaging techniques introduce a mechanical excitation and use either MRI or ultrasound to monitor the tissue response, thereby creating an image of the tissue stiffness. Elastographic methods that have been used to visualize structures in the prostate are strain imaging [52, 67, 79, 34], acoustic radiation force impulse (ARFI) imaging [117, 119, 118, 121], shear wave imaging [120, 4], vibration elastography imaging [96, 59], and vibration amplitude sonoelastography [20, 48, 106].

Although there are a multitude of elastographic techniques, they are all based on the same concept of applying a force and imaging the resulting tissue response. Common forces include compressing the tissue, using a vibrating piston or other mechanical actuator, or using acoustic radiation force. The tissue response has been monitored with both ultrasound and magnetic resonance imaging (MRI). The induced tissue deformation, or displacement, is related to the mechanical properties of the tissue through the principles of elasticity. There are two general types of elastographic images, qualitative and quantitative. Qualitative images portray the relative stiffness, strain, or displacement response of the tissue, whereas quantitative images utilize the principles of elasticity to derive the underlying elastic material properties of the tissue. The quality of the images depends on the imaging modality being used, the magnitude and type of force being applied, the signal processing of the data, and the validity of the assumptions used to reconstruct the images.

1.3.1 Governing Principles of Elasticity

To appreciate elastography images and the data that they contain, a brief overview of the governing principles of elasticity is necessary. Elastographic imaging methods measure the displacement (u), or strain (ϵ), of the tissue in response to an applied force (or stress, σ). The strain is the spatial gradient of the displacement ($\epsilon = \frac{du}{dx}$), and represents the change in displacement with depth (i.e., how tissue compresses). Strain is related both to the applied stress (σ, i.e. force per unit area) and the inherent tissue mechanical properties (E, the elastic, or Young's modulus), and under

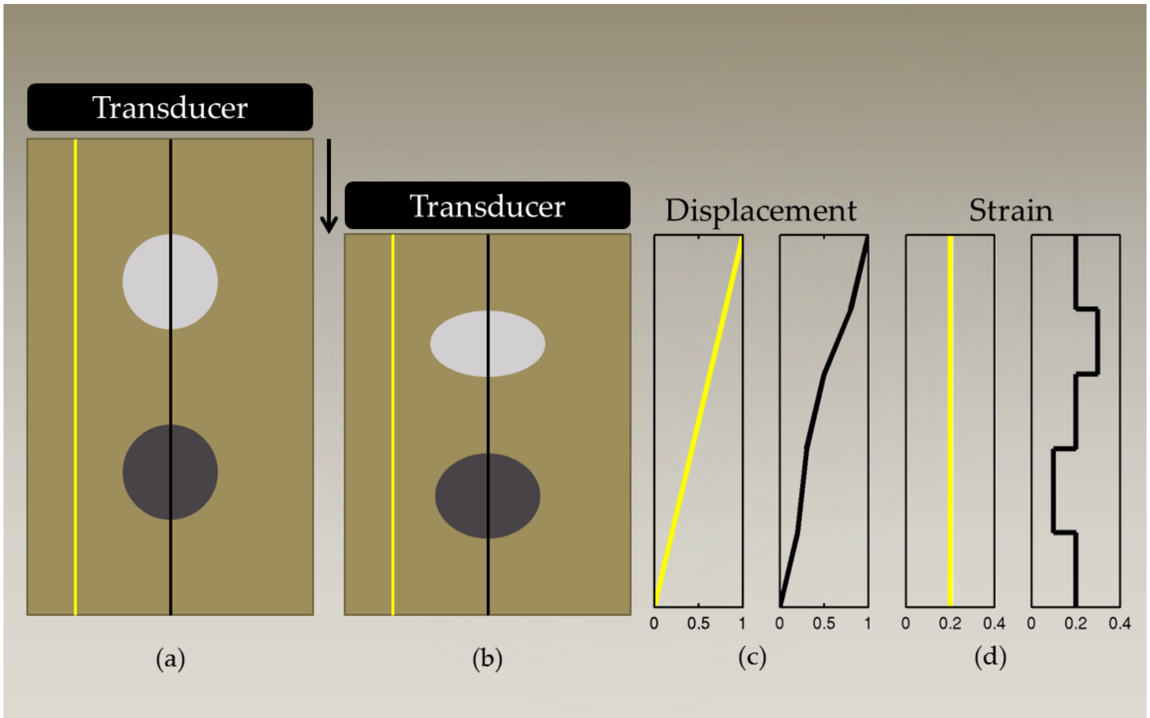

FIGURE 1.2: Schematic representation of tissue with a soft circular inclusion (top, light gray) and stiff circular inclusion (bottom, dark gray) prior to compression (a), post-compression (b), the induced displacements (c), and the computed strain (d). The background has linearly varying displacement throughout depth due to the applied force at the top of the tissue and fixed bottom boundary; thus, the background has constant strain, as represented by the yellow line. The displacement in the region with the two inclusions is piecewise linear, with different slopes in the lesions and the background. The soft lesion displaces more than the background and the stiff inclusion displaces less than the background; thus, the strain provides information about the relative stiffnesses of the lesions and background.

simplifying assumptions is described by the equation:

$$\epsilon = \frac{\sigma}{E} \tag{1.1}$$

The elastic modulus describes the stiffness of tissue; stiffer tissues have a higher elastic modulus than softer tissues. Since strain is inversely proportional to the elastic modulus, for a given stress, stiffer structures exhibit smaller strain, or displacement, and softer tissues exhibit larger strains (figure 1.2). Both MRI and ultrasound can be used to measure tissue motion, thus, in elastographic imaging methods, tissue displacement in response to an applied stress is measured, and, images of tissue displacement or strain are generated that reflect relative differences in tissue stiffness.

In addition to compressing the tissue, it is possible to generate shear waves in the tissue. These shear waves propagate in a direction orthogonal to the applied stress and are in concept similar to the ripples that propagate away from a pebble dropped in water. The spatial and temporal behavior of a shear wave in tissue is governed by the wave equation:

$$\nabla^2 \mathbf{u} = \frac{1}{c_s^2} \frac{\partial^2 \mathbf{u}}{\partial t^2} \tag{1.2}$$

where u is the displacement of the tissue, c_s is the wave speed, and ∇ is the Laplacian operator.

Equation 1.2 relates the spatial behavior of the wave, the left side of the equation, to the temporal behavior of the wave, the right side of the equation. Additionally, there is a constant of proportionality, c_s, which is known as the shear wave speed. The shear wave speed can be related to the shear modulus through assumptions of linear elasticity and homogeneity, such that $\mu = \rho c_s^2$, where μ is the shear modulus and ρ is the density. Furthermore, under the assumption of incompressibility, which is considered reasonable in soft tissues such as the prostate, the shear modulus is directly proportional to the Young's modulus, such that $E = 3\mu = 3\rho c_s^2$. Therefore, if the shear wave speed is measured using elastographic techniques, it is possible to directly estimate the corresponding shear and Young's moduli, which represent the inherent material elastic properties of the tissue.

1.3.2 Elastic Properties of the Prostate

In addition to empirical evidence that prostate cancer is stiffer than normal prostate tissue (i.e., the digital rectal exam), multiple studies have been published that quantify the stiffness. Zhang et al. performed a study on *ex vivo* prostates and found that the Young's moduli of normal posterior and cancerous prostatic tissue were $15.9 \pm 5.9 kPa$ and $40.4 \pm 15.7 kPa$, respectively [122]. Zhai et al. utilized quantitative shear wave based elastography methods in *ex vivo* samples and reported that the Young's moduli of normal peripheral zone and cancerous prostatic tissues were $12.3 \pm 2.4 kPa$ and $30 \pm 3.0 kPa$, respectively [120]. Although the stiffness differed between the studies, both found that there is approximately a 2.5× increase in the stiffness of the cancerous regions as compared to the prostatic peripheral zone tissue.

1.3.3 Elastographic Methods in Prostate

Strain Imaging

The vast majority of prostate elastography clinical studies have employed strain imaging (i.e., compression elastography) because this method is commercially available [52, 24, 66, 69, 77, 87, 97, 109]. Strain imaging requires the user to obtain a B-mode image of the prostate, then compress the organ and obtain a second B-mode image. The tissue displacement is estimated using correlation based techniques and the strain between the two states is then computed [87, 75].

Strain imaging assumes that the operator applies a uniform stress across the prostate. Stiffer regions can then be identified by their relatively low strain compared to the surrounding tissue as shown in figure 1.2. Elastography is typically performed as a free-hand technique with the operator gently compressing the prostate with the ultrasound transducer. A skilled technician is needed to obtain adequately uniform compression, which can be challenging. Some recent studies have used inflatable balloons that surround the endorectal transducer and can be filled or emptied by the operator, thereby generating a more uniform stress on the prostate [87, 53, 108].

Researchers have also investigated the potential use of strain imaging to obtain quantitative information about the tissue. To accomplish this, the inverse problem is solved using models of the tissue structure and displacement data. While this method holds promise it has not been used clinically to date due to challenges with implementation [6, 38].

Transrectal ultrasound (TRUS) is widely used for visualization during systematic prostate biopsies, but it is not typically used for biopsy guidance since tumors may not be visualized [78]. The primary use of strain imaging investigated in the clinical literature is for biopsy guidance. As will be reviewed below, many studies have employed conventional biopsy techniques, and then used elastography to identify and target additional regions [52, 24, 66, 69, 109, 53]. Some studies have acquired elastography data and retrospectively compared suspicious regions with those that were biopsied [79] or with whole-mount histology after the prostate is excised [97].

Cochlin et al. demonstrated a significant improvement using strain imaging as compared to TRUS for prostate cancer (PCa) biopsy guidance. The authors studied 100 patients and using elastography identified five cancers that would not have otherwise been biopsied. Additionally, of these five cancerous regions, three were in patients whose other biopsies showed no cancer, thus cancer detection was only achieved through the use of elastography. For elastography, the reported sensitivity and specificity for PCa were 51% and 83%, respectively. [24]

Nelson et al. in 2007 studied targeting biopsies using TRUS, color Doppler, and elastography in addition to the traditional sextant biopsy. The authors concluded that color Doppler and elastography both improve cancer detection, but that the detection is not sufficient to replace the standard sextant biopsy. Additionally, the authors showed that cancer detection in gray scale ultrasound, color Doppler, and elastography images are all correlated with Gleason score. [69]

Kamoi et al. studied 107 patients using both power Doppler ultrasound and elastography, indicating that elastography had 68% sensitivity and 81% specificity for PCa. The authors report that elastography is more successful at detection of high Gleason score tumors, with 100% of the tumors with a Gleason score $\geqslant 8$ being detected. The authors indicated that their primary difficulty with elastography was the image quality variability between users due to the user-dependent nature of compression. [52]

Although the previous studies used both Doppler ultrasound and strain imaging, other groups have evaluated exclusively strain imaging. A 311 patient study by Miyagawa et al. reported a 90% diagnostic sensitivity for PCa using the combination of TRUS and elastography. The authors reported that elastography was most successful in detecting cancer in the anterior prostate. They also noted that the sensitivity of elastography decreased as prostate volume increased, which they attributed to the confounding effects of BPH. [66]

The observation that the diagnostic utility of elastography differs in various regions of the prostate was expanded upon by Tsutsumi et al. The authors divided the prostate into three regions, anterior, middle, and posterior and analyzed the utility of elastography for prostate cancer detection. While elastography improved cancer detection in all regions of the prostate, the largest benefit was seen with anterior tumors, with decreasing improvement for middle and posterior tumors. [109]

Pallwein et al. studied 492 patients, who had elastograms of the prostate recorded prior to receiving a systematic 10 core biopsy. The urologist performing the biopsy was blinded to the results of the elastography study. The authors found a whole organ sensitivity of 86% and specificity of 72% in the retrospective analysis of suspicious regions in the elastograms. Cancer detection in the basal region was compromised due to high false positive rates associated with chronic inflammation and atrophy. A representative series of elastograms is reproduced from their work in figure 1.3. [79]

Kapoor et al. performed a 50 patient study specifically focused on determining the utility of elastography in targeting biopsies. The authors reported the sensitivity and specificity of 91.7% and 86.8%, respectively, as compared to their reported sensitivity

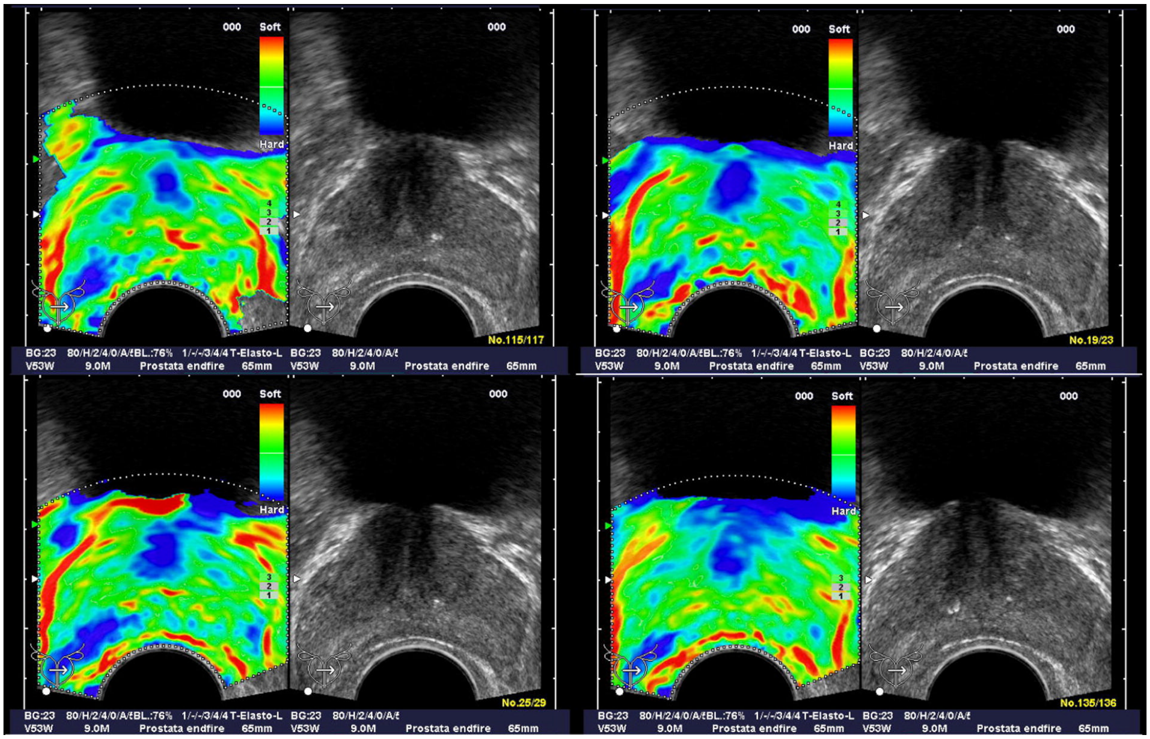

FIGURE 1.3: Patient (picture series) with histologically confirmed prostate cancer in the right mid-gland of prostate. The elastographic examination showed a well-defined lesion with low strain (dark blue). The peripheral zone on the patient left side showed normal stiffness. *Figure reproduced with permission from [79].*

and specificity of TRUS: 16.7% and 89%, respectively. They noted that the primary challenges in using elastography are the inability to differentiate between cancer and prostatitis, very large prostates, and lack of operator experience. [53]

Salomon et al. studied prostate elastography in 109 patients undergoing radical prostatectomy, in which the pre-operative elastography data was correlated with whole mount histology data. The authors reported 75% sensitivity and 77% specificity for elastography. The authors found that elastography detection of PCa was positively correlated with Gleason score. [97]

One of the common challenges reported for strain imaging of the prostate is achieving uniform compression of the organ. To address this challenge, Tsutsumi et al. inflated a water balloon surrounding the transducer to compress the tissue, which reduced the operator-dependence of the image quality. Using this method, the authors detected 71% of histology confirmed prostate cancer lesions. [108]

Overall, the multitude of studies performed using strain imaging has demonstrated great promise for guidance of targeted biopsies. The primary benefits have been reported for detecting PCa in the peripheral zone, where approximately 80% of cancers are located [78]. Although the studies have demonstrated higher sensitivity than with TRUS alone, challenges have also been identified. The studies using free hand compression noted that an experienced operator was needed to obtain high quality images. Additionally, many studies demonstrated a high false positive rate due to the confounding effects of BPH, which looks similar to cancer in strain images. Finally, the studies determined that targeted biopsies are not sufficient and that standard sextant or 10-core biopsies are necessary in addition to elastography-targeted biopsies.

Acoustic Radiation Force Impulse (ARFI) Imaging

Although strain imaging has been the most widely used elastographic imaging technique in the prostate to date, many other methods are currently under investigation. One promising area is the use of an acoustic radiation force impulse (ARFI) excitation rather than transrectal compression. The primary benefit of ARFI excitation is the ability to apply the force directly within the tissue, reducing the operator dependence of image quality [107].

ARFI imaging applies short duration ($< 1ms$) focused ultrasound pushing pulses that displace the tissue on the order of $10\mu m$; the displacement response is then measured with the same ultrasonic transducer. Regions of decreased displacement are assumed to represent stiffer tissues in the same way that regions of decreased strain represent stiffer tissues in strain imaging. [72]

ARFI imaging has been used in preliminary feasibility studies to detect prostate

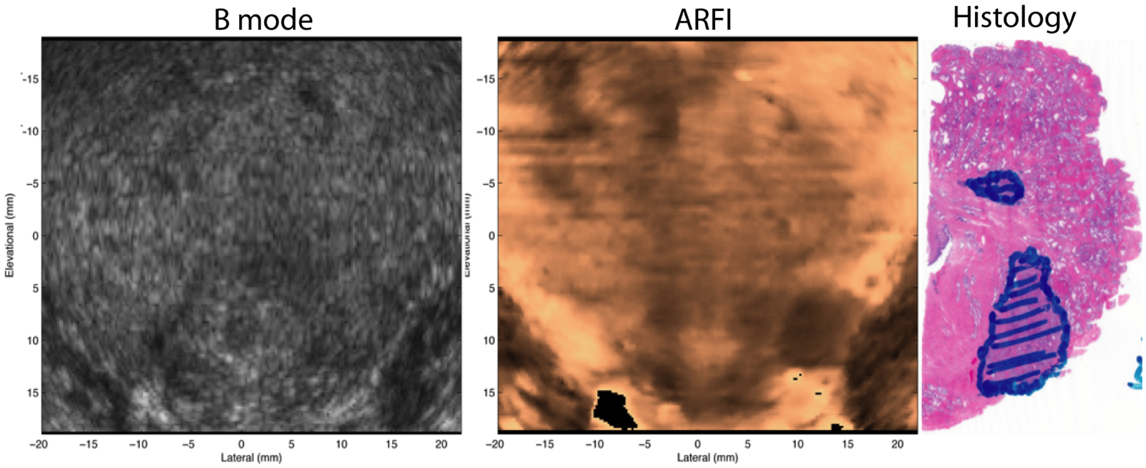

FIGURE 1.4: Co-registered coronal sections of B-mode, ARFI images *in vivo* and the right half histological slide. The basal area of the prostate is at the top of the images, and the apex is at the bottom. Images were obtained in vivo immediately prior to radical prostatectomy surgery. In the histological slide, cancerous regions were masked in blue by a pathologist. The stiff structure in the right apex region shown in the ARFI image corresponds to the cancerous lesion. The Gleason's scores are 4+3. *Figure reproduced with permission from [117].*

cancer. Zhai et al. have acquired three-dimensional volumes of ARFI data and correlated their results to whole mount histology in both ex vivo and in vivo studies. The initial ex vivo studies demonstrated that ARFI images portrayed zonal anatomy, BPH, and prostate cancer with considerably higher contrast than matched B-mode images [119].

In a follow-up study of 19 patients, the same group acquired three-dimensional volumes in vivo using an end-fire endocavity transducer prior to radical prostatectomy. The images were then correlated with histologic results. As with strain imaging, when visible, cancers appeared as stiffer regions, corresponding to decreased displacement in the ARFI images. In addition, regions of BPH within the central gland were well visualized with a nodular appearance. Representative ARFI images and corresponding histology slide are shown in figure 1.4. [117, 121]

Shear Wave Elastography

Shear wave imaging is an elastography technique in which the tissue stiffness is interrogated by exciting a shear wave and monitoring the speed of propagation away from the excitation, thus obtaining c_s, as given in equation 1.2. To generate a shear wave *in vivo*, acoustic radiation force impulse excitations are used, either with a single focus or in a multi-focal 'supersonic' configuration [10]; an image of the tissue is then generated by estimating the shear wave speed in small regions that are assumed to be uniform [87].

Although shear wave imaging has been used to image the breast [105], muscles [42], and liver [68], it has only recently been translated to imaging prostates *in vivo* [25]. In a single-center study, Ahmad et al. imaged and biopsied 50 patients, 33 of which had at least one positive biopsy core. Based on this work, they found that cancer was approximately 50% stiffer than the benign tissue and that they were able to detect cancer with high sensitivity and specificity (0.9 and 0.88, respectively). [4]

Vibro-Elastography

Vibro-elastography is an elastography technique that uses external vibratory actuators to excite the tissue at many frequencies simultaneously. The displacement of the tissue is then monitored using ultrasound and the biomechanical properties of the tissue are calculated from the induced displacement. This method is equivalent to a strain image, but is calibrated to the frequency and amplitude of motion, and therefore it can be used to obtain quantitative values for stiffness, density, and viscosity. [110]

Vibro-elastography has been used in a pilot study by Salcudean et al. to demonstrate the potential utility in detecting prostate cancer and brachytherapy seed placement. The tissue is excited using a mechanical actuator coupled to a transrectal ultrasound transducer to generate displacements within the tissue, which are subsequently observed using correlation based techniques. The authors showed the ability to generate repeatable, operator independent images that revealed stiff regions in the prostates they studied. [96, 59]

Vibration Amplitude Sonoelastography

Another ultrasound based elastographic method that has been used to evaluate prostate cancer in vivo is vibration amplitude sonoelastography. Two external mechanical actuators positioned beneath the patient's pelvis vibrate at low frequency (70-200 Hz) generating vibrations within the prostate. These vibrations are monitored using a specially designed ultrasound Doppler processing mode. Regions of decreased amplitude are associated with stiffer structures in the tissue. [20, 48, 106, 87]

Castaneda et al. imaged 10 patients prior to radical prostatectomy and correlated the results with whole mount histology. Twelve of 19 cancerous lesions were identified (average diameters: 7.4mm visualized, 3.8 mm missed), and 12 false-positive regions were identified, 6 of which corresponded to BPH. The primary challenges associated with this method are the inability to detect small tumors and difficulty in coupling enough vibration energy into the tissue. [20, 48]

1.4 Thesis Outline

Empirical evidence and quantitative experiments have demonstrated that cancerous regions in the prostate can be stiffer than healthy tissue. Reports generally indicate improved sensitivity (70-90%) and specificity (72-87%) for prostate cancer as compared to TRUS alone using compression elastography. However, several challenges have been identified, including: operator dependent image quality; difficulty in differentiating between BPH, prostatitis, atrophy, and prostate cancer; reduced image quality in larger prostates; and limitations of cancer sensitivity in the basal region of the prostate. Therefore, techniques such as ARFI and SWEI, which have the potential to overcome some of these challenges, are under development.

This thesis presents work developing new methods and algorithms for improved ARFI and SWEI imaging with the clinical goal of improved visualization of prostate cancer. The Siemens Acuson SC2000™ was chosen for the work in this thesis because of its technological improvements over previous generations of scanners, specifically its increased parallel receive capabilities, improved power supply and arbitrary waveform generator.

In chapter 2, background information on ultrasound scanners and ultrasonic imaging is provided, with an emphasis on radiation force image sequencing and data processing. Radiation force based modalities, such as ARFI and SWEI, have been implemented on multiple commercial ultrasound platforms [9, 11]; however, these modalities are not commercially available on the SC2000™. Thus, chapter 3 details the creation and validation of a tool set for prototyping radiation force sequences on the SC2000™, with the goal of supporting the development of new methods and algorithms for ARFI and SWEI.

Given the parallel receive capabilities as well as higher sampling frequencies used by the SC2000™, significant data processing and throughput challenges exist. Therefore, chapter 4 describes the development and implementation of real-time displacement estimation and ARFI image generation through the use of general purpose computing on graphics processing units (GPUs).

Utilizing the radiation force prototyping tools and GPU processing methods, an investigation into improved ARFI and SWEI methods was performed. Specifically, in chapter 5, a new method for multi-focal zone ARFI imaging was investigated and analyzed for its impacts on image quality. Chapter 6 then investigates improving SWEI image quality by utilizing an adaptive filter to reduce the noise present in SWEI images, therefore allowing the use of smaller reconstruction kernels.

These new ARFI and SWEI methods and algorithms are then utilized in chapter 7 to develop an *in vivo* 3D radiation force based prostate imaging system. Patients expecting robotic radical prostatectomy were imaged with the system, and the ARFI image volumes are currently being compared with histopathologic data to assess the accuracy of ARFI to visualize prostate anatomy and clinically significant prostate cancer tumors.

Finally in Chapter 8, the work presented in this thesis is summarized and future directions are outlined.

2

Background

2.1 Ultrasound Imaging

Ultrasound imaging systems utilize high frequency (500 kHz - 50 MHz) acoustic waves to image tissue material properties. A brief flowchart of a typical ultrasound system is given in figure 2.1 demonstrating the primary components of the system: digital control, transducer, transmit (high-voltage) circuitry, receive (low-voltage) circuitry, digital beamforming, imaging processing, and display.

In most modern ultrasound scanners, the digital control is split into two parts: a motherboard module (MBM) is used for the high-level digital control of the ultrasound system, and a separate real time controller (RTC) interacts with the low-level circuitry. The MBM is typically a desktop computer that coordinates the software and hardware, managing the interactions required to tell the hardware what to do and retrieving data from the receive circuitry. Additionally, the MBM also contains powerful central processing units (CPUs) and graphics processing units (GPUs) to allow for advanced image processing algorithms. The RTC can be either an application specific integrated circuit (ASIC) or a field programmable gate array (FPGA)

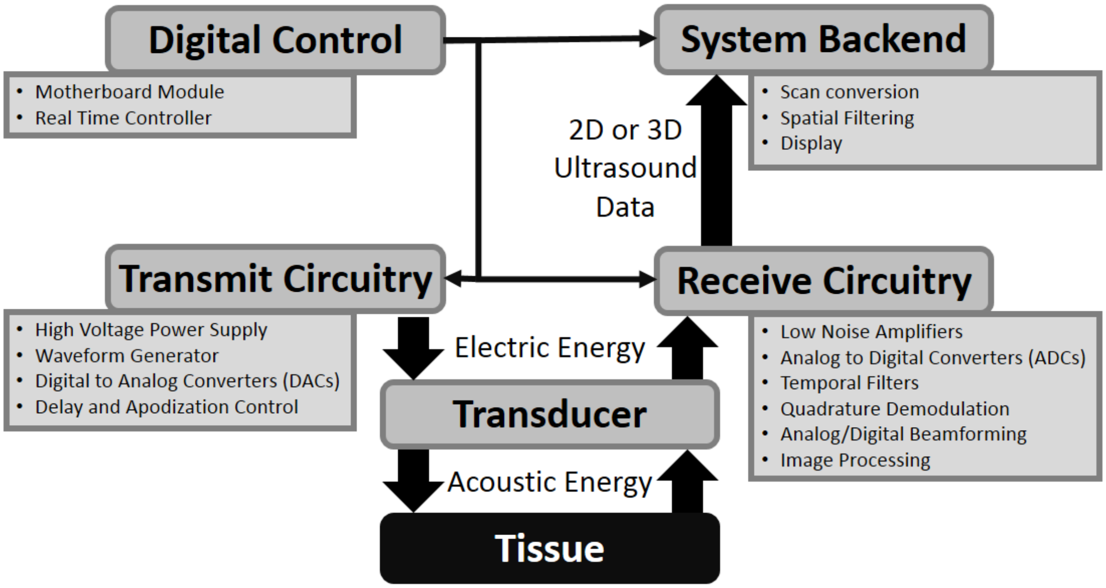

FIGURE 2.1: Flowchart of an example ultrasound system demonstrating the 4 primary system components: digital control, transmit circuitry, receive circuitry, and backend, as well as the transducer, which converts between electric and acoustic energy. Each of the system components is broken down into its main constituents and the general flow of control information and data are shown as well. The digital control specifies instructions for all of the other pieces of the system. To generate an image, after receiving its instructions, the transmit circuitry sends high voltage electric signals to the transducer, which converts it into acoustic energy that is transmitted into the tissue. The tissue scatters some of the acoustic energy back, which is then converted back into electric energy, again by the transducer. These electronic signals are processed by the receive circuitry into 2D or 3D ultrasound data, including: B-mode, Doppler, M-mode, and elasticity data, which are then transferred to the backend for scan conversion, additional spatial filtering, and display.

and performs the low-level hardware functions such as transducer control, thermal monitoring, analog-to-digital conversion (ADC), digital-to-analog conversion (DAC), and timing control.

The ultrasound transducer is a complex piece of technology that converts signals between acoustic and electric energy. Most diagnostic ultrasound transducers are made with lead zirconate titanate (PZT), which is a piezoelectric material that has good characteristics for the two-way conversion between acoustic and electric energy.

Modern diagnostic transducers have multiple different sizes and shapes depending on their purpose, including: linear, curvilinear, and phased; additionally, the transducers can be 1-D (single row of elements), 1.25-D (multiple rows of elements, but no independent delay control), 1.5-D (multiple rows of elements with delay control, but always centered about the elevation aperture), or 2-D (matrix transducer with fully independent delay and apodization control) [115].

The primary components of the transmit circuitry are a high voltage (upwards of 250 V peak-to-peak) function generator and individual transducer channel control. Depending on the complexity, and thus associated cost, of the ultrasound scanner, the function generator could be as simple as only being able to output square waves at a certain modulation frequency or as complicated as an arbitrary waveform generator including the ability to generate amplitude- and phase-modulated sinusoids, chirps, and coded excitations. The individual transducer channel control needs to account for transmit delays and apodization; thus it needs to be able to time-delay the transmit pulse for each channel as well as modulate the amplitude of the transmit for apodization.

The receive circuitry must be isolated from the transmit circuitry since the received signals are relatively low voltage. The receive circuitry is comprised of low-noise amplifiers, analog-to-digital converters (ADCs), analog and digital beamformers, and digital imageformers. Ideally, each receive channel would have its own dedicated amplifier and ADC, which would then pass the data to software, however, this generates a large amount of data. For example, a standard 192 channel transducer and 40 MHz digitization with 12-bit ADCs would generate over 10 GB of data per second, which provides challenges in downstream data processing, although modern peripheral component interconnect express (PCIe) buses can handle the data throughput. Therefore, the typical receive circuitry uses ASICs to preform beamforming to reduce the channel count as well as convert the radio frequency (RF) signal to in-phase and quadrature (IQ) data at baseband, allowing for a much lower sampling frequency. Additional data processing such as Doppler processing, B-mode detection, or image filtering can also be applied using ASICs or FPGAs in the receive circuitry.

After all of the data has been processed by the receive circuitry, it is transferred to software via a direct memory access (DMA) interface, of which PCIe is an example, for additional image processing and display. The backend of the ultrasound system typically performs spatial filtering and scan conversion based on the transducer and scan geometry. Additionally, the user interface and display software are contained within the backend, allowing for the concurrent visualization of multiple imaging modes such as B-mode, Doppler, M-mode, and elasticity imaging, as well as the ability to modify display parameters to obtain the best image possible.

2.2 B-Mode Imaging

All ultrasound imaging utilizes sound from the transducer, which propagates through tissue as a longitudinal wave where the pressure and particle velocity at each spatial point are related by the acoustic impedance, which is dependent on the density and bulk modulus of the medium [23]. As the sound wave propagates through the tissue, it is scattered and reflected when the acoustic impedance varies along the wave propagation path. The acoustic signal at the face of the transducer is the summation of the interference pattern of the scattering and reflections.

The transducer then converts the acoustic energy into an electrical signal, which is modulated by the center frequency of the sound wave used to generate it. Modern ultrasound transducers are typically 1D or 2D arrays of small elements, each of which has a wire attached to it so that the received signal from each can be processed independently. One common method for processing these signals is delay and sum beamforming, where the signal from each element is time-delayed and then summed together, thus applying an electronic lens to the data to focus at a location within the tissue [23].

After beamforming the data, the modulation frequency is still present, but it does not contain useful information for B-mode imaging; thus, the signal is demodulated (i.e., by quadrature demodulation or the Hilbert transform), and the amplitude of the demodulated signal is obtained. The resulting data is referred to as an amplitude-line (A-line) and contains the magnitude of the reflected and scattered acoustic signal. A brightness mode (B-mode) image is comprised of multiple A-lines obtained across a field of view.

2.3 Acoustic Radiation Force

As the acoustic wave propagates through a medium, it also transfers momentum to the medium due to scatter and absorption, which results in the acoustic radiation force (ARF) [73]. Following Nyborg [73], the radiation force can be modeled by:

$$\mathbf{F} = \frac{2\alpha\mathbf{I}}{c_0} \tag{2.1}$$

where $\mathbf{F}$ is the radiation force $[kg/(s^2cm^2)]$, $\mathbf{I}$ is the temporal average acoustic intensity $[W/cm^2]$, α is the acoustic attenuation $[Np/m]$, and c_0 is the speed of sound $[m/s]$.

ARF is generated whenever sound propagates through a medium, however, to harness this force for use in ultrasound elasticity imaging, high energy, relatively long duration $(10 - 2000\mu s)$ focused ultrasonic waves are transmitted into the tissue where they generate displacements on the order of microns in the direction of wave propagation [33]. Due to the focusing of the waves, there is a force gradient through depth, laterally, and in elevation as dictated by the energy distribution. Typically, the region of excitation (ROE) is the region over which the ultrasonic wave is tightly focused and can be approximated as $\frac{\lambda z}{D}$ in the lateral and elevation dimensions and $8F^2\lambda$ axially, where λ is the ultrasonic wave length, z is the focal depth, D is the appropriate (lateral or elevation) aperture size, and F is the lateral F-number.

2.4 Ultrasonic Displacement Tracking

ARF-based imaging involves monitoring the tissue response to the applied force. To determine the tissue response, it is necessary to track the displacement, which is accomplished with conventional, broadband ultrasonic pulses [89]. Typically, one or more broadband pulses are transmitted into the tissue and the backscatter echoes are recorded after beamforming; these data are used as a reference. The long duration pushing pulse is then transmitted; although it is long duration compared to a broadband pulse, it can be considered nearly impulsive with respect to the tissue response. Finally, the same type of broadband pulse that was used for the reference is again transmitted, and backscatter echoes are received, which are known as the tracks.

The tracks are then compared to the reference in order to determine the displacement of the tissue. If radio-frequency data were collected, normalized cross-correlation is typically used to estimate the displacement of the tissue [111]. For scanners with parallel receive capabilities, in-phase and quadrature (IQ) data are commonly collected to reduce the required number of samples per beam. To estimate the displacement using IQ data, a phase shift estimation algorithm is typically be used, such as Kasai's [54], Loupas's [58], or Pesavento's [88] algorithms.

2.5 Acoustic Radiation Force Impulse (ARFI) Imaging

ARFI imaging consists of monitoring the response of the tissue in the region where the radiation force is applied. In general stiffer tissues displace less than soft tissues, thus creating the contrast in ARFI images. To generate a 2D ARFI image, it is necessary to push and track at every spatial location across the field of view; thus, a single ARFI frame can take hundreds of milliseconds to acquire. Additionally, the tighter the focus of the push beam, the better contrast that is observed in the images, but this reduces the axial ROE and requires additional pushes across the same field of view, so the image quality and frame rate trade offs must be considered [71].

ARFI imaging measures the displacement (u), which is the integral of the strain (ϵ), of the tissue in response to an applied force (or stress, σ). The strain is related both to the applied stress (σ, i.e. force per unit area) and the inherent tissue mechanical properties (E, the elastic, or Young's modulus), and under simplifying assumptions is described by the equation:

$$\epsilon = \frac{\sigma}{E}. \tag{2.2}$$

Thus, ARFI imaging portrays the displacement response of the tissue to the radiation force, such that tissues with higher stiffness have smaller displacements. However, due to the focused acoustic wave, there is a depth dependent gradient of radiation force applied to the tissue; thus, depth dependent normalization is typically applied to the data to generate uniform images in homogeneous media. Additionally, the noise on the displacement estimates, known as jitter, can be reduced in a variety of ways including low pass filtering through time and median filtering 2D images.

2.6 Shear Wave Elasticity Imaging (SWEI)

Although SWEI utilizes similar ARF excitations, it consists of monitoring the response of the tissue in a region laterally offset from the radiation force excitation [98]. For scanners with high parallel receive capabilities, it is possible to acquire SWEI data very quickly with as little as a single reference, push, track ensemble ($<$ 10ms). The data are then split into lateral and axial kernels over which the tissue is assumed to be homogeneous and isotropic. The wave arrival time at each location can be determined by a variety of methods such as time to peak [82], time to peak slope [95], or cross-correlation [62]. Under the homogeneous and isotropic assumptions, the wave arrival time should vary linearly with position, so a linear regression is typically performed to estimate the shear wave speed in the material [82], although more advanced methods such as random sample consensus [112] or radon sum transform [94] have also been investigated.

The spatial and temporal behavior of a shear wave in tissue is governed by the wave equation:

$$\nabla^2\mathbf{u} = \frac{1}{c_s^2}\frac{\delta^2\mathbf{u}}{\delta t^2} \tag{2.3}$$

where $\mathbf{u}$ is the displacement of the tissue, c_s is the wave speed, and ∇ is the Laplacian operator. The constant of proportionality that scales between the spatial (left side of the equation) and the temporal (right side of the equation) behaviors of the wave is c_s, which is known as the shear wave speed. The shear wave speed can be related to the inherent material properties through assumptions of linear elasticity, incompressibility and homogeneity. Specifically,

$$c_s = \sqrt{\frac{\mu}{\rho}} = \sqrt{\frac{E}{3\rho}}, \tag{2.4}$$

where μ is the shear modulus, ρ is the density and E is the Young's modulus. Therefore, if the shear wave speed is measured using SWEI, it is possible to directly estimate the corresponding shear and Young's moduli.

3

Development of Radiation Force Imaging Prototyping Tools on the Siemens Acuson SC2000™

3.1 Introduction

Acoustic radiation force (ARF) based imaging has been studied extensively using the Siemens Elegra™, Antares™, and S2000™ ultrasound platforms as part of a research agreement between Duke University (Drs. Nightingale and Trahey) and Siemens Healthcare (Siemens Medical Solutions USA, Inc., Ultrasound Division, Mountain View, CA, USA). With the introduction of the Siemens Acuson SC2000™, multiple technological improvements over previous scanners were recognized, including: an improved power supply, arbitrary waveform generator, and additional parallel receive beamforming [103]. These capabilities can all be utilized to improve ARF-based imaging and reduce acoustic exposure and acquisition duration, but current prototyping tools available were limited to the previous generations of scanners. Therefore, the development of a new tool set that would allow for rapid prototyping of radiation force imaging sequences was required.

The prototyping tools used on the older scanners involved 3 main components:

saving parameter tables, manipulating or merging the tables, and loading the new tables and acquiring data. The parameter tables consisted of data such as: transmit and receive apodization and delay data, transmit pulse data, and system timing information. Specifically for ARF-based imaging, multiple sets of tables were saved from the scanner detailing both the push and track configurations; these tables were then merged together to create a radiation force imaging sequence. Once the sequence and parameter tables were defined, they would be loaded into the scanner software, which would fire the sequence and save the raw radio frequency (RF) or in-phase and quadrature (IQ) data.

The base tool set contained code to read and write the parameter tables, as well as save them from and load them onto the scanner. Examples for how to merge the tables together for some imaging sequences were provided, but the merging code was typically sequence specific, so in many cases, it had to be manually modified. Although versatile due to its flexibility to manipulate the tables, the modifications could take a significant amount of time to code. Additionally, because the code manipulated text files, merging the data sets was a slow process as all of the data was read and written as ASCII files.

The code to load the tables back onto the scanner and save data was standardized; however, processing code to estimate the displacements from the raw RF or IQ data was not contained within the tool set provided. This lack of standardized processing code resulted in many unvalidated, custom displacement estimation programs, as well as the use of suboptimal displacement estimation algorithms [89].

In addition to the limitations of the tool set, the ability to manipulate the software on the scanner was also constrained. Specifically, the transmit beam positions and parallel receive locations were required to exist in a current imaging case on the scanner, and there was limited ability to modify these imaging cases. Additionally, manipulating the scanner by loading the custom parameter tables would often lead to non-deterministically crashing the scanner software or hardware.

Based on the previous tool sets as well as the scanner limitations, a new radiation force imaging tool set was designed for the Siemens Acuson SC2000™ to enable the scanner to collect similar data as previous scanners, but also to address some of the challenges detailed.

3.2 Background

To sequence a scanner for radiation force imaging, there are two main requirements: the ability to manipulate the front-end parameters for each transmit event and the ability to save the raw, beamformed (RF or IQ) data. In deciding how to prototype radiation force imaging on the Siemens Acuson SC2000™, multiple sequencing schemes were considered.

The SC2000™ was designed to perform volumetric imaging, but radiation force imaging is primarily performed using 1D arrays. Therefore, one consideration was to add a false elevation dimension, which could manipulate the low level hardware parameters necessary to sequence the scanner. This method was discarded for two primary reasons: it would prevent the users from ever using the tool set for a volumetric imaging case, and the large size of the parameter tables would have taken too much time to load into the scanner memory.

A second method that was considered was using B-mode to perform the displacement tracking and utilize a separate mode, such as M-mode, for the pushing pulses. By completely separating the push and track configurations into separate modes on the scanner, significant flexibility could be achieved. However, for radiation force imaging, the timing between the push and track pulses needs to be precise, and the time to switch between the modes was not perfectly deterministic; therefore, this method was also discarded.

Finally, the method chosen for prototyping radiation force sequences was collinear events, which is the same method that is used for sequencing color flow Doppler on the SC2000™. In this method, the number of collinear events corresponds to the number of times each beam group is fired repeatedly before moving to the next beam group. This method results in a set of spatially aligned parallel receive beams (track lines), while giving access to manipulate the front-end parameters for each collinear event and beam group as required.

As with most ultrasound scanners, the SC2000™ was designed to process and push multiple data types through the software, however access to the raw, beamformed data was limited. Initially, to save the IQ data, it had to be dumped directly from a hardware buffer as an ASCII text file, which was a very large, inefficient file and the saving required a long time during which the scanner could not be imaging (anywhere from 10 seconds upwards of several minutes depending on the data size).

To facilitate rapid data acquisition, a data pipeline was created to move the IQ data from the hardware buffers to the main memory in the MBM. This pipeline allows the user to save binary data files, making it possible to acquire and save the raw data in real time. Additionally, when using the pipeline, real-time B-mode imaging is still available as the IQ data in memory are processed with envelope detection and log-compression, then pushed to the back end for display (see figure 2.1).

3.3 Radiation Force Tool Set Development

After deciding how to program prototype radiation force imaging sequences and creating the IQ data pipeline to rapidly save the raw data, the development of the tool set commenced. The initial phase of code development was to determine how to generate the necessary parameter tables for both the push and track configurations. To accomplish this task efficiently, the imaging parameter and optimization database (IPOD) generation code was utilized, which restricted the push and track configurations to the flexibility that existed within the IPOD code base, including but not limited to: manipulating the numbers of beam groups and parallel receive lines, choosing the center and sampling frequencies, and optimizing the gain, filter and demodulation parameters. Although this choice does not provide arbitrary control over the scanner, which could limit the overall flexibility of the tool set in the future, the IPOD generation code does allow for more sequence customization than was available on previous scanners.

To utilize the IPOD code base for radiation force imaging, it is run twice to create both the track and push parameter tables. Custom code was then written to merge the tables together along with the controls for when each set of parameters should be used. Initially, four tables were manipulated: transmit delays, transmit apodization, system timing, and transmit pulse. These tables allowed for the push and track configurations to have different focal depths and aperture sizes, as well as provided the correct control for the low-level clocks based on the system timing. The transmit pulse required manipulation to fire a long duration pushing pulse in between the broadband tracking pulses.

Basic radiation force sequences could then be implemented and tested. Examples were provided for a standard 2D ARFI image configuration and for a SWEI configuration where the location of the push beam was fixed while moving the tracking beam locations. Because of its reliance on the IPOD code base, the tool box was very fast (i.e., within less than 30 seconds, a user could define new parameters and create new tables); however, the loading of the parameter tables and setting of secondary parameters such as the transmit voltage were still done manually. Thus, a new version of the tool box was created including automatic generation of batch scripts as well as additional tables for the secondary parameters. These batch scripts allowed the user to automatically load the tables, fire the sequence, and save the data, significantly reducing the total acquisition time. Additionally, the ability to ECG trigger radiation force sequences was enabled, and low-level control of the pulse repetition interval (PRI) between the tracking and pushing pulses was expanded.

Although the previous version significantly reduced the acquisition time, it still required manually switching between live B-mode imaging and the radiation force imaging case. To improve the work flow, the tool set was expanded to generate new batch files, which automatically perform this task. Python code was also integrated into the tools to allow for runtime manipulation of scanner parameters. For example, to notify the scanner software that the radiation force parameter tables had finished loading, the Python code could deliver low-level commands to the hardware in real time. The Python code was also used to determine when the data had finished saving, and then create a timestamped parameters file associated with the data file containing information necessary for processing.

Since the prototyping tool box now included standardized data and parameters file formats, MATLAB processing code was created to read these files, perform displacement estimation and generate a results file including the displacement data, time vector, and lateral and axial coordinates. The displacement estimation code was validated using a Newport MM3000 motion controller (Newport Corporation, Irvine, CA) to move a transducer in small, fixed increments and record data at each position. The estimated displacement could then be compared back to the known motion of the transducer (see section 3.4).

The tool box now allowed for rapid prototype sequence creation, data acquisition and processing, however the versatility and stability needed to be improved. The ability to modify the receive delays and apertures was added to the parameter table merging code, allowing for full control of receive vectors, enabling modes such as wiper-bladed ARFI imaging (method to increase the frame rate of ARFI imaging), M-mode ARFI imaging [17], as well as combined ARFI/SWEI sequences. To improve the stability of the prototyping tool, the method of loading the parameters was modified to allow for batch loading of the tables instead of serial loading, which significantly reduced the chance that a parameter would get loaded incorrectly due to it appearing at the wrong part of a clock cycle.

As the tool box expanded with the introduction of new imaging modes such as harmonic ARFI imaging [31] and multi-focal zone ARFI imaging [101], the inputs files and driver scripts began to become cumbersome. Therefore, a code refactoring was performed, which simplified the inputs to the tool box significantly and increased the flexibility of the batch files used to control the scanner. Multiple new runtime Python functions were created to provide additional sequence timing control, disable advanced imaging methods such as spatial compounding, and restore live B-mode imaging. As part of the code refactoring, new functions were also added into the tool box to perform consistency checks between all of the parameters specified.

The prototyping tool box was then put under version control to allow for collaborative work between all of the users, which has resulted in discovery and correction of multiple bugs within the tool set. Additionally, a variety of examples were created to demonstrate the different modes available in the tool box. Finally, additional processing code has been added to improve image quality including: dynamically merging multi-focal zone acquisitions, applying depth-dependent gain to ARFI data, and band-pass filtering displacement data.

Currently, upwards of 61 parameters can be specified in the input files to the radiation force prototyping tools as well as all of the parameters specified when using the IPOD generators. Both fundamental and harmonic tracking are supported along with arbitrary control over the locations of the push and track beams for ARFI, SWEI, M-mode ARFI, and combined modes. When acquiring data, arbitrary timing (PRI) between each transmit event in the sequence can also be specified, and standard or ECG triggered acquisitions can be performed. If desired, high quality B-mode data can also be acquired after the radiation force imaging sequence.

3.4 Displacement Estimation Validation

As part of the development of the radiation force imaging prototyping tools, it was necessary to validate the displacement estimation MATLAB code. Therefore, a Newport MM3000 motion controller (Newport Corporation, Irvine, CA) was used to translate a linear array in 5μm increments from 0-50μm, collecting data at each location. Raw RF data and two sets of IQ data, both before and after hardware demodulation, were saved at each position with a 40 MHz sampling rate at center frequencies of 5 MHz, 7 MHz, and 9 MHz. The RF data were processed using normalized cross-correlation and compared to the pre-demodulation IQ data processed using a phase shift estimator [89, 58]. The pre- and post-demodulation IQ data were compared as well.

Figure 3.1 depicts the comparison between the normalized cross-correlation and phase shift algorithms. Data were collected for 200 lateral locations and averaged across the field of view to reduce noise. In figure 3.1, the two algorithms result in nearly identical displacement data, except for the 9 MHz, 50μm displacement, which corresponds to a shift greater than $\lambda/2$ computed as the two-way acoustic propagation wavelength. This large displacement results in noise in the phase-shift computation because the estimator is unable to distinguish $\pm 180^\circ$. Both the normalized cross-correlation and the phase-shift algorithms yield data that is within 5% of the true displacement as recorded from the translation stage. The primary source of error in these measurements is if the face of the transducer was not perpendicular to the axis of translation, the estimated displacement would be slightly different than the translation value.

Figure 3.2 depicts the displacement estimated using the phase shift algorithm before and after hardware demodulation. The post-demodulation data for the larger displacement values (i.e., $> \lambda/8$) have some curvature in the displacement versus

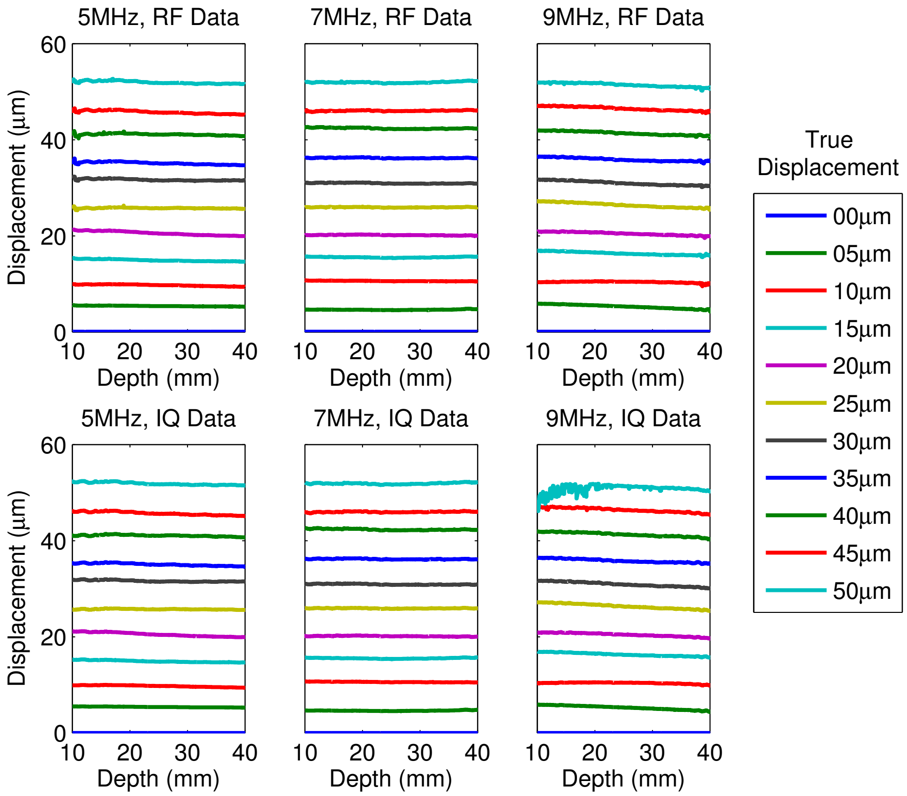

Figure 3.1: Displacement versus depth profiles for normalized cross-correlation (top row) and phase-shift (bottom row) displacement estimation algorithms are compared for three different center frequencies (5 MHz left column, 7 MHz center column, 9 MHz right column) and 10 different displacement magnitudes. The true displacement corresponds to the distance that was moved using a Newport MM3000 motion controller, which has a precision of 0.1μm. Both algorithms yield nearly identical displacement data that is within 5% of the true displacement, except for the 9 MHz, 50μm displacement, which corresponds to a shift greater than $\lambda/2$.

depth profiles, which is a result of the quantized hardware demodulation and baseband filtering. The quantization is due to the number of bits available in hardware to perform these operations since integer and fixed point math, not floating point math, must be used. The mean displacement over depth, however, is still within 5% of the true displacement.

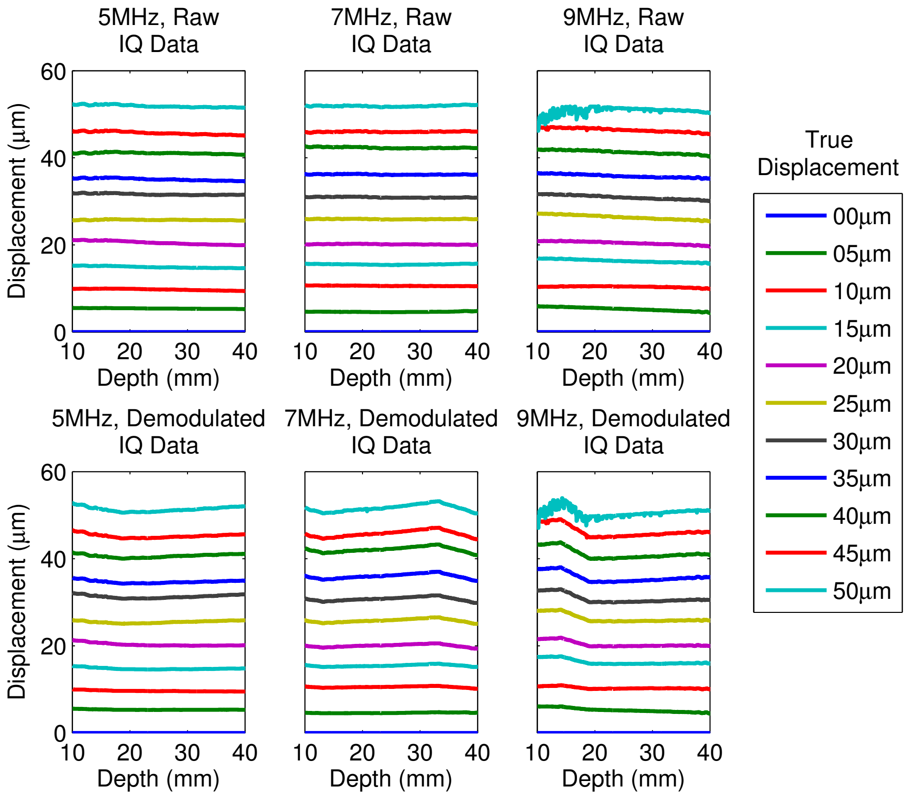

FIGURE 3.2: Displacements estimated using a phase shift algorithm before and after hardware demodulation, demonstrating the effect of integer and fixed point math on demodulation. The curvature in the displacement versus depth profiles is apparent when the displacement exceeds $\lambda/8$.

3.5 Master Clock and Power Supply Noise

In addition to displacement estimation validation, the ability to reliably acquire high quality data with a wide range of radiation force imaging parameters was investigated. In this work, one of the main challenges was correctly setting the power supply settings on the scanner, which manifested itself as two separate confounding effects: a global displacement artifact early in time, and a variable displacement amplitude as a function of tracking frequency.

Figure 3.3 depicts displacement versus time plots at three different depths (15 mm, 22.5 mm, and 30 mm) acquired with three different power supply settings; the

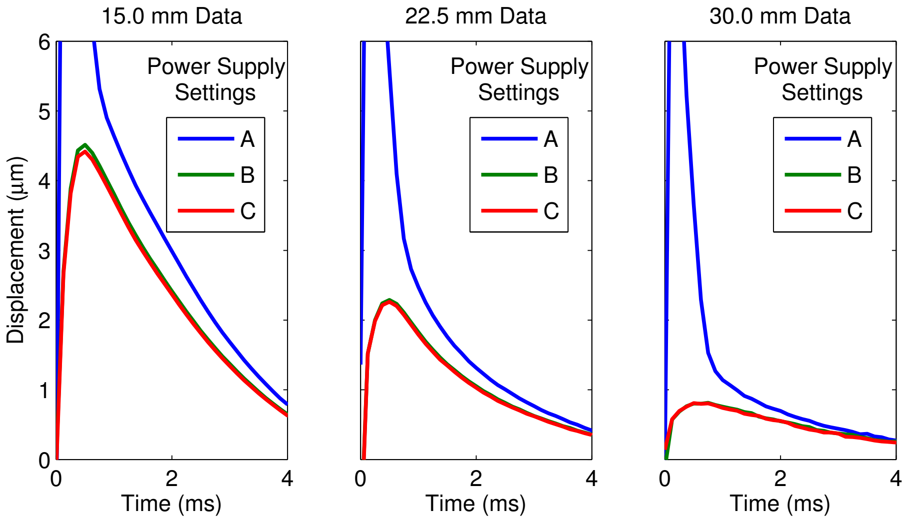

FIGURE 3.3: Displacement versus time profiles at three depths (15 mm, left, 22.5 mm, center, and 30 mm, right) for three different power supply configurations. The pushing and tracking configurations were not changed between the different power supply settings, thus they should all have the same displacement magnitude, however, power supply settings A clearly shows an artifact in the displacement estimation. It is hypothesized that when the power supply is set incorrectly, the master clock is perturbed by the pushing pulse, which results in a displacement artifact; thus, either configuration B or C should be used, but not configuration A.

displacements after force cessation were averaged across the lateral field of view in a homogeneous phantom. For all three power supply configurations the displacement magnitude should be identical, however after transmitting the pushing pulse, the displacement profile for setting A is very different than the profiles for settings B and C. In this case, it is hypothesized that the pushing pulse in configuration A perturbs the master clock which causes every lateral location acquired to appear to have high displacement early in time. Since the master clock controls the start of receive time, any deviation in the clock between the pre-push reference lines and the post-push track lines appears as a displacement artifact after the push, as is seen in figure 3.3. Based on this work, a fix was added to the radiation force tool box that prevents the use of power supply setting A.

An additional issue with the power supply was also discovered when varying the

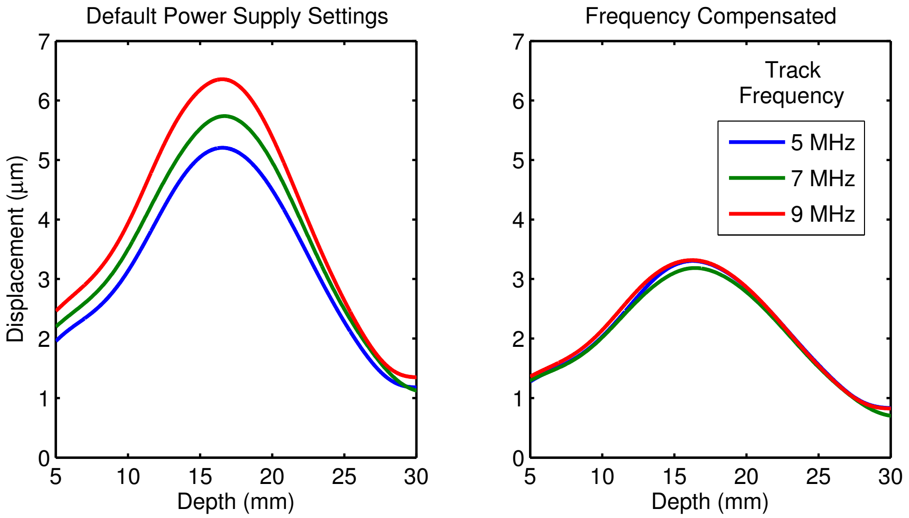

FIGURE 3.4: Displacement versus depth profiles for the default power supply settings (left) and frequency compensated power supply settings (right) demonstrating the need to compensate for the track frequency in the power supply to achieve a consistent push magnitude.

center frequency of the tracking beams, but maintaining the same pushing configuration. The displacement in a uniform phantom was not consistent between the different configurations, as seen in the left plot of figure 3.4; however, based on figures 3.1 and 3.2, the issue was not in the displacement estimation code. After investigating the parameters being loaded onto the scanner, it was determined that the push amplitude was actually varying as a function of track frequency because one of the power supply parameters was not being compensated for correctly, and separate from the issue seen in figure 3.3. After compensating for the center frequency of the tracking beams, the same data were re-acquired and are shown in the right plot of figure 3.4, which shows no variability between the different track frequencies.

3.6 Transducer Implementation and Optimization (ER7B)

Throughout the development of the prototype radiation force imaging tool box, multiple unsupported transducers were introduced on the SC2000™ for specific appli-

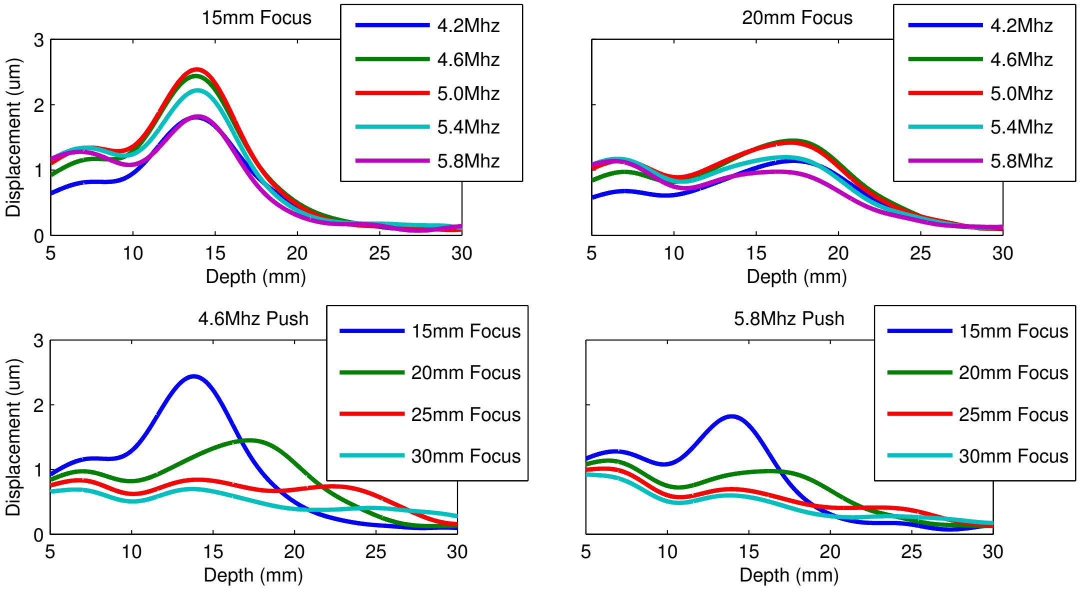

FIGURE 3.5: Displacement magnitude in a homogeneous phantom as a function of push focus and frequency 0.2 ms after force cessation. The top row of plots depicts data for a fixed focal depth whereas the bottom row of plots depicts the data for a fixed push frequency. Based on this data, 4.6 MHz was chosen as the push frequency for subsequent experiments.

cations, such as the ER7B, which is a transrectal ultrasound transducer that was originally used on the Acuson XP128 and Aspen ultrasound scanners. To enable B-mode imaging, probe files of another linear array were modified to match the specifications of the ER7B. Parameters such as the impulse response, number of elements, element size, and lens focus were input into the scanner to correctly perform transmit and receive beamforming. Optimization of B-mode image quality was also performed, involving setting depth dependent demodulation, baseband filter, and front-end gain parameters as well as using coherent imaging technology, known as INFocus [16].

The ER7B was then optimized for ARFI imaging by performing a set of experiments while varying the push frequency and focal depth. The resulting data, depicted in figure 3.5, motivated the use of 4.6 MHz as the push frequency. Example depth-normalized ARFI images focused at 15 mm and 25 mm are shown in figure 3.6

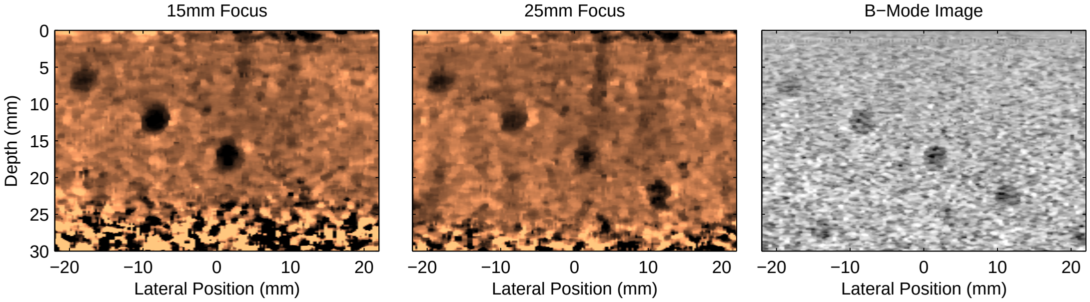

FIGURE 3.6: Example depth-normalized ARFI images and corresponding B-mode image of a custom CIRS tissue-mimicking phantom with stiff 3 mm diameter lesions acquired with the ER7B transducer. The 15 mm focus ARFI image has better contrast and resolution for the middle 2 lesions, however the deep lesion is only visible in the 25 mm focus ARFI image.

along with the corresponding B-mode image using a custom CIRS tissue-mimicking phantom (CIRS, Norfolk, VA) with 3 mm diameter lesions, which are stiffer than the background material.

Additional investigation and validation of the ER7B pushing configuration was performed both to investigate the performance of the transducer and to validate the radiation force imaging tool box. Figure 3.7 depicts the 2D displacement profile 0.3 ms after force cessation for three different push focal configurations, F/1, F/2, and F/3 all focused at 15 mm; the displacements have been depth-normalized by the on-axis displacement (lateral position 0 mm). Comparing the beam profile from 5-10 mm, the differences in the shape of the push beam between the different focal configurations are apparent, confirming that the F/# was correctly varying between the acquisitions.

Analyzing the F/1 configuration in figure 3.7, there appears to be displacement at 6 mm laterally, which is lower-amplitude, but still significant; thus, an investigation into this off-axis displacement was performed by using a F/1 configuration focused at 15 mm and 25 mm. Depicted in figure 3.8, using a larger lateral field of view and plotting the displacements in decibels, it is clear that this off-axis displacement

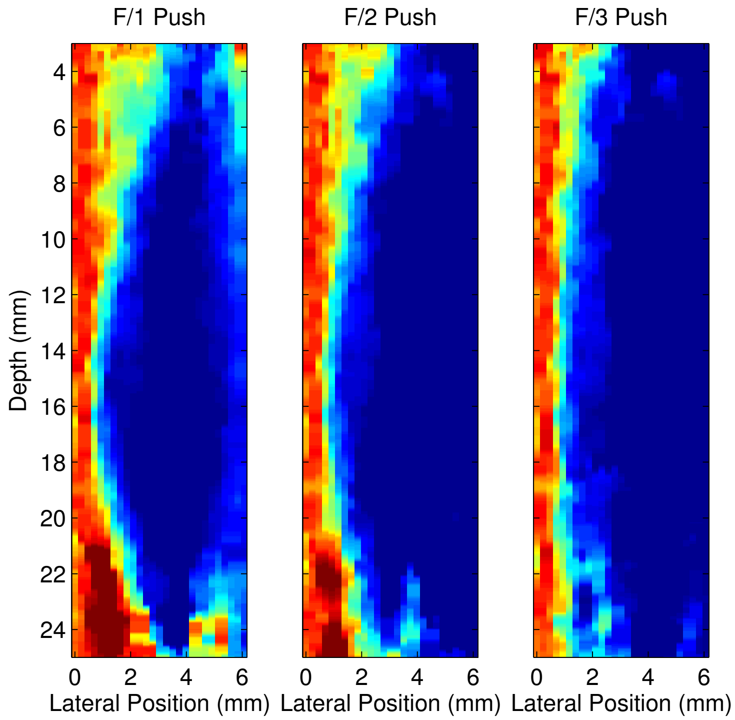

FIGURE 3.7: Displacement profiles of three push beam geometries (F/1 left, F/2 center, F/3 right) as a function of lateral and axial position, 0.8 ms after force cessation; the displacements were depth-normalized based on the on-axis magnitude. Based on the beam geometry changes as a function of focal configuration shown here, these data validated the manipulation of the aperture for the push beam.

is significant. It is hypothesized that the displacement is a result of the grating lobes of the transducer, which are off-axis locations where the acoustic energy sums constructively [23]. The lateral location of the grating lobes is computed as:

$$x = n\frac{\lambda z}{s},$$

where x is the lateral position of the grating lobe, n is the grating lobe number, λ is the wavelength, z is the focal depth, and s is the element pitch. In this case, the first grating lobes should appear at 5.8 mm and 9.7 mm laterally for the 15 mm and 25 mm foci, respectively, corresponding well with the displacement seen in figure 3.8.

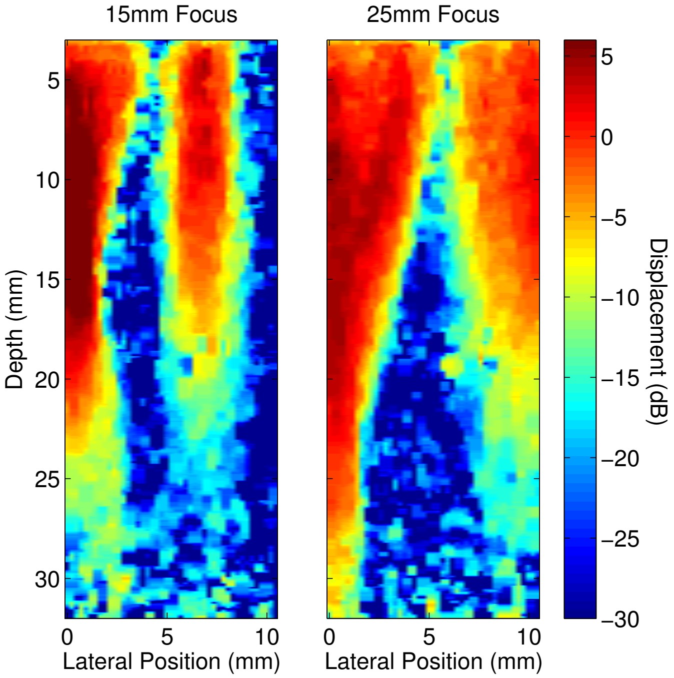

Figure 3.8: Displacement profiles of F/1 pushes focused at 15 mm (left) and 25 mm (right) are shown on a decibel scale. Secondary lateral foci appear at approximately 6 mm and 11 mm for the 15 mm and 25 mm focal depths, respectively, which correspond well to theoretical locations of grating lobes for this transducer.

3.7 Transducer Comparison

In addition to validating the radiation force imaging tool box and implementing and optimizing the ER7B transducer, a comparison was performed between the ER7B, a prototype 12L4 linear array, and the 9L4 linear array. The 9L4 transducer is a multi-D array, and therefore, experiments were performed using either the center row of elements or the full elevation aperture. The push frequency for all three transducers was fixed at 4.6 MHz with an F/2 focal configuration to standardize for any attenuation effects; however, this frequency was not necessarily optimal for each transducer.

Figure 3.9 depicts the resulting displacement versus depth profiles for the different transducers 0.3 ms after force cessation. Looking at the shallowest focus, 10

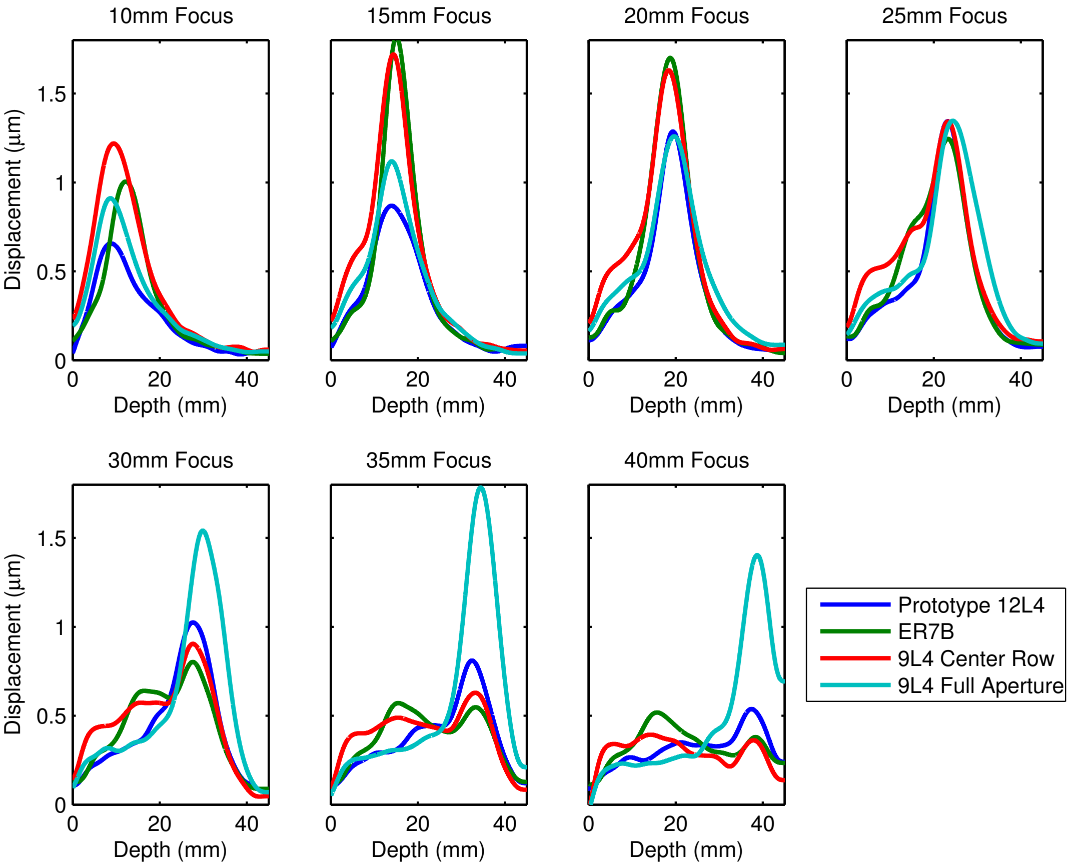

FIGURE 3.9: Displacement magnitude in a homogeneous phantom for the ER7B, prototype 12L4, and 9L4 linear arrays as a function of push focus 0.3 ms after force cessation. The center row of the 9L4 performs the best for the shallowest focus, but as the focal depth increases, the optimal transducer changes, with the full aperture of the 9L4 performing the best at the deepest depths.

mm, it is clear that the center row of the 9L4 performs the best. As compared to the full aperture of the 9L4, the center row has higher displacement due to a narrower elevation beamwidth, which results in the push needing to displace less tissue and reducing the displacement underestimation when tracking [84]. At the shallow depths, the prototype 12L4 displacement magnitude is quite low compared to the other transducers and has a broader full-width half-max axial profile. The ER7B has good displacement amplitude, however, the energy is concentrated deeper than the desired focus.

As the focal depth increases, the center row of the 9L4 and ER7B both perform well, but by 25 mm, they both demonstrate significant near field loss that the prototype 12L4 and 9L4 full aperture do not. At the deepest depths, the prototype 12L4 outperforms the ER7B and center row of the 9L4 with regards to displacement magnitude and near field loss, however, the full aperture of the 9L4 is clearly the best deeper than 30 mm.

3.8 Conclusions

In this chapter, a tool box for prototyping radiation force imaging on the SC2000™ was described that was designed, implemented and validated along with processing code to estimate the displacements. Multiple issues with both stability and speed were addressed including: rapidly saving binary data files, incorrectly loading parameter tables, validating the displacement estimation, and addressing power supply and master clock noise. The tool box currently supports setting upwards of 61 parameters specific to the radiation force sequence along with many more parameters used by the IPOD generation code that specify the imaging case. Examples of the flexibility and utility of the tool box were then demonstrated by implementing and optimizing a new transducer (ER7B) and comparing it to the 9L4 and prototype 12L4 linear arrays.

4

GPU-Based Real-Time Small Displacement Estimation with Ultrasound

This chapter has been published in the journal IEEE Transactions on Ultrasonics, Ferroelectrics and Frequency Control, 58(2), pages 399-405.

The following chapter describes the use of general purpose computing on graphics processing units to estimate displacements from raw IQ data and generate ARFI images in real-time. The development of real-time processing approaches is important for ultrasonic research systems to be able to assess image quality and make modifications during studies and is complimentary to the development of the prototyping tool set described in the previous chapter.

4.1 Abstract

General purpose computing on graphics processing units has been previously shown to speed up computationally intensive data processing and image reconstruction algorithms for CT, MR, and ultrasound images. Although some algorithms in ultrasound have been converted to GPU processing, many investigative ultrasound research systems still use serial processing on a single CPU. One such ultrasound modality is acoustic radiation force impulse (ARFI) imaging, which investigates the mechanical properties of soft tissue. Traditionally, the raw data are processed offline to estimate the displacement of the tissue after the application of radiation force. It is highly advantageous to process the data in real-time to assess the quality and make modifications during a study. In this paper, we present algorithms for efficient GPU parallel processing of two widely used tools in ultrasound: cubic spline interpolation and Loupas' two-dimensional autocorrelator for displacement estimation. It is shown that a commercially available graphics card can be used for these computations, achieving speed increases up to 40× as compared to single CPU processing. Thus, we conclude that the GPU based data processing approach facilitates real-time (i.e. < 1 second) display of ARFI data and is a promising approach for ultrasonic research systems.

4.2 Introduction

There has recently been much investigation into using graphics processing units (GPUs) instead of CPUs for scientific computing. To facilitate using graphics cards for scientific computing, NVIDIA introduced compute unified device architecture (CUDA) to allow users direct access to program the GPUs on NVIDIA graphics cards [2]. The graphics cards' architecture contains a large number of processing cores (64-512) each with a small amount of local memory (2 kB), all of which can be used in parallel. To utilize the full power of the GPUs, it is necessary to redesign algorithms to work in a parallel environment rather than a conventional serial environment. It has been shown that GPUs can significantly increase the speed of CT image reconstruction [116, 102, 44, 50], MR image reconstruction [99, 43], multi-modality image registration [123], ultrasound scan conversion [125], and ultrasound Doppler flow processing [22].

Ultrasound researchers could clearly benefit from GPU-based processing of raw data to achieve real-time displays for their investigation methods. One such example is acoustic radiation force impulse (ARFI) imaging, which utilizes ultrasound to visualize the mechanical properties of tissue [72, 71]. High intensity focused acoustic beams are used to generate acoustic radiation force within the tissue, causing small displacements (on the order of $10\mu m$). These displacements are monitored using ultrasonic correlation-based and phase-shift methods (i.e. normalized cross-correlation, Kasai's 1-D and Loupas' 2-D autocorrelators) [72, 58, 89, 54]. ARFI images are generated by laterally translating the ultrasonic beams and estimating the displacements through time at each location [72]. This scheme generally includes between 50-120 A-line acquisitions at 10-60 lateral locations, generating large amounts of data (1-50 MB). Data processing, including cubic spline interpolation, displacement estimation, and motion filtering, has traditionally been performed on a single CPU, taking multiple seconds to over one minute to process the data depending on the size [89]. Real time estimation and display of ARFI images would be advantageous in the development of new algorithms and sequences as well as for clinical feasibility studies. In this paper, GPU parallel processing is developed and implemented for ARFI imaging.

4.3 Background

4.3.1 NVIDIA Quadro FX 3700M and CUDA

The NVIDIA (Santa Clara, CA) Quadro FX 3700M is a high-end laptop graphics card that was utilized herein as part of a mobile workstation. The card's architecture consists of 16 multi-processors (MPs), each containing 8 stream processors for a total of 128 stream processors operating at 1.40 GHz. The Quadro FX 3700M has a total of 1 GB memory divided into 16 kB shared memory (SM) per MP and 64 kB constant memory, with the rest being global memory; each MP also has access to

8,192 registers.

One manner in which CUDA can be used is as an extension of the C and C++ languages, primarily allowing for memory copies between the CPU and GPU memory banks and the ability to launch programs, known as kernels, on MPs. Each kernel consists of a grid of blocks, where a block is a group of threads. Each block is launched on a single MP, such that all the threads in a block run in parallel. The block size is limited to 512 threads and the grid size is limited to 2^{32} blocks. When a block of threads is sent to a MP, a SIMT (single-instruction, multiple-thread) unit divides the block into groups of 32 threads called warps and the compiler, SIMT unit, and internal thread scheduler control when each thread is sent to a stream processor.

4.3.2 Acoustic Radiation Force Impulse (ARFI) Imaging

Acoustic radiation force arises from a transfer of momentum from an ultrasonic wave to the medium through which it is traveling [107]. This momentum transfer is due to both absorption and scattering of the wave, and is directly related to the acoustic attenuation [107, 70]. ARFI imaging utilizes this acoustic radiation force by applying short duration ($<$ 1ms) focused ultrasound pushing pulses that displace tissue [70]. Typical ARFI images are generated by acquiring at least one conventional reference A-line at the region of interest, then applying the pushing pulse, and finally acquiring additional tracking A-lines. The data can be acquired either in radio-frequency (RF) format or as quadrature demodulated (IQ) data. The response of the tissue is determined by estimating the displacement of the tissue between the pre-push reference and the post-push tracks [70]. The displacement estimation process for IQ data involves two standard ultrasonic image processing steps: cubic spline interpolation and Loupas' 2-D autocorrelator[58, 89]. In this paper we present GPU-based algorithms that we have developed to perform the sequence of operations shown in figure 4.1.

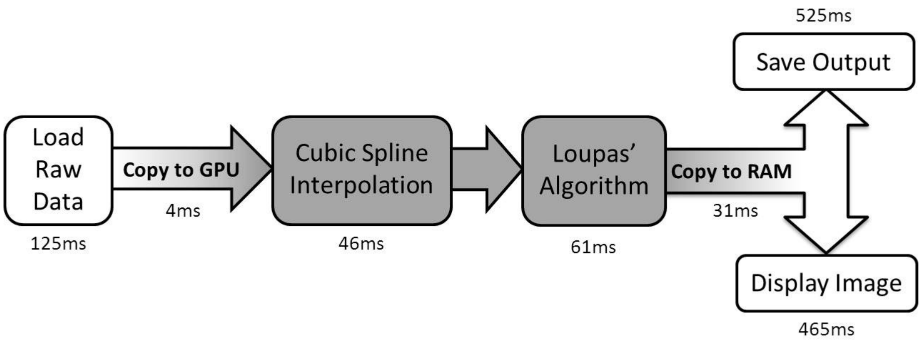

FIGURE 4.1: A flow diagram of the overall algorithm is shown along with the computation time for each step when using the CUDA code. The CPU stages of the program are shown in white and the GPU processing steps are shaded. The time required to load the data, copy it to the graphics card, process it, and copy it back to RAM is less than that to either save the output or display an image of the data.

4.4 Methods

4.4.1 Cubic Spline Interpolation

Cubic spline interpolation is used extensively in ultrasonic tracking methods to upsample the data in order to improve the precision of the velocity or displacement estimates [89]. Spline interpolation represents an extension of linear interpolation such that the first and second order derivatives are continuous. For a given function $y_i = y(x_i)$, $i = 1 \ldots N$, the interpolating spline for $x \in [x_i, x_{i+1}]$ is given by:

$$S(x) = y_i + b_i(x - x_i) + c_i(x - x_i)^2 + d_i(x - x_i)^3 \tag{4.1}$$

where b_i, c_i, and d_i are coefficients that are computed by solving a tridiagonal matrix [90]. Once the coefficients are computed, the abscissae at which the data are to be interpolated are substituted into equation 4.1.

The traditional solution to a tridiagonal matrix, such as that used to solve for the spline coefficients, involves a decomposition loop and a backsubstitution loop, both of which iterate over every (x_i, y_i) [90]. This algorithm is not well suited to parallelization since the solution is dependent on all of the data points. To solve for the coefficients using a parallel GPU architecture, a modified implementation was developed by dividing the long vector of data into small overlapping subsets.

The problem was divided into N/n spline interpolations, where n is the number of coefficients calculated in each interval and N is the total number of points to be interpolated. The spline coefficient kernel was then launched with each thread solving the tridiagonal matrix associated with $n+2k+1$ data points, where k is the number of overlapping points. The data were first copied into shared memory such that thread 0 copied $(y_0, \ldots, y_{n+2k})$, thread 1 copied $(y_n, \ldots, y_{2n+2k})$, and so forth. Each thread then computed the $n+2k+1$ coefficients associated with the data that it copied over using the traditional tridiagonal matrix solution. The coefficients were copied back into global memory so that the first k and last $k+1$ coefficients were thrown out. Thus, thread 0 copied $(b_0, \ldots, b_{n+k-1})$, thread 1 copied $(b_{n+k}, \ldots, b_{2n+k-1})$, thread 2 copied $(b_{2n+k}, \ldots, b_{3n+k-1})$, and so forth, into global memory.

The splines were then evaluated by launching a new kernel and having each thread of each block copy a y_i, b_i, c_i, and d_i into shared memory to compute $S(x)$ for $x \in [x_i, x_{i+1}]$. The output was then directly written to global memory. The speed and accuracy of the GPU-based spline interpolation was compared to the traditional implementation while varying the number of points per thread, the number of overlapping points, and the number of points to be interpolated.

4.4.2 Loupas' Phase Shift Estimator

One algorithm that is often used in displacement estimation for ARFI images is presented by Loupas *et al* and utilizes IQ data [58, 89]. The algorithm is based on equation 4.2, where M is the axial averaging range, m is the axial sample being used, N is the ensemble length, n is the IQ line being used, c is the speed of sound, f_c is the demodulation frequency, f_s is the sampling frequency, and $\bar{u}$ is the average displacement in that axial range. For ARFI imaging, a single pre-push reference is typically compared to each of the tracks to estimate the displacement through time and depth. Thus, the ensemble length is always 2, and for a given lateral location, the reference IQ line is constant.

To implement equation 4.2 using CUDA, each upsampled IQ line (2465 points) was divided into 512 point sections, corresponding to the number of threads in a block. Each section overlapped M points, the axial averaging window size, with the previous section so that the displacement would be estimated for each point in the IQ line. The grid of blocks was then created with the number of blocks equaling the total number of sections including all lateral locations and tracks per location. The kernel begins by declaring six 512-point shared memory arrays (12 kB) such that 4 arrays correspond to the I and Q components of one section of a paired reference and track, with the other arrays being used to store the data from the summations in equation 4.2.

To parallelize the algorithm, each thread computes a single parameter inside the summations of equation 4.2. Once the parameters are saved in shared memory, each thread performs a summation so as to have the minimum number of divergent threads. The parameters are computed such that shared memory blocks are overwritten so that all of the parameters are computed within the 12 kB that was originally declared. After the four summation parameters are computed, the demodulation frequency vector is copied from GPU global memory and equation 4.2 is evaluated using the built-in *atan2f* function. The displacement value is written directly to GPU global memory.

4.4.3 Computational Speed Tests

All code was compiled on a Dell Precision M6400 laptop with 4 GB RAM that was running Microsoft Windows XP. The laptop had an Intel® Core™2 Extreme Q9300 operating at 2.53 GHz and an NVIDIA Quadro FX 3700M with 16 multi-processors

$$\bar{u} = \frac{c}{4\pi f_c} \frac{\arctan\left(\frac{\sum\limits_{m=0}^{M-1}\sum\limits_{n=0}^{N-2}[Q(m,n)I(m,n+1)-I(m,n)Q(m,n+1)]}{\sum\limits_{m=0}^{M-1}\sum\limits_{n=0}^{N-2}[I(m,n)I(m,n+1)+Q(m,n)Q(m,n+1)]}\right)}{1+\arctan\left(\frac{\sum\limits_{m=0}^{M-2}\sum\limits_{n=0}^{N-1}[Q(m,n)I(m+1,n)-I(m,n)Q(m+1,n)]}{\sum\limits_{m=0}^{M-2}\sum\limits_{n=0}^{N-1}[I(m,n)I(m+1,n)+Q(m,n)Q(m+1,n)]}\right)\Big/\left(2\pi\frac{f_c}{f_s}\right)} \tag{4.2}$$

and 1 GB total memory. The CUDA code (GPU/CPU) was compiled using the nvcc compiler for CUDA 2.3 and the traditional C++ code (CPU only) was compiled using the gcc compiler for speed comparisons.

The programs were tested on 10 independent data sets acquired from a modified Siemens SONOLINE™Antares scanner (Siemens Medical Solutions USA, Inc., Ultrasound Division, Mountain View, CA, USA) using a VF7-3 transducer operating at 5.33 MHz. The data sets have 52 total push locations, 80 track pulses per push, and 493 I and Q samples per track. Each data set was processed 20 times and the run times were averaged. The error bars in all of the figures show the standard deviation of the average computation time between the 10 data sets. The computation times and speed increases stated for cubic spline interpolation include copying the raw 16-bit integers from RAM to the GPU global memory and for Loupas' algorithm include copying the displacement estimates from the GPU global memory back into RAM.

The multi-processor occupancy for algorithms that were executed on the GPU was also computed. The occupancy is a ratio of the number of active warps on a MP to the maximum possible number of active warps, which is 24 for the NVIDIA Quadro FX 3700M. The occupancy is a measure of the efficiency of the code, with the most efficient code having an occupancy of 1 [2].

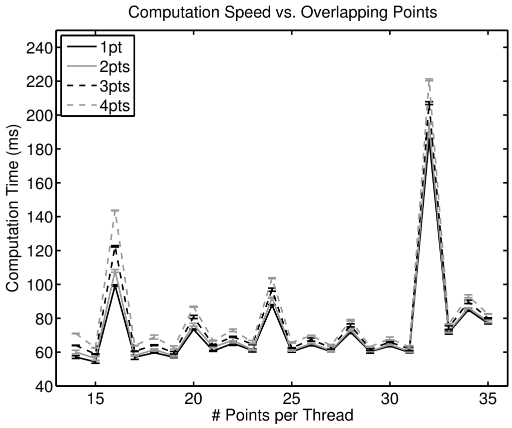

FIGURE 4.2: The computation time of cubic spline interpolation using CUDA as a function of number of points per thread and number of overlapping points. The computation time is linearly related to the number of overlapping points and is a complicated function of the number of points per thread that should be optimized empirically.

4.5 Results

Figure 4.2 compares the computation time with the number of overlapping points (k) and points per thread ($n + 2k + 1$) for interpolating 2×10^6 points from a sampling rate of 8.9 MHz to 44.4 MHz. The computation time is directly proportional to the number of overlapping points and has a more complicated dependence on the number of points per thread. The error associated with the parallelized approximation of the cubic splines as compared to the traditional algorithm was also computed. The maximum RMS errors were 0.33%, 0.15%, 0.12%, and 0.12% for 1, 2, 3, and 4 points of overlap, respectively.

A further analysis of the speed of the CUDA code was performed using 15 points per thread and 2 points of overlap. The CUDA code was compared to a traditional cubic spline interpolation algorithm [90] as programmed in C++. The number of points that were interpolated were varied logarithmically between 1×10^4 and 2×10^6 points. The resulting time to perform interpolation is shown in figure 4.3 and the speed increase of the CUDA code over the C++ code is shown in figure 4.3.

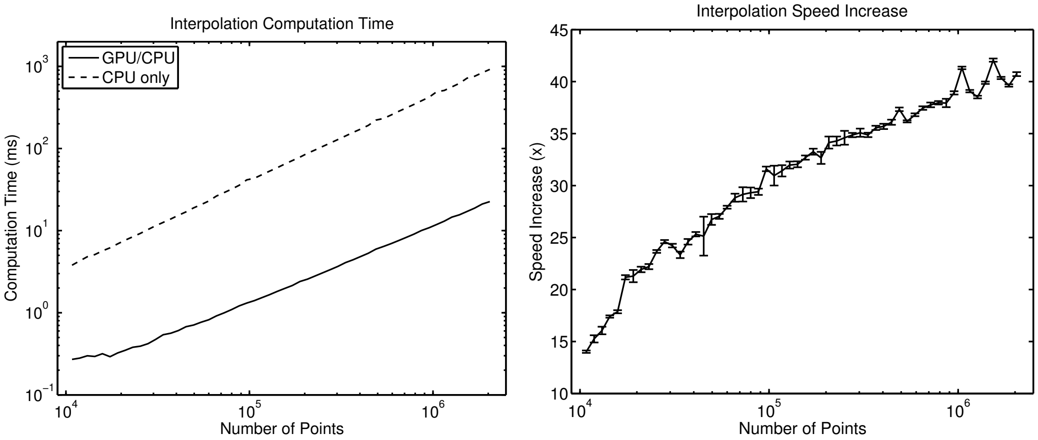

FIGURE 4.3: The computation time (a) and speed increase (b) of cubic spline interpolation as a function of the number of points to be interpolated. The efficiency of the CUDA code increases as the number of points to be interpolated increases, eventually plateauing at approximately 41× faster than the C++ code.

Using the algorithms outlined above, the computation time for the CUDA code was compared to previously optimized C++ code [89]. The speed increase for both the interpolation and Loupas' algorithm are shown in figures 4.4 and 4.4. In figure 4.4, the speed increase is shown as a function of the number of track pulses used assuming 52 push locations, and figure 4.4 assumes 80 track pulses while varying the number of push locations. The MP occupancy was 0.083, 0.667, and 0.667 for the spline coefficient, the spline evaluation, and the Loupas' algorithm kernels, respectively.

The speed increase of the CUDA code is constant for greater than 40 tracks (assuming 52 push locations) or greater than 20 push locations (assuming 80 tracks). In these cases, the CUDA implementations are 41× and 27× faster for cubic spline interpolation and Loupas' algorithm, respectively. The interpolation time includes copying the raw data to the graphics card, and the computation time for Loupas' algorithm includes copying the displacement estimates back to RAM. Additionally, the displacements estimated with the CUDA code had a maximum RMS error of $0.012 \mu m$ (1.1%) across the 10 data sets as compared to the C++ code.

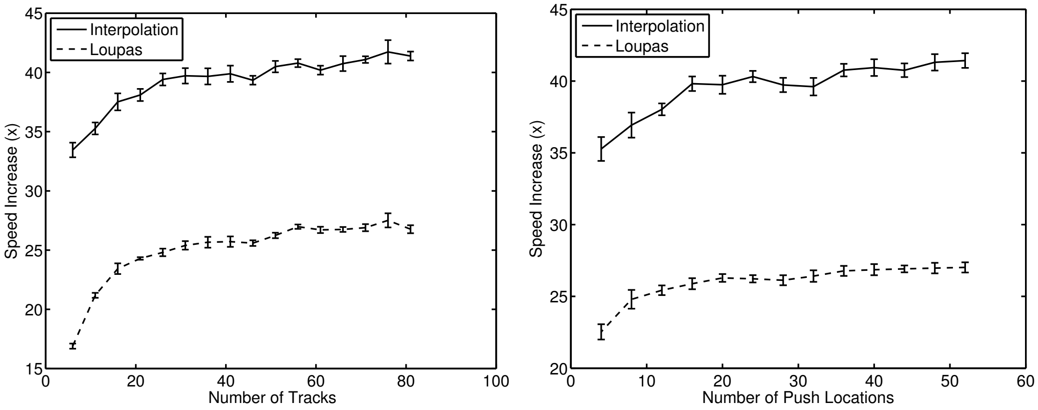

FIGURE 4.4: Speed increase for cubic spline interpolation and Loupas' algorithm as a function of a) the number of track pulses (assuming 52 push locations) and b) the number of push locations (assuming 80 track locations). As in figure 4.3, the speed increase of interpolation plateaus at approximately 41× faster for the CUDA code as compared to the C++ code. Similarly, Loupas' algorithm plateaus at 27× faster for the CUDA code. Additionally, 37% of the computation time associated with Loupas' algorithm is devoted to copying the displacement estimates from GPU memory to CPU memory.

Figure 4.5 shows the computation time associated with the components of processing an ARFI data set, including: acquiring the raw data, estimating the displacements, saving the displacement values to disk, and displaying an image. The data acquisition duration is based on transmitting 80 tracking pulses per location with a pulse repetition frequency of 7 kHz at 13 lateral locations using 4:1 parallel tracking for a total of 52 lateral locations. The data are saved using *fwrite* on single precision floating point numbers, and the graphical display is accomplished with OpenGL.

4.6 Discussion

The goal of this work is to develop a GPU-based real-time ARFI data processing system for use in clinical feasibility studies of ARFI imaging. The two principle computational steps required to achieve this goal are data interpolation and displacement estimation. To develop efficient GPU code for these algorithms, the two primary considerations were parallelizing the algorithms so that each data point is independent

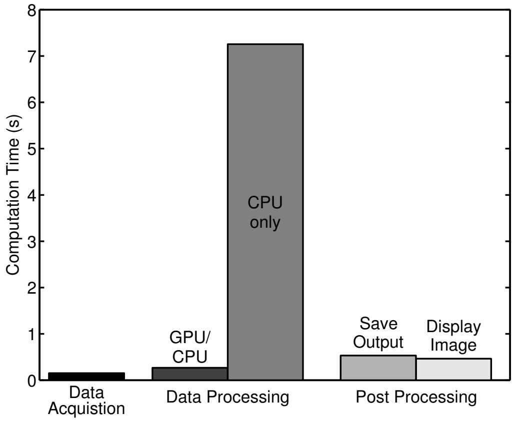

FIGURE 4.5: Time required for acquiring the raw data, estimating the displacements, saving the estimates to disk, and displaying an image using OpenGL. The time required for data processing is significantly reduced by using CUDA (i.e. GPU/CPU vs. CPU only), and therefore, it is no longer the rate limiting step in generating ARFI images.

and reducing the computational memory footprint of the data to at most 16 kB per 512 data points.

As shown in figure 4.2, the computation time for spline interpolation increases monotonically with the number of overlapping points, but has a complicated dependence on the number of points per thread. The monotonic behavior is expected due to the increasing number of computations required; however, the other trend is much more difficult to analyze. There is a small increase in the computation time as a function of the number of points per thread, but the dominant behavior seen is the erratic behavior from point to point. It is hypothesized that these rapid variations are due to the number of bits being copied between global and shared memory and the way the individual threads are accessing the data in shared memory. It is not feasible to account for all of these factors when initially developing the code, and therefore, optimization must be performed empirically by testing different numbers of points per thread.

Figure 4.3 shows the increasing efficiency of the CUDA code as the number of interpolation points is increased. This increase in efficiency is due to two major effects; firstly as the number of points increases, the CUDA code can occupy more of the MPs. The second effect is that as the number of points to be interpolated increases, a greater portion of the computation time is spent computing the required values compared to copying the data from RAM.

With respect to displacement estimation, both cubic spline interpolation and Loupas' algorithm reveal a distinct trend of increasing efficiency as the number of total computation points is increased, ultimately plateauing, as shown in figures 4.4 and 4.4. Although efficient, neither of these algorithms are perfectly optimized as seen by the MP occupancy for each algorithm, indicating that the MP is not being used to its maximum efficiency. In all cases, the occupancy is not equal to 1, but as seen in figure 4.5, the data processing step is no longer the rate limiting step, and thus additional optimization of the algorithms would not greatly improve the overall speed.

The speed increase of Loupas' algorithm is much smaller than that of interpolation primarily due to the memory copy operation back to RAM. This discrepancy results from the raw IQ data being 16-bit integers, which are then upsampled and stored as single precision floating point numbers (floats). After the displacements are estimated, they are also stored as floats at the high sampling frequency. Thus, the number of bytes copied to the graphics card memory is only 20% of the number copied back to RAM. The second copy operation accounts for 37% of the computation time of Loupas' algorithm. If this copy time was not included, the speed increase for Loupas' algorithm would be almost identical to that of the interpolation.

The small difference in the value of displacement estimates between the C++ code and CUDA code has two sources: the approximations made in the cubic spline interpolation and the use of single precision floating point numbers. Overall, the RMS error in the displacement estimates was very small $(0.012\mu m, 1.1\%)$ compared to the ARFI displacements induced ($1 - 5\mu m$). This error is also an order of magnitude less than the Cramer-Rao predicted lower bound for the accuracy of the measurements [111].

The total time to read in the raw data from disk, estimate the displacements using CUDA, and copy the data back to RAM is 267 ms compared to 7255 ms to perform the same operations using C++, an overall speed increase of 27×. The data processing using CUDA does take longer than the data acquisition time (152 ms), but the displacement estimation is no longer the rate limiting step when either saving the output or displaying an image using OpenGL, which requires over 450 ms to initialize the graphics and display an image. Although the time required to display an image is relatively large, this can likely be reduced by using CUDA 3.0, which was recently released [3]. This version of CUDA allows for the use of OpenGL while data is still on the graphics card rather than necessitating a copy to RAM and then back to the graphics card.

4.7 Conclusions

We have shown that two algorithms widely used in ultrasonic data processing, and specifically in ARFI imaging, are suitable for parallel execution on a GPU by demonstrating that the data points can be processed independently and that there is a maximum computational memory footprint of 16 kB per block of threads. Analysis of the performance shows speed increases of over 40× for the algorithms and over 27× including memory copy operations. Additionally, the error associated with using single precision as well as the cubic spline interpolation algorithm is insignificant compared to the magnitude of ARFI displacements ($< 2\%$). We conclude that this data processing approach holds great promise for real-time display of ARFI data as well as for many other ultrasonic research applications.

5

Analysis of Rapid Multi-Focal Zone ARFI Imaging

This paper has been submitted to the journal IEEE Transactions on Ultrasonics, Ferroelectrics and Frequency Control
coauthors: Mark Palmeri, and Kathryn Nightingale

The following chapter describes the development of a new approach to multi-focal zone ARFI imaging as well as its implications on image quality. The data presented were collected using the radiation force image sequence prototyping tool set described in chapter 3.

5.1 Abstract

Acoustic radiation force impulse (ARFI) imaging has shown promise for visualizing structure and pathology within multiple organs; however, because the contrast depends on the push beam excitation width, image quality suffers outside of the region of excitation. Multi-focal zone ARFI imaging has previously been used to extend the ROE, but the increased acquisition duration and acoustic exposure have limited its utility. Supersonic shear wave imaging has previously demonstrated that through technological improvements in ultrasound scanners and power supplies, it is possible to rapidly push at multiple locations prior to tracking displacements, facilitating extended depth of field shear wave sources. Similarly, ARFI imaging can utilize these same radiation force excitations to achieve tight pushing beams with a large depth of field. Finite element method simulations and experimental data are presented demonstrating that single- and rapid multi-focal zone ARFI have comparable image quality (less than 20% loss in contrast), but the multi-focal zone approach has an extended axial region of excitation. Additionally, as compared to single push sequences, the rapid multi-focal zone acquisitions improve the contrast to noise ratio by upwards to 40% in an example 4 mm diameter lesion.

5.2 Introduction

Acoustic radiation force impulse (ARFI) imaging is a well established ultrasonic elasticity imaging modality that has been used to image structure, pathology, and medical procedures in the breast, prostate, liver, heart, and peripheral vessels [70, 72, 100, 121, 92, 36, 35, 31, 28]. By visualizing the mechanical properties of tissue, ARFI imaging provides adjunctive information to B-mode imageing, often with higher contrast. However, ARFI image contrast suffers outside of the region of excitation (ROE) of the push beam due to lower displacement and broader radiation force excitations [71].

To overcome the loss in contrast outside of the ROE, previous studies have acquired multiple separate ARFI images with the push beam focused at different depths, blending the data in post-processing to generate a single image [101, 83]. Although these multi-focal zone sequences can improve overall image quality, there are certain issues with the published implementations. One primary drawback is the significant increase in acquisition duration, which can cause misregistration of the individual focal zone images. ARFI images can require hundreds of milliseconds to acquire one plane [36], thus acquiring multi-focal zone ARFI images can take well over one second, during which cardiac and pulmonary motion could introduce artifacts. Another deficiency of multi-focal zone sequences is increased acoustic exposure and resulting off-time required to maintain FDA-approved acoustic output levels (i.e., the thermal index and temporal average intensity). This increased exposure is due to both the additional long-duration pushing pulses as well as the increased number of tracking pulses required, which can account for upwards of 30% of the total acoustic output.

Shear wave elasticity imaging (SWEI) has previously utilized multiple pushes in rapid succession prior to tracking displacements, creating an extended depth of field in the images [10, 105]. However, these radiation force excitations have not been explored for ARFI imaging and can potentially allow for multi-focal zone imaging without any increase in acquisition duration. Additionally, given the processing and display capabilities of graphics processing unit (GPU) cards, multi-focal zone pushes facilitate higher frame rates for real time ARFI imaging [91]. In this paper, an analysis of the jitter, noise, contrast, and contrast to noise ratio (CNR) is performed to compare single- to rapid multi-focal zone ARFI imaging.

5.3 Background

Acoustic radiation force (ARF) arises from a transfer of momentum from an ultrasonic wave to the medium through which it is traveling due to both absorption and scattering of the wave and is described by [70, 107]

$$\vec{F} = \frac{2\alpha\vec{I}}{c}, \tag{5.1}$$

where α is the acoustic attenuation, $\vec{I}$ is the acoustic intensity, c is the speed of sound, and $\vec{F}$ is the force applied to the medium. ARF-based ultrasound elasticity imaging utilizes this acoustic radiation force by applying focused ultrasound pushing pulses that displace the tissue on the order of microns to oberseve the on-axis displacement (ARFI imaging) [70] or the off-axis shear wave propagation (SWEI imaging) [98].

The focus of this work is ARFI imaging, which uses a beam sequence that begins with acquiring at least one conventional reference A-line in the region of interest, then applying the pushing pulse, and finally acquiring additional tracking A-lines. ARFI images are then generated by repeating the beam sequence over the lateral field of view. The response of the tissue is determined by estimating the displacement of the tissue between the pre-push reference and the post-push tracks within the region of excitation [70]. Stiffer tissues displace less and recover more quickly than softer tissues; thus, ARFI images typically show stiffer tissues as regions of lower displacement.

This dynamic tissue response can be observed since it is relatively slow as compared to acoustic wave propagation; thus, by repeatedly transmitting acoustic waves and monitoring the changes in the phase of the received signal, tissue displacement can be estimated. Additionally, based on the time scale of the tissue dynamics, it is possible to repeatedly excite with radiation force before tracking the tissue displacement, which has been termed a 'supersonic' excitation [10, 105]. For example, typically each radiation force excitation is less than $100\mu s$ and the first observation of tissue motion does not occur until 0.5 ms after force cessation, allowing for up to 5 pushes prior to tracking the resulting motion.

It is also possible, however, that by rapidly applying radiation force excitations, interactions between individual pushes can occur, resulting in pushing on tissue that was not originally located at the desired focus of the excitation beam. For example, if the tissue translates significantly between the pushes, either due to the prior radiation force excitations or due to physiological motion, the radiation force from the later pushes would be applied in the incorrect region, and the resulting ARFI image may be confounded. For the imaging system to be considered spatially invariant, there should be no significant interaction between the pushes [64].

Although this rapidly repeated excitation is possible, previous studies utilizing multi-focal zone ARFI images generated the images in the same fashion as sequential focus B-mode images due primarily to power supply limits [101, 83]. Each focal depth was interrogated individually by acquiring all of the lateral locations with a single focal depth before moving to the next focal depth; the resulting data were then blended in post-processing to create a single image.

5.4 Theory

To determine the impact of the multi-focal zone acquisitions on contrast of a target, a derivation is performed assuming two different focal depths (A and B), where the target is centered at one of the focal depths (A). It has previously been demonstrated that the maximum contrast in an ARFI image is achieved in the region where the push beam is narrowest [71]. Thus, for the target located at focal depth A, the image contrast from focal depth A would be higher than focal depth B, i.e.,

$$Contrast^A = 1 - \frac{\mu_i^A}{\mu_o^A} = \frac{\mu_o^A - \mu_i^A}{\mu_o^A} > \frac{\mu_o^B - \mu_i^B}{\mu_o^B} = 1 - \frac{\mu_i^B}{\mu_o^B} = Contrast^B, \tag{5.2}$$

where μ_o is the mean displacement outside the target, μ_i is the mean displacement inside the target, and the superscript represents the focal zone.

Additionally, assuming small displacements relative to the target size, linear systems applies; thus, it follows that the displacement of the multi-focal zone acquisition will be the sum of the appropriately time-delayed displacements of each focal zone. Therefore, the contrast of the target in the multi-focal zone sequence is given by:

$$Contrast^{AB} = \frac{\mu_o^{AB} - \mu_i^{AB}}{\mu_o^{AB}} = \frac{(\mu_o^A + \mu_o^B) - (\mu_i^A + \mu_i^B)}{\mu_o^A + \mu_o^B} \tag{5.3}$$

$$= 1 - \frac{\mu_i^A + \mu_i^B}{\mu_o^A + \mu_o^B} \tag{5.4}$$

Thus, based on equation 5.2, it can be shown that:

$$1 - \frac{\mu_i^A}{\mu_o^A} > 1 - \frac{\mu_i^A + \mu_i^B}{\mu_o^A + \mu_o^B} \tag{5.5}$$

$$1 - \frac{\mu_i^B}{\mu_o^B} < 1 - \frac{\mu_i^A + \mu_i^B}{\mu_o^A + \mu_o^B} \tag{5.6}$$

Therefore, by combining equations 5.4, 5.5, and 5.6, we have demonstrated that the contrast of the multi-focal zone acquisition is bounded by the contrast of the individual focal zones.

5.5 Methods

5.5.1 Finite Element Method (FEM) Simulations

To investigate whether or not the imaging system is spatially invariant while utilizing rapid multi-focal zone ARFI imaging, previously validated finite element method (FEM) simulations were performed using a model for a prototype Siemens linear array transducer [80]. These simulations were performed to determine the interactions between the different pushing pulses in a uniform medium. A three-dimensional, rectangular, solid mesh was created using LS-PREPOST2 (Livermore Software Technology Corp., Livermore, CA), and the FEM simulations were performed using an explicit time-domain finite element algorithm available in LS-DYNA (Livermore Software Technology Corp., Livermore, CA). A typical high resolution ARFI sequence was simulated: three push beam configurations were defined (5 MHz center frequency, $60\mu s$ duration, F/1.5 focal geometry, focused individually at 15, 20, 25 mm) such that the depth of field, computed as $8F^2\lambda$, overlapped by 1 mm [71].

For each push configuration, Field II was used to determine the three-dimensional radiation force distribution, which was then utilized as the force input to the FEM simulations [51, 84]. Each of the three push configurations was simulated independently in addition to two multi-focus simulations (15 → 20 → 25 mm or 25 → 20 → 15 mm). The multi-focus simulations simulated the pushes with temporal spacing such that there was $40\mu s$ between the cessation of one push and the beginning of the next one, simulating a 10 kHz pulse repetition frequency (PRF). The tissue displacement was then monitored for 5 ms after force cessation.

5.5.2 Experimental Phantom Acquisitions

Experimental phantom data were obtained in a custom designed, calibrated CIRS tissue-mimicking phantom (CIRS, Norfolk, VA) to verify the simulation results as well as analyze the impact of rapid multi-focal zone ARFI imaging on four image quality metrics: displacement jitter, image noise, contrast, and CNR. The phantom has a nominal background stiffness of 8 kPa Young's modulus and attenuation of 0.5 sdB/cm/MHz; it contains a 4 mm diameter cylindrical rod, which is 4x stiffer than the background material, with the center located at 20 mm in depth.

Five different push focal depths were investigated (10, 15, 20, 25, 30 mm), with each push consisting of 300 cycles at 5 MHz. Single focal zone sequences were designed such that data were acquired with a single push at each focal depth and with three pushes at each focal depth. Rapid multi-focal zone sequences were also designed to acquire data for each combination of 3 adjacent focal depths.

Displacement tracking was performed with a 9 MHz, F/3.0 transmit, focused with F/0.5 dynamic receive and 4:1 parallel at a 10 kHz pulse repetition frequency. Raw in-phase and quadrature (IQ) data were recorded using a prototype Siemens linear array and a modified Siemens Acuson SC2000™ ultrasound scanner (Siemens Healthcare, Ultrasound Business Unit, Mountain View, CA, USA). Displacements were estimated using a phase shift algorithm [58, 89].

5.5.3 Image Analysis

To analyze the jitter, contrast, CNR, and image noise, ARFI images of both uniform regions and the cylindrical target were acquired. After the displacement was estimated, multiple pre-processing algorithms were applied; the data were low pass filtered in time with a cutoff frequency of 1000 Hz, depth dependent gain was applied to normalize for the force distribution due to focusing of the push beam, and a 0.25 mm axial and 0.50 mm lateral median filter was applied [27].

After the pre-processing of the data, the mean displacement across the lateral field of view in the uniform region of the phantom was computed. The average displacement through time profiles for the individual foci were then time-delayed according to the timing of the multi-focal zone cases and summed to compare to the combined foci measurements. To estimate the jitter, the standard deviation of the displacement in 2 mm axial regions was computed over the entire acquisition depth and divided by the mean displacement at that depth; thus, the jitter is given in units of decibels relative to the mean displacement and quantified as a function of time after force cessation and depth in the phantom.

The contrast was computed as $1 - (D_i/D_o)$, where D_i is the displacement inside the target and D_o is the displacement outside the target at the same depth in a 4 mm diameter region of interest. The contrast to noise ratio (CNR) was computed in the same region of interest as $(D_i - D_o)/\sqrt{\sigma_i^2 + \sigma_o^2}$ where σ_i is the standard deviation of the displacement inside the target and σ_o is the standard deviation of the displacement outside the target; the overall image noise is therefore defined as $\sqrt{\sigma_i^2 + \sigma_o^2}$. Analyses are performed with comparisons between the single push, single

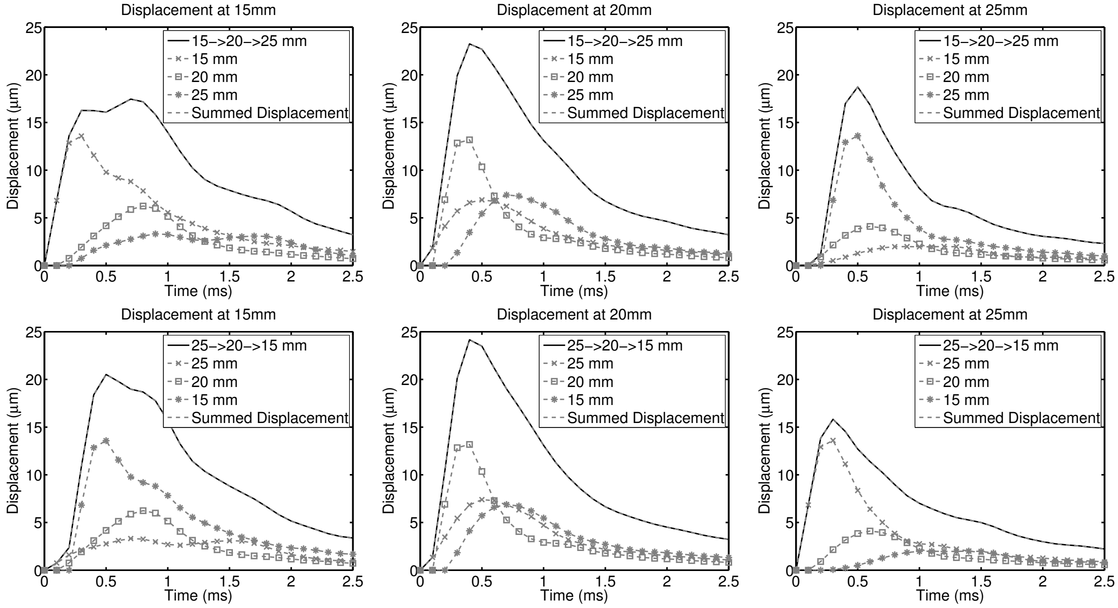

FIGURE 5.1: Simulated displacement though time profiles (without simulated ultrasonic tracking) are shown for each focal configuration and at each focal depth, with the appropriate time delays applied according to when the pushes started in the multi-focal zone configurations. The top row of images compares the profiles when pushing at the shallowest focal depth first and the bottom row of images utilized the deep-to-shallow configuration. In each plot, the dashed gray line indicates the time-delayed and summed output of the three individual focal zone simulations and is nearly identical to the solid black line, which is the multi-focal zone simulation. As expected for a linear system, the RMS difference between the time-delayed and summed displacement profiles and the multi-focal zone simulations is less than $0.01\mu m$ in all configurations.

focal zone, triple push, single focal zone, and rapid multi-focal zone sequences.

5.6 Results

5.6.1 Displacement Dynamics

Finite element method (FEM) simulations were performed per the methods detailed in section 6.4.1 to determine whether or not rapid multi-focal zone ARFI imaging is spatially invariant. Figure 5.1 displays the displacement through time curves for each of the simulations at the individual focal depths (15mm, 20mm, and 25mm), and compares the time-delayed and summed displacement data from each of the

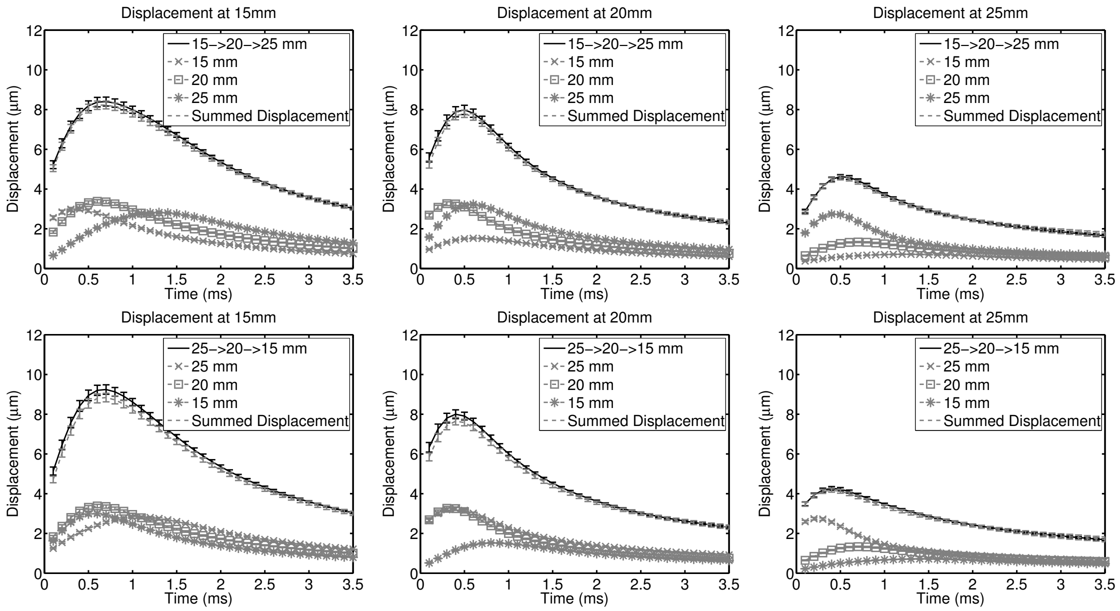

FIGURE 5.2: Experimentally acquired displacement though time profiles in a uniform region of the phantom are shown for each focal configuration and at each focal depth in the same configuration as figure 5.1. The error bars indicate the standard deviation over 9 independent speckle realizations. In each plot, the solid black line (the multi-focal zone data) is in agreement with the dashed gray line (the sum of the individual focal zone acquisitions). The RMS difference through time between the time-delayed and summed displacement profiles and the multi-focal zone acquisitions is less than $0.2\mu m$ in all configurations, which is consistent with the simulations results in figure 5.1.

3 individual focal zone simulations to the rapid multi-focus simulation. The RMS difference between the rapid multi-focal zone simulation and the time-delayed and summed displacement data was computed over the entire simulated region (5-30mm depth) and for each time step independently. As expected for a linear system, the rapid multi-focal zone and summed single zone approaches are effectively the same, with a maximum RMS difference less than $0.01\mu m$.

To incorporate the effects of ultrasonic tracking, matched experimental data were acquired and are shown in figure 5.2, where for each of 9 acquisitions, the displacements were averaged across the field of view and the error bars indicate the standard deviation over the speckle realizations. The multi-focal zone displacement (black

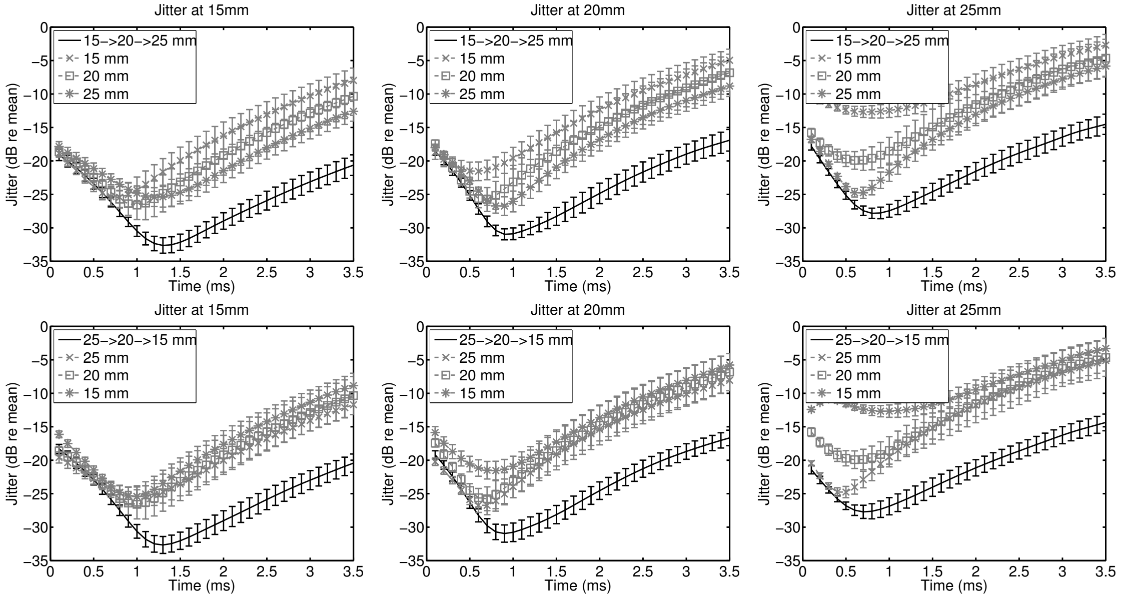

FIGURE 5.3: The jitter magnitude relative to the mean displacement of the experimentally acquired data from figure 5.2 is shown here for each focal depth. For each of the 9 speckle realizations, the jitter was computed independently, and the error bars indicate the standard deviation of the jitter magnitude. Since the jitter magnitude is computed relative to the displacement, a high jitter magnitude is expected whenever the displacement magnitude is low, such as late in time.

line) was compared to the time-delayed and summed single-push individual focal zone data (dashed gray line) with a maximum RMS error of 0.2 μm over all of the configurations.

To evaluate the impact of the multi-focal zone acquisitions on displacement noise, the jitter magnitude was estimated for each focal configuration and is given in figure 5.3 in units of decibels relative to the mean displacement. Viewing the jitter relative to the displacement, it is necessary to interpret figures 5.3 and 5.2 together, such that a high jitter magnitude can corresponds to high noise as well as low displacement magnitude, such as late in time. Overall, the multi-focal zone acquisitions have equivalent or lower jitter than any of the single push, single focal zone acquisitions, indicating that there is minimal negative impact on the displacement signal to noise ratio by utilizing the rapid multi-focal zone acquisitions.

Although the previous comparisons demonstrated the linear combination of the single push, single focal zone sequences into the rapid multi-focal zone sequences, to compare image quality, triple push, single focal zone sequences were also acquired. Example displacement and jitter plots are given in figure 5.4, where each column is a different image and focal depth for the single focal zone sequences, which are then compared to the same rapid multi-focal zone acquisition. In all cases, the triple push sequence has the highest overall displacement; the peak displacement also occurs earlier in time for the single focal zone sequences as compared with the multi-focal zone sequence. The triple push sequences also have lower jitter than the single push sequences. For the two deeper focal depths, the jitter magnitude of both the triple push, single focal zone and the multi-focal zone sequences is similar, however for the shallowest focal depth, after the peak displacement occurs, the jitter magnitude is lower for the multi-focal zone sequence.

5.6.2 Experimental Results

To evaluate the impact of the rapid multi-focal zone approach on CNR, experimental data were collected and processed per the methodology detailed in section 5.5.2. Figure 5.5 shows the typical ARFI image quality achieved with these sequences in the phantom. As expected, the lesion, which is centered at 20 mm, is best visualized in the 20 mm focus and combined focal zone configurations. The single focal zone acquisitions at 10 and 30 mm do not contain the target within their depth of field, so the target is poorly visualized.

After the center of the lesion was identified in each image, the contrast, image noise, and CNR were computed by comparing two 4 mm circular regions at the same depth separated by 8 mm laterally. The image quality metrics were computed for each time step after the push, and an example of the temporal evolution of the contrast, noise, and CNR is given in figure 5.6 for the triple push, single focal

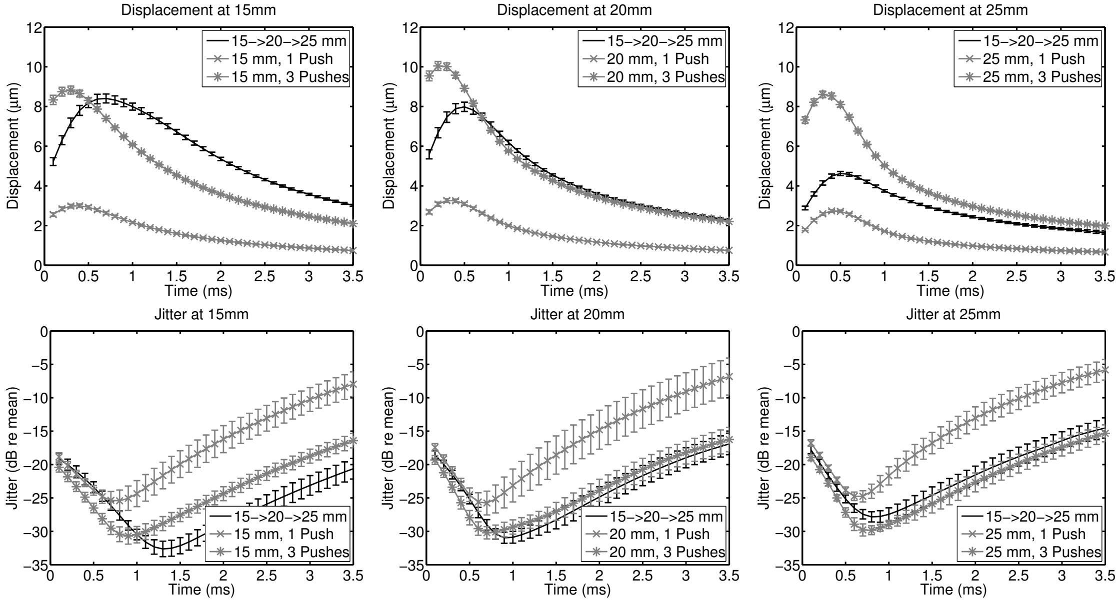

FIGURE 5.4: The experimental displacement amplitude jitter magnitude relative to the mean displacement comparing single push, single focal zone, triple push, single focal zone, and rapid multi-focal zone imaging sequences. For each of the 9 speckle realizations, the displacement magnitude and jitter was computed independently, and the error bars indicate the standard deviation of the jitter magnitude. The triple push sequence has the highest overall displacement and its peak displacement occurs earlier in time as compared with the multi-focal zone sequence.

zone sequence, where the error bars indicate the standard deviation over 9 speckle realizations. In figure 5.6, the peak contrast occurs early in time using the 20 mm focus sequence, however because the noise decreases later in time, when the contrast of the 25 mm focus sequence is peaking, the maximum CNR is achieved later in time using the 25 mm focus sequence.

Given the temporal evolution of both contrast and CNR, to evaluate both of these image metrics, the maximum values through time were extracted, along with the image noise at those time steps. Figure 5.7 shows the mean and standard deviation of the contrast, noise, and CNR over 9 independent speckle realizations for the time step associated with the maximum image contrast. For the multi-focal zone sequences, the black bars indicate pushing at the shallowest focal depth first, then the middle

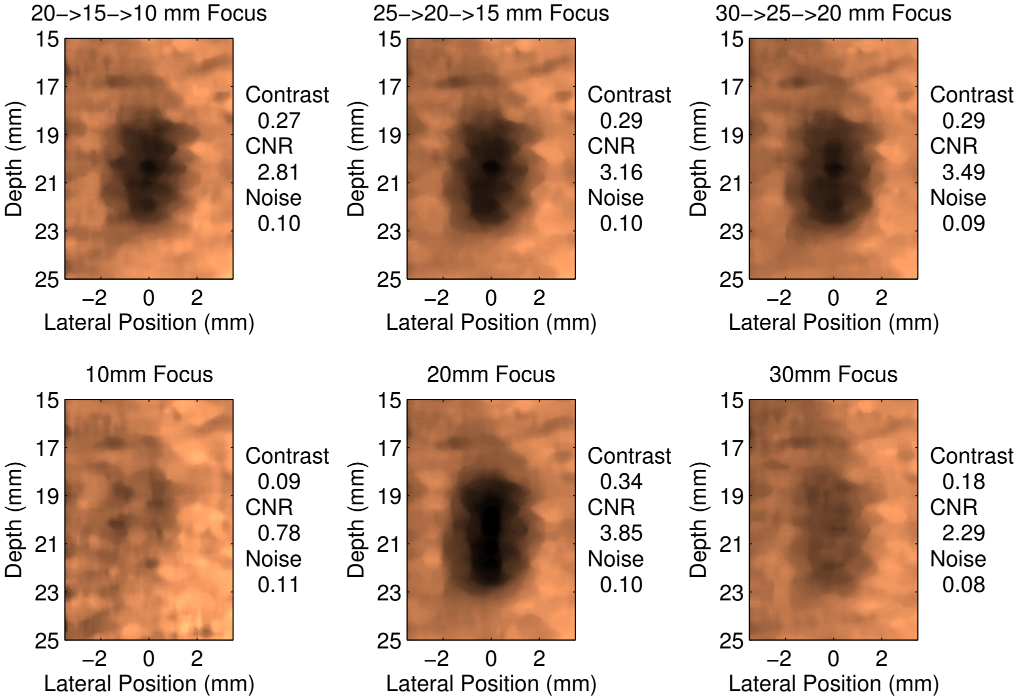

FIGURE 5.5: Experimentally acquired ARFI images of the 4 mm cylindrical target, displayed 0.6 ms after force cessation. The top row of images shows 3 different multi-focal zone sequences and the bottom row displays the triple push, single focal zone acquisitions. Comparable image quality is achieved in all of the multi-focal zone sequences since each configuration included the 20 mm focal depth, which is centered on the lesion. Conversely, as demonstrated by the 10 mm and 30 mm single focal zone acquisitions, when the push is only focused away from the target, the image quality is severely degraded.

focal depth, and finally at the deepest focal depth; the gray bars indicate pushing in the opposite order. For the single focal zone sequences, the black bars display the data associated with the single push sequences and the gray bars indicate the data for the triple push sequences. Using the data from figure 5.7, paired Student's two-tailed t-tests were performed between the contrast values for the 20 mm triple push, single focal zone acquisition and all of the other focal configurations, which showed statistically significantly higher contrast ($p < 0.01$, top plot, figure 5.7). However, by limiting the comparison to only the rapid multi-focal zone and single push sequences, the 20 mm, single push sequence had the highest contrast ($p < 0.01$,

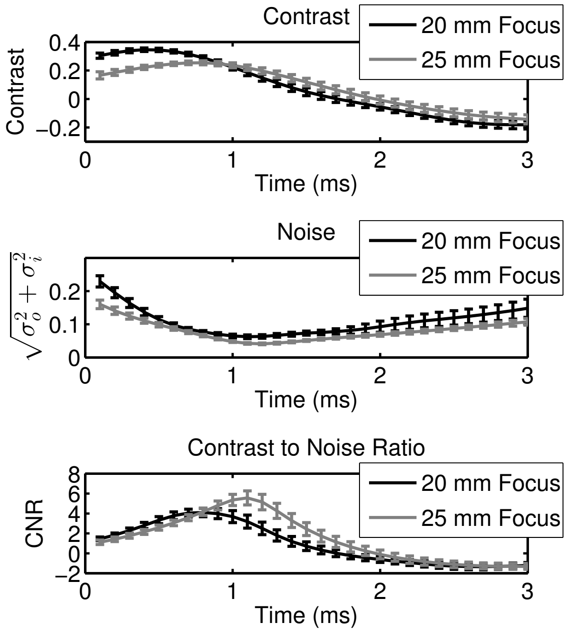

FIGURE 5.6: Contrast, noise, and CNR of the 4 mm cylindrical target are given, where the error bars indicate the standard deviation over 9 independent speckle realizations. The data are shown as a function of time for the triple push, single focal zone sequences at 20 mm and 25 mm. The 20 mm focus has the highest contrast, but the 25 mm focus sequence has the highest CNR due to the temporal evolution of both the contrast and the image noise.

top plot, figure 5.7).

Constructed in the same manner as figure 5.7, figure 5.8 displays the contrast, noise, and CNR for each sequence from the time step associated with the maximum CNR. As shown in figure 5.6, this time step is usually different than the one used for the maximum contrast. Paired Student's two-tailed t-tests were again performed, yielding that the triple push, 25 mm focal zone had the highest CNR of all of the sequences. However, comparing the rapid multi-focal zone sequences to only the single push sequences, the 30 → 25 → 20 mm combined focal zone acquisition had the highest CNR ($p < 0.01$, bottom plot, figure 5.8).

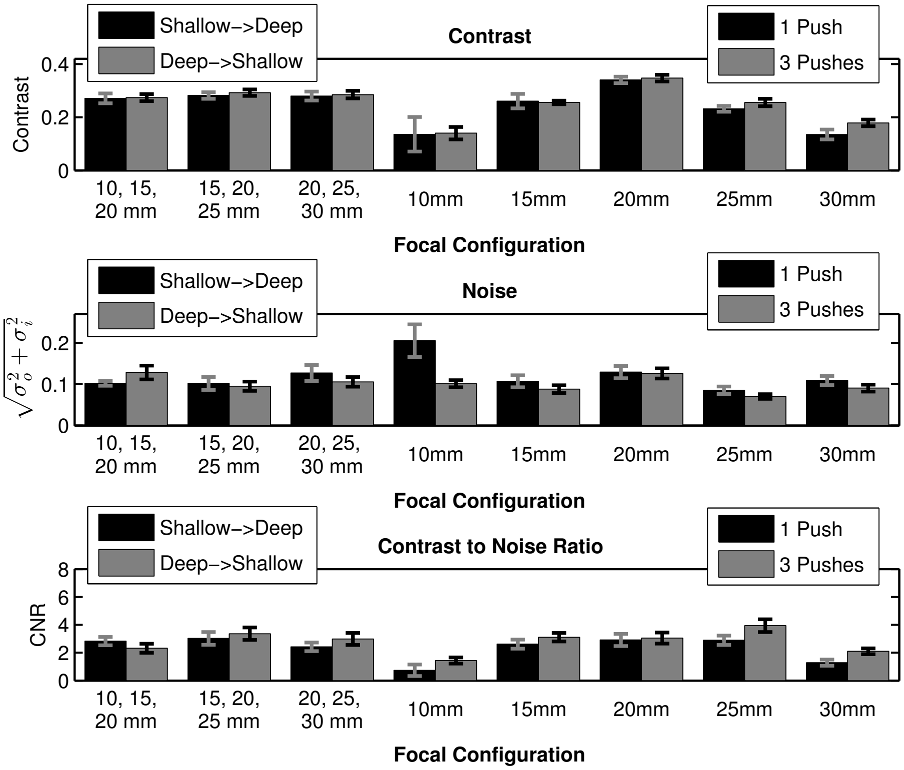

FIGURE 5.7: Contrast, noise, and CNR of the 4 mm cylindrical target are given, where the error bars indicate the standard deviation over 9 independent speckle realizations. The bar plots portray the data from the time step where the maximum contrast through time was observed. As expected per the derivation in 5.4, the 20 mm push focal configuration yields the highest contrast (paired Student's two-tailed t-test, $p < 0.01$).

5.7 Discussion

Through the development of technological improvements in ultrasound scanners and power supplies, rapid multi-focal zone ARFI imaging is now possible, allowing extended regions of interest without any increase in acquisition time. Additionally, depending on the relative positions of the focal zones and the target being imaged, there is either minimal degradation or improvement of image quality based on the CNR of target as compared to a single push, single focal zone images.

By rapidly pushing at multiple focal depths, the displacements sum linearly at each depth as shown in figures 5.1 and 5.2. In the FEM simulations, the match

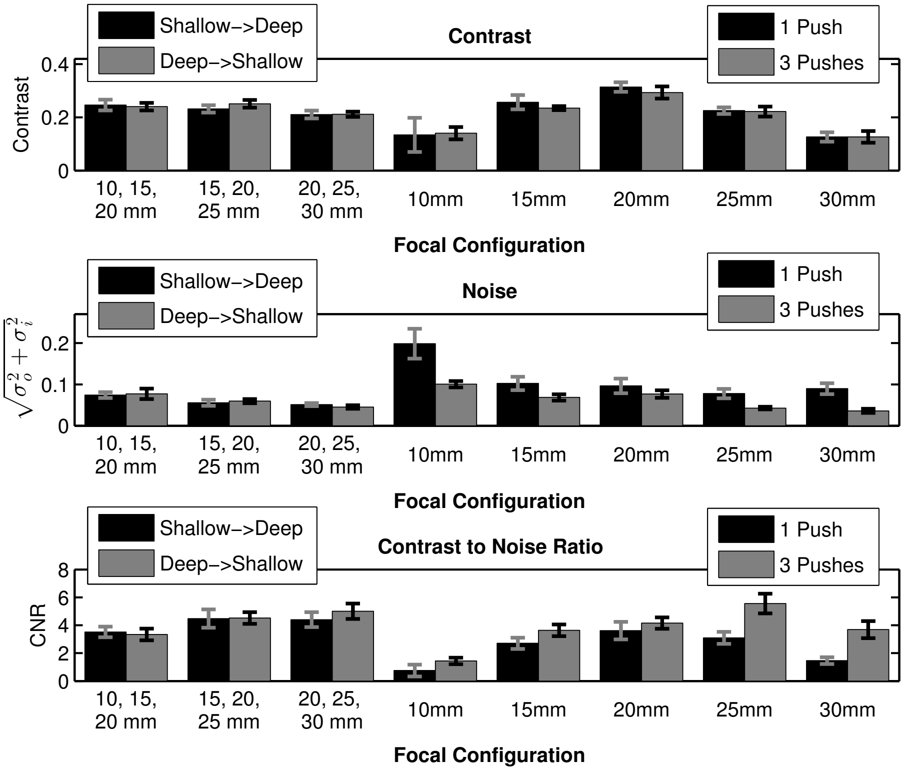

FIGURE 5.8: Contrast, noise, and CNR of the 4 mm cylindrical target are given, where the error bars indicate the standard deviation over 9 independent speckle realizations. The bar plots portray the data form the time step where the maximum CNR through time was observed. In many of the focal configurations, by looking later in time after force cessation, the noise decreases, increasing the CNR of the target. The triple push, 25 mm focus sequence had the highest CNR (paired Student's two-tailed t-test, $p < 0.01$), but comparing the multi-focal zone sequences to the single push, single focal zone sequences, the 20 → 25 → 30 mm combined focal zone acquisition had the highest CNR ($p < 0.01$).

between the summed individual profiles and the simulated multi-focal zone pushes was nearly perfect (RMS error $< 0.01\mu m$), indicating that multi-focal zone pushes maintain spatial invariance since the displacements induced are small compared to the distance between the focal depths. In the experimental data, the time-delayed and summed displacement data had slightly lower displacement magnitude early in time as compared to the multi-focal zone acquisitions. We hypothesize that this discrepancy arises from underestimation of the tissue motion due to ultrasonic tracking and resulting shearing under the point spread function (PSF) [61, 80]. The single focal zone acquisitions have relatively higher shearing under the PSF near the focus of each push as compared to the multi-focal zone pushes, which have a slightly broadened push beam due to the superposition of the focal geometries of all of the pushes [61, 80].

Although the displacement magnitude sums linearly when using multi-focal zone configurations, the relative jitter magnitude is similar early in time to the single focal zone acquisitions, as demonstrated in figure 5.3. This result is expected since the only primary source of jitter that is impacted by the multi-focal zone acquisitions is the correlation coefficient, which is related to shearing under the point spread function [111, 84]. The multi-focal zone acquisitions increase the displacement magnitude, but they do not increase the shearing of the tissue due to the relatively broader pushes. As discussed earlier, it is hypothesized that the rapid multi-focal zone pushes slightly decrease the shearing under the PSF; however, for the jitter magnitude early in time, there are no significant differences since the error bars overlap.

Given the increased quantity of acoustic energy used in the multi-focal zone sequences, the larger displacement magnitudes for all of the focal depths were expected. However, to analyze the results assuming a finite amount of acoustic energy, the rapid multi-focal zone sequences were compared to the triple push, single focal zone sequences in figure 5.4. In all cases, it is apparent that the triple push, single focal zone sequences have the highest displacement and lowest jitter early in time. However, since the peak displacement for the rapid multi-focal zone sequences occurs later in time, the relative jitter magnitude can be lower, as demonstrated in 15 mm subfigure (bottom left plot, figure 5.4).

The comparison between sequences was then extended to the image quality metrics of contrast, noise, and CNR. Figure 5.6 demonstrates the temporal evolution of these metrics after force cessation, which indicates that the maximum contrast and the maximum CNR are achieved both with different sequences and at different times. The maximum CNR consistently occurs later in time than the maximum contrast due to the reduction in image noise that occurs as the shearing under the tracking PSF decreases with time, while the displacement at the target is still high.

The contrast, noise, and CNR were then evaluated for all of the different sequences, looking at data from the time step associated with the maximum contrast or the maximum CNR. For the maximum contrast data (figure 5.7), the triple push, 20 mm focus had the highest target contrast ($p < 0.01$, top plot, figure 5.7), and if the triple push sequences are removed from the analysis, the single push, 20 mm focus has the highest contrast ($p < 0.01$, top plot, figure 5.7). These results are consistent with the derivation presented in section 5.4 (equation 5.5), confirming that the use of multi-focal zone ARFI imaging degrades the maximum contrast achievable in a ARFI image.

However, figure 5.7 (bottom plot) also demonstrates that the maximum CNR is highly dependent on the noise level, which decreases later in time and can be reduced by utilizing either the triple push sequences or multi-focal zone ARFI imaging. Specifically, figure 5.8 displays the data from the time step associated with the maximum CNR for each sequence. Overall, the triple push sequence focused at 25 mm has the highest CNR ($p < 0.01$, bottom plot, figure 5.8), and if the triple push sequences are removed from the analysis, the CNR when using the $30 \rightarrow 25 \rightarrow 20$ mm combined focal zone is highest ($p < 0.01$, bottom plot, figure 5.8).

Analyzing the data in figures 5.7 and 5.8, two primary conclusions can be drawn: to achieve maximum contrast, the radiation force excitation should be focused at the center of the target, but to achieve maximum CNR, the push should focused slightly below the target using the maximum amount of available energy. Generally, CNR is a better indicator of image quality than contrast since it incorporates target conspicuity, however, it is also noteworthy that the maximum CNR occurs later in time than the maximum contrast, at which point the lesion size may be incorrect [71].

As compared to the single focal zone sequences, the rapid multi-focal zone sequences yield consistent image quality throughout a much larger excitation depth, which would result in overall better image quality for targets larger than the single focal zone depth of field or if the exact depth of the target was unknown. Additionally, as compared to the single push, single focal zone sequences, the rapid multi-focal zone sequences can have a higher CNR (bottom plot, figure 5.8), and all of the sequences have less than 20% loss in the target contrast (top plot, figure 5.7) as compared to the 20 mm focus sequence.

An alternative interpretation of rapid multi-focal zone imaging is as an optimization parameter since it extends the depth of field of the ARFI image, while not increasing the acquisition duration. Thus, if a certain depth of field for the image is desired, the F-number for a single focal zone sequence can be computed, but multiple rapid multi-focal zone sequences could also be designed, which would have narrower excitation beams, and therefore potentially improved image quality [71], which is similar to the advantage that arises from the use of the 'supersonic' excitations for SWEI [105].

Lastly, comparing the rapid multi-focal zone approach to previously published multi-focal zone ARFI imaging methods, any potential motion artifact is reduced since the data is acquired in $1/N$ amount of time, where N is the number of focal zones. Additionally, the overall acoustic exposure is reduced since fewer tracking pulses are required, which can consist of over 30% of the total acoustic energy output.

5.8 Conclusions

In this paper, we have performed an analysis of the displacement magnitude, noise, contrast, and CNR to compare single- and rapid multi-focal zone ARFI imaging. By utilizing rapid multi-focal zone ARFI imaging, the depth of field in the images is extended beyond that of a single focal zone without decreasing frame rate, the CNR of targets within the region of excitation can increase by upwards to 40%, and the acquisition duration is significantly lower compared to conventional blended images, reducing potential motion artifacts. Thus, we conclude rapid multi-focal zone acquisitions can improve overall image quality, depending on the imaging conditions and the size of the target being image, but the implementation of rapid multi-focal zone imaging is contingent upon an adequate power supply and sufficiently low acoustic energy exposure.

6

An Adaptive Filter for Shear Wave Speed Estimation Using a Maximum a Posteriori Estimator

This paper has been submitted to the journal IEEE Transactions on Ultrasonics, Ferroelectrics and Frequency Control
coauthors: Ned Rouze, Brett Byram, Mark Palmeri, and Kathryn Nightingale

The previous chapter detailed a method to rapidly acquire high quality ARFI images with a large depth of field; however, it did not investigate any methods for improving SWEI image quality. Thus, this chapter describes the development of an adaptive filter using a maximum *a posteriori* estimator to reduce the noise in SWEI images.

6.1 Abstract

Shear wave elasticity imaging (SWEI) has shown promise for visualizing structure and pathology within multiple organs; however, due to the desire for high resolution images, time-of-flight based algorithms can result in significant image noise because of the limited number of samples used to estimate the shear wave speed. The *maximum*

a posteriori estimator (MAPE) provides a framework for Bayesian estimation of the shear wave speed in order to reduce noise present in SWEI images. Ultrasonically tracked, finite element method simulations were employed herein to investigate the bias and variance of the MAPE filtered shear wave speed estimates compared to least squares linear regression. Additionally, the adaptive filter is shown to provide consistent image quality improvements even while varying the input parameters over an order of magnitude away from the optimal values. As compared with conventional SWEI images, the MAPE filtered images demonstrate improvements upwards of 16 dB in the contrast to noise ratio of simulated spherical lesions, while requiring only 10-30 seconds of additional data processing.

6.2 Introduction

Shear wave elasticity imaging (SWEI) is an ultrasound elasticity imaging technique that has shown promise for visualizing structure and pathology within multiple organs, including prostate, breast, muscle, liver and thyroid [120, 7, 4, 25, 105, 26, 42, 81, 112, 93, 8, 68, 13]. SWEI images are generated by estimating the transverse wave speed within the tissue after inducing broadband or periodic motion [98]. The shear or Young's modulus of the tissue can then be computed based on underlying assumptions about the tissue and wave propagation [98].

To induce shear waves within the tissue, focused ultrasonic beams generating acoustic radiation force (ARF) are widely utilized to generate broadband shear waves [98, 32], although other mechanical excitation sources such as external vibrators have also been investigated [110, 124]. For ARF-based shear waves, the propagation is monitored utilizing ultrasound to observe the dynamic displacement of the tissue spatially offset from the excitation. The shear wave velocity is commonly estimated utilizing time-of-flight based reconstruction algorithms that assume a known direction of wave propagation and homogeneous, isotropic tissue within the reconstruction kernel [81, 10]. Violation of these assumptions can lead to biased shear wave speed estimates and image artifacts generated by reflected waves at structural boundaries [30, 95].

Although these issues exist with time-of-flight based reconstruction techniques, these methods are widely used because of their ease of implementation and because ultrasound typically only provides in-plane information when monitoring tissue displacement. In contrast, when utilizing 3D data such as that acquired with magnetic resonance elastography, it is possible to do a direct inversion of the 3D wave equation to determine the shear modulus [74].

To reduce image artifacts and improve spatial resolution when using time-of-flight based algorithms, smaller reconstruction kernels can be used, however with fewer estimates of the wave propagation, the noise level increases as well. One method for reducing image noise that is typically employed is a two-dimensional median filter [95]; however, this method assumes a constant amount of noise at every pixel and does not take into account spatially varying noise profiles, which are typical when imaging heterogeneous tissue. An alternative approach for is to use a maximum *a posteriori* estimator (MAPE), which have been utilized as image processing techniques to reduce the noise in images [14, 15]. In this work, a maximum *a posteriori* estimator for shear wave speed is investigated as an adaptive filter to reduce the noise in SWEI images.

6.3 Background

6.3.1 Acoustic Radiation Force Induced Shear Wave Propagation

Acoustic radiation force (ARF) arises from a transfer of momentum from a sound wave to the medium through which it is traveling due to both absorption and scattering of the wave and is described by [70, 107]

$$\vec{F} = \frac{2\alpha\vec{I}}{c}, \tag{6.1}$$

where α is the acoustic attenuation, $\vec{I}$ is the acoustic intensity, c is the speed of sound, and $\vec{F}$ is the force applied to the medium. SWEI utilizes this acoustic radiation force by applying ultrasonic pushing pulses that displace the tissue on the order of microns [70] and tracking the propagation of the transverse wave that propagates away from the region of excitation [98].

A typical ARF-induced shear wave beam sequence begins with acquiring at least one conventional reference A-line in the region of interest (ROI), then applying the pushing pulse away from the ROI, and finally acquiring additional tracking A-lines. The response of the tissue is determined by estimating the displacement of the tissue between the pre-push reference and the post-push tracks [70]. By observing how the shear wave propagates over multiple lateral locations, it is possible to estimate the shear wave speed. Under the assumptions of homogeneous, linear elastic, incompressible, isotropic tissue, the shear modulus (G) is equal to three times the Young's modulus (E), and also equal to the density of the tissue (ρ) times the shear wave speed (S) squared (i.e., $G = 3E = \rho S^2$). Thus, stiffer tissues have a higher shear wave speed than soft tissues, and by creating images of the shear wave speed, or derived shear or Young's modulus, the image contrast is related to the stiffness of the underlying tissue.

To estimate the shear wave speed, it is necessary to determine the wave arrival time at each lateral and axial location. Multiple methods exist for determining this wave arrival time, such as time-to-peak tissue displacement, time-to-peak tissue velocity, and cross-correlation between the displacement or velocity profiles at each lateral location [81, 95, 21, 62, 56]. Typically, these wave arrival time estimates are then input into a time-of-flight algorithm, such as linear regression or random sample consensus, which fits the data to a model assuming a single shear wave speed across the lateral and axial field of view [94, 113]. Specifically, linear regression is a maximum likelihood estimator that assumes a linear relationship between the arrival time at each lateral location and the speed of the shear wave. In structured media, to obtain high resolution, small regression kernels are desired, but this leads to increased noise in the estimated shear wave speed. One method to reduce this noise is to recast the estimation problem as a Bayesian problem to also include prior information about the expected local smoothness of the reconstructed shear wave speed images.

6.3.2 Maximum Likelihood Estimate of SWS Images

The development of the MAPE is based off of the traditional time-of-flight based algorithms [81] and begins by considering linear regression, which is a maximum likelihood estimator (MLE) for shear wave speed. To relate the shear wave speed to the wave arrival times, the tissue within the reconstruction kernel is assumed to be homogeneous and isotropic such that the wave arrival times are linearly related to the shear wave speed. This relationship is given by:

$$T_k = \left(\frac{x_k}{S} + b\right), \tag{6.2}$$

where T_k is the measured wave arrival time at position x_k with shear wave speed S, and y-intercept b, which is the amount of time required for the shear wave to start propagating away from the region of excitation.

However, equation 6.2 does not account for any noise in the system. Assuming the wave arrival time estimates are Gaussian distributed [112] and considering all of the data within the reconstruction kernel K, the probability that the set of wave arrival times ($T = (T_k | k \in K)$) was measured given the shear wave speed (S) and intercept (b) is the product of a set of exponential functions, known as the likelihood function:

$$P(T|S) = \prod_{k \in K} exp\left(-\frac{\left(T_k - \left(\frac{x_k}{S} + b\right)\right)^2}{2\sigma^2}\right). \tag{6.3}$$

The MLE estimate of the shear wave speed is the value for which equation 6.3 is maximized. By taking the logarithm of both sides, a more tractable version of the equation is obtained:

$$\log(P(T|S)) = \sum_{k \in K} exp\left(-\frac{\left(T_k - \left(\frac{x_k}{S} + b\right)\right)^2}{2\sigma^2}\right), \tag{6.4}$$

which is known as the log-likelihood function.

Both b and S can be solved for by taking the respective derivatives and setting the equations equal to zero. The resulting solution for the MLE estimate, $\hat{S}$, is equation 6.5, which is least squares linear regression.

$$\hat{S} = \frac{\sum_{k \in K} (\tilde{x}_k^2)}{\sum_{k \in K} \left(\tilde{T}_k \tilde{x}_k\right)} \qquad \tilde{T}_k = T_k - \frac{1}{k} \sum_{k \in K} T_k \qquad \tilde{x}_k = x_k - \frac{1}{k} \sum_{k \in K} x_k \tag{6.5}$$

To obtain a SWEI image, the MLE must take into account the data at each pixel, which mathematically yields the combined probability in equation 6.6. In this equation, the subscript i indicates the value at a given pixel in the image. The shear wave speed (S_i), y-intercept (b_i) and reconstruction kernel (K_i) are all a function of the pixel number, but the positions (x_k) and associated wave arrival time data (T_k) are not. The likelihood function for the entire image (equation 6.6) is the product of the likelihood functions for each individual pixel (equation 6.3). Again considering the log-likelihood function, equation 6.7 must now be maximized to determine the MLE estimate for the SWEI image.

$$P(T|S) = \prod_{i} P(T|S_i) \tag{6.6}$$

$$\log(P(T|S)) = \sum_i \log(P(T|S_i)) = \sum_i \left(\sum_{k \in K_i} exp \left(-\frac{\left(T_k - \left(\frac{x_k}{S_i} + b_i\right)\right)^2}{2\sigma_i^2} \right) \right) \tag{6.7}$$

Since equation 6.7 is a summation and each term is independent, they can be maximized individually. Therefore, the resulting solution for the MLE estimate at a given pixel ($\hat{S}_i$) is still equation 6.5.

6.3.3 Maximum a Posteriori *Estimate of SWS Images*

The least squares linear regression log-likelihood function (equation 6.7) can be used to develop a maximum *a posteriori* estimator (MAPE) by combining it with a prior probability, $P(S)$, for the image. In this formulation, equation 6.8 gives the log-likelihood function that must be optimized, with an arbitrary prior distribution.

$$\log(P(T|S)P(S)) = \sum_i (\log P(T|S_i) + \log P(S_i)) \tag{6.8}$$

One prior distribution that can be used is an exponential function [14]:

$$\log(P(S_i)) = \sum_{j \in N_i} \left(\frac{-a_{ij}}{\gamma} \left| \frac{1}{S_i} - \frac{1}{S_j} \right| \right), \tag{6.9}$$

where a_{ij} is the weight of pixels in the neighborhood N_i and γ characterizes the width of the exponential function. This prior distribution introduces a penalty term when the shear wave speed within a neighborhood is not uniform.

The MAPE estimate, $\hat{S}_{MAPE}$, is the maximum value over the domain S after substituting the likelihood function and prior distribution into equation 6.8, resulting in equation 6.10. Since the terms in the summation are not independent, to solve for $\hat{S}_{MAPE}$, an optimization algorithm must be utilized such as conjugate gradient descent [47] or iterative coordinate descent [15].

$$\hat{S}_{MAPE} = \underset{S}{argmax} \sum_{i} \left(\sum_{k \in K_i} \left(- \frac{\left(T_k - \left(\frac{x_k}{S_i} + b_i \right) \right)^2}{2\sigma_i^2} \right) + \sum_{j \in N_i} \left(\frac{-a_{ij}}{\gamma} \left| \frac{1}{S_i} - \frac{1}{S_j} \right| \right) \right) \tag{6.10}$$

6.4 Methods

6.4.1 Finite Element Method (FEM) Simulations

Previously validated finite element method (FEM) simulations were adapted to analyze the performance of the MAPE for shear wave speed estimation [85, 84]. A three-dimensional, rectangular, solid mesh was created for the FEM simulations with dimensions of 18 mm laterally (x), 10 mm in elevation (y), and 40 mm axially (z) using LS-PREPOST2 (Livermore Software Technology Corp., Livermore, CA), such that each element was cubic with a side length of 0.2 mm. The boundary conditions of the mesh were defined to have quarter-symmetry about the lateral and elevation faces of the mesh ($x - z$ plane, $y = 0$ mm and $y - z$ plane, $x = 0$ mm) and non-reflecting boundary conditions on the back faces ($x - z$ plane, $y = 10$ mm and $y - z$ plane, $x = 18$ mm). Full constraints were assumed for the top and bottom of the mesh ($x - y$ plane, $z = 0$ mm and $x - y$ plane, $z = 40$ mm).

The FEM mesh was defined to simulate stiff spherical lesions ranging from 4 mm to 8 mm in diameter, such that the center of the lesion was located 9 mm laterally from the mesh boundary ($x = 9$ mm, $y = 0$ mm, $z = 20$ mm). The background tissue was modeled as a homogeneous material with a Young's modulus of 7.2 kPa. Each size lesion was simulated to be 2x, 3x, 4x, 6x, and 8x stiffer than the background.

Field II was used to simulate a linear array transducer with a F/2.5, 4.6 MHz, 65 μs pushing pulse focused at 20 mm ($x = 0$ mm, $y = 0$ mm, $z = 20$ mm) [84, 51]. After obtaining the three-dimensional acoustic intensity profile, the force was computed per equation 6.1 at each node in the mesh, scaled by the uniform element volume. The pushing pulse was simulated such that as the shear wave propagated away from the region of excitation it would pass through the spherical lesion.

The FEM simulations were performed using an explicit time-domain finite element algorithm available in LS-DYNA (Livermore Software Technology Corp., Livermore, CA); the total time simulated was 12 ms, and nodal displacement data were saved every 0.1 ms, corresponding to a 10 kHz sampling rate. Ultrasonic tracking was then simulated using Field II and the displacement data output from the FEM simulation; the same linear array transducer definition was used, but with a F/2 transmit focal geometry, 7 MHz, 1-cycle excitation, with F/0.5 dynamic receive and receive aperture growth [84, 51]. The output of the Field II simulation was a set of radio-frequency (RF) A-lines, and normalized cross-correlation was used to estimate the tissue displacement with a kernel length and search region of 1.5× and 0.4× the acoustic wavelength, respectively [89]. For each FEM simulation, ten speckle realizations were simulated using Field II.

An example of the simulated, ultrasonically tracked shear wave propagation through the 6 mm, 28.8 kPa Young's modulus lesion is given in figure 6.1. Observing the shear wave 1.0 and 3.0 ms after the radiation force excitation, the wavefront is nearly vertical since the background tissue is homogeneous. Once the shear wave enters the stiffer lesion, part of the shear wave energy is reflected at the boundary, and the wavefront bends to accommodate the faster speed inside the lesion, as seen in the 5.0 ms figure. As the shear wave exits the lesion, additional energy is again reflected, and on the far side of the lesion at 9.0 ms, two shear wavefronts can be observed, one corresponding to the wave that propagated through the lesion, the other to the wave that propagated around the lesion only in the background material.

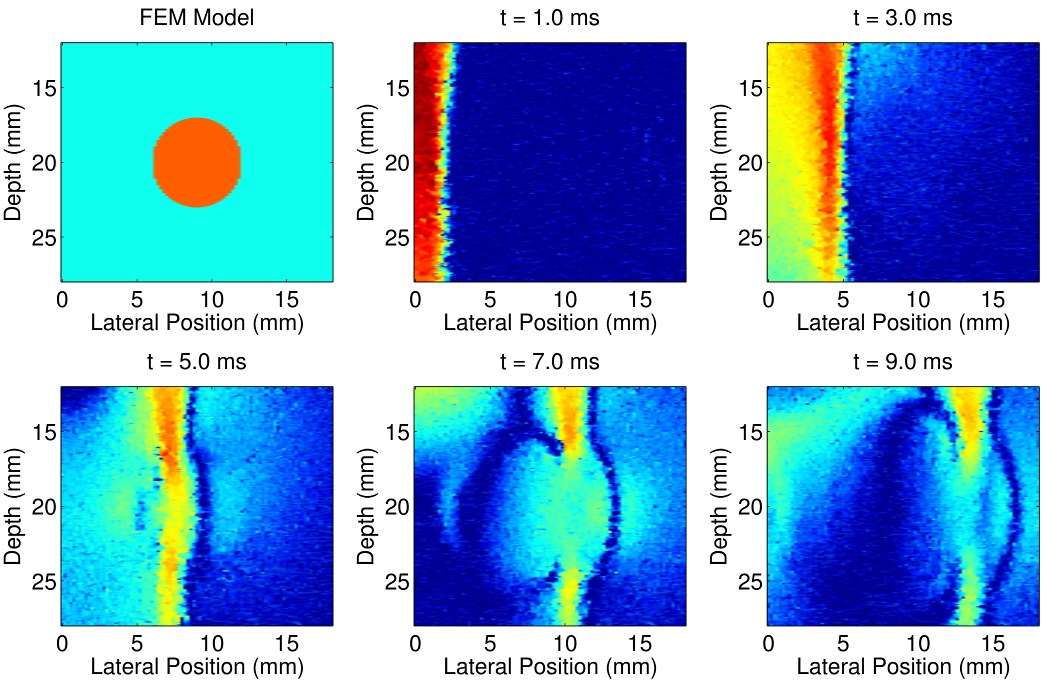

FIGURE 6.1: Example FEM mesh of the 6 mm, 28.8 kPa Young's modulus lesion (top left) and ultrasonically tracked displacement at 5 time points after the simulated radiation force excitation (the displacements are on a decibel scale, [-20, 20] dB re 1 μm). The shear wave propagates left to right, and as seen at 1.0 and 3.0 ms after the excitation, the wavefront is nearly vertical; however later in time as the shear wave enters the lesion, the wavefront bends since the speed is greater within the lesion than the background.

6.4.2 Wave Arrival Time Estimation

After displacement estimation, multiple data processing steps were applied to obtain the estimates for the wave arrival time. First, a correlation coefficient filter was applied to remove data with correlation coefficients below 0.995; the removed data points were then interpolated from the surrounding data. Next, a 0.75 mm axial median filter was applied, the data were differentiated to determine the tissue velocity, and a second-order low-pass Butterworth filter with a 1000 Hz cutoff frequency was applied to remove high frequency jitter from the velocity data at each pixel [94]. The data were then downsampled spatially to 0.1 × 0.2 mm axial by lateral, and upsampled temporally to a sample rate of 50 kHz. Finally, a directional filter was applied to each axial plane individually to isolate the right propagating shear waves [30].

The wave arrival time (T_k) for each lateral position (x_k) was determined at each depth individually by first estimating the incremental wave arrival time between adjacent lateral positions, and then calculating the cumulative sum of the incremental arrival times to determine the absolute wave arrival time. For adjacent lateral positions, the incremental arrival time ($T_{k+1} - T_k$) was estimated by performing cross-correlation between the upsampled velocity vs. time waveforms for each pair of adjacent lateral locations [21]. After the maximum correlation was found, a parabolic sub-sample estimator was used to obtain the final estimate of the wave arrival time. The cumulative sum of the incremental wave arrival times were then used to estimate the shear wave speed at each spatial location.

The example data set from figure 6.1 was plotted as a function of time and lateral position for a homogeneous region (13 mm axially) and a region with the simulated 6 mm, 28.8 kPa inclusion (20 mm axially) in the two top images in figure 6.2. The homogeneous region (figure 6.2, top left) has a smooth wavefront as the shear wave propagates across all of the lateral positions. The difference in shear wave speed in the region with the inclusion is clearly visible as the wavefront propagates through a larger lateral region in the same amount of time (figure 6.2, top right); additionally, the secondary wavefront on the far side of the lesion is also visible here.

The bottom plots of figure 6.2 show the cross-correlation method for computing the incremental wave arrival time between successive lateral positions. In each of these plots, the cross-correlation between the velocity versus time waveforms was obtained, and after using the parabolic sub-sample estimator, a ΔT value was computed corresponding to the time for the shear wave to propagate from one lateral position to the next.

The incremental wave arrival time for each pixel in the image was obtained and is shown in the left image of figure 6.3. Although this image is very noisy, the

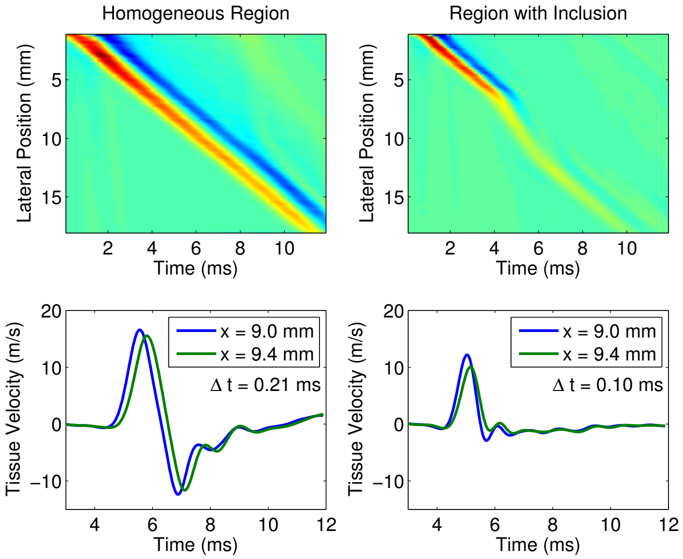

FIGURE 6.2: Tissue velocity after ultrasonic tracking, pre-processing, and directional filtering is given as a function of lateral position and time for a homogeneous region (top left) and a region with a 6 mm, 28.8 kPa inclusion (top right). The region with the inclusion has multiple shear wave speeds as seen in the bending of the wavefront at 6 mm and 12 mm laterally. The bottom plots of tissue velocity versus time demonstrate the computation of the incremental wave arrival time between adjacent lateral locations using cross-correlation and a parabolic sub-sample estimator. In this case, the region with the stiff inclusion has an incremental wave arrival time of less than half that of the homogeneous region.

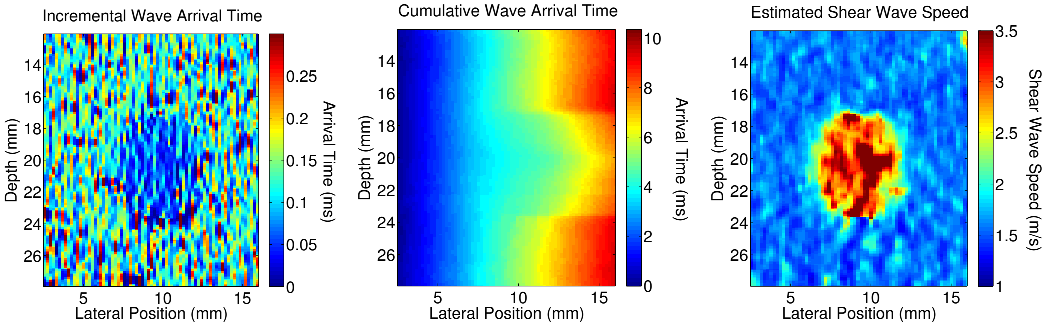

FIGURE 6.3: The incremental (left image) and cumulative (middle image) wave arrival times are given as a function of lateral and axial position. The incremental wave arrival time image is the raw output from the cross-correlation demonstrated in figure 6.2; however due to the noise in this data, to estimate the shear wave speed, the slope of the linear regression of the cumulative wave arrival time data is typically used and is shown in the right image with a 1.5 mm lateral regression kernel.

lesion is still visible, however, to obtain robust estimates of the shear wave speed, linear regression is typically performed as a function of lateral positions using the cumulative wave arrival time data (middle image, figure 6.3), with the slope of the regression corresponding to the estimated shear wave speed (right image, figure 6.3).

6.4.3 Shear Wave Speed Estimation Algorithms

Time-of-flight algorithms typically perform a least squares linear regression of the wave arrival time data versus lateral position to estimate the shear wave speed. In contrast, the proposed adaptive filter utilizes a posterior distribution comprised of the likelihood function from least squares linear regression combined with an exponential prior distribution as detailed in section 6.3.3 [14, 15]. The prior distribution provides a spatial continuity constraint for the image by comparing the shear wave speed at each pixel with the surrounding pixels in a given neighborhood using a previously determined model for the expected amount of noise in the linear regression estimates.

For each simulated speckle realization of the FEM simulations, the least squares linear regression shear wave speed image was computed using regression kernel lengths ranging from 1.0 mm to 4.0 mm laterally. Additionally, a noise image was computed, where each pixel corresponds to the standard deviation of the residuals for each regression kernel:

$$\sigma_i = \sqrt{\frac{1}{N}\sum_{k \in K_i}\left(T_k - \frac{x_k}{S_i}\right)^2}, \tag{6.11}$$

where N is the number of points used in the regression.

Using the least squares linear regression shear wave speed image and the noise image, the constrained nonlinear optimization of equation 6.10 was performed using the *fmincon* function in MATLAB (The MathWorks Inc., Natick, MA), where the image data were used as the initial guess and the values of σ_i in equation 6.10

correspond to the values computed using equation 6.11. In this work, constrained optimization was chosen to limit the possible range of shear wave speed values to appropriate estimates (i.e., negative speeds were not permitted and a maximum speed of 8 m/s was considered).

Each pixel in the neighborhood region of the prior was given equal weighting (i.e., $a_{ij} = 1$ in equation 6.10). By choosing the exponential prior distribution, the analytic gradient vector and Hessian matrix were computed, allowing for more rapid optimization using fmincon. The neighborhood region was selected as a circular region around the pixel, with the radius varying from 1.0 mm to 4.0 mm in size. Additionally, the width of the prior distribution was varied such that γ ranged from 10^{-4} to 10^{3} m/s. In total, 7 regression kernel sizes, 7 neighborhood sizes, and 25 values of γ were analyzed for each speckle realization.

6.4.4 Image Analysis

For each of the least squares linear regression and MAP estimated shear wave speed images, the root mean squared (RMS) error was computed. Since the exact size, stiffness, and position of the lesion are known from the FEM simulation, the true shear wave speed was subtracted from the estimated SWS image and the RMS error for the image was computed as the mean RMS error over a region twice the area of the lesion.

To analyze lesion conspicuity, both the contrast and the contrast to noise ratio (CNR) of the lesions were computed using a region half the area of the simulated lesions. The contrast was computed as S_{in}/S_{out}, where S_{in} is the mean shear wave speed inside the target and S_{out} is the mean shear wave speed outside the target. The contrast to noise ratio (CNR), which is generally considered a better metric for lesion conspicuity, was computed in the same region of interest as $(S_{in} - S_{out})/\sigma_{out}$ where σ_{out} is the standard deviation of the shear wave speed outside the target.

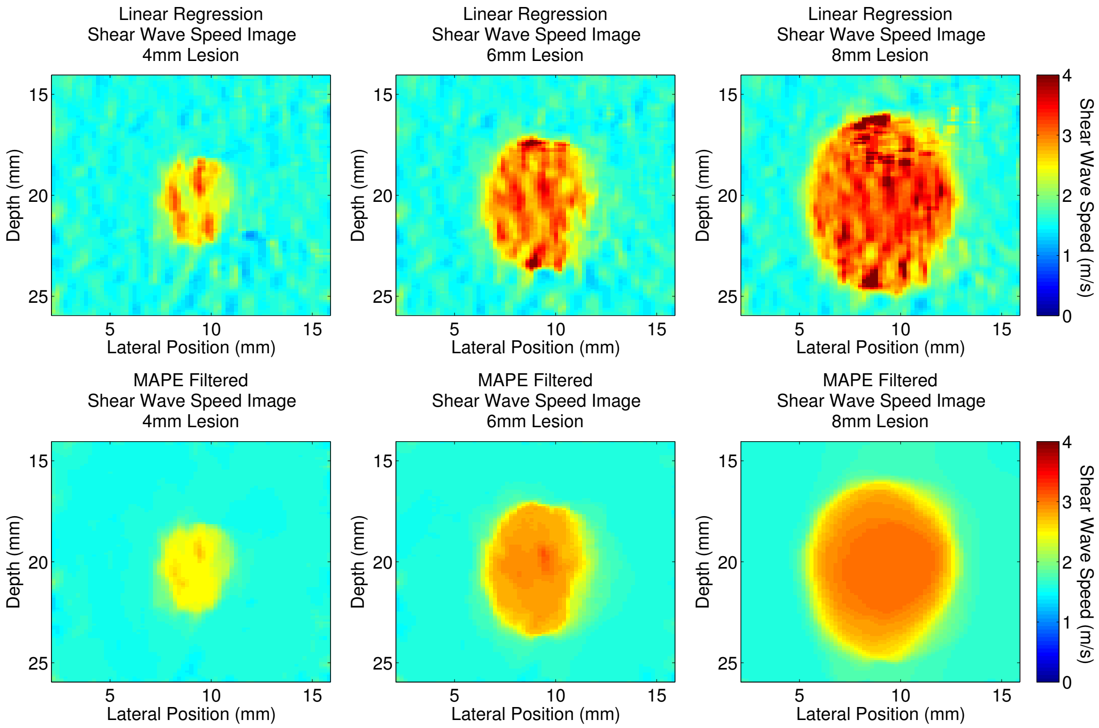

FIGURE 6.4: Example linear regression and MAPE filtered shear wave speed images of the 28.8 kPa Young's modulus inclusions are shown using a 1.5 mm linear regression kernel. By using a small regression kernel, there is significant image noise in the top row of images. The second row of images depicts shear wave speed images after applying the MAPE filter, which results in images that visually appear smoother both in the background and within the lesion.

Analyses are performed with comparisons between the linear regression results, with and without applying a two-dimensional median filter, and the adaptive filter, with error bars computed over the 10 speckle realizations used for each simulation.

6.5 Results

For each size and stiffness combination, shear wave speed images were generated and examples of the variations of the images with size and stiffness are given in figures 6.4 and 6.5, respectively. In both of these figures, a 1.5 mm linear regression kernel was used and the top row of images depicts the result for least squares linear regression on the cumulative wave arrival time data shown in figure 6.3. Utilizing the linear

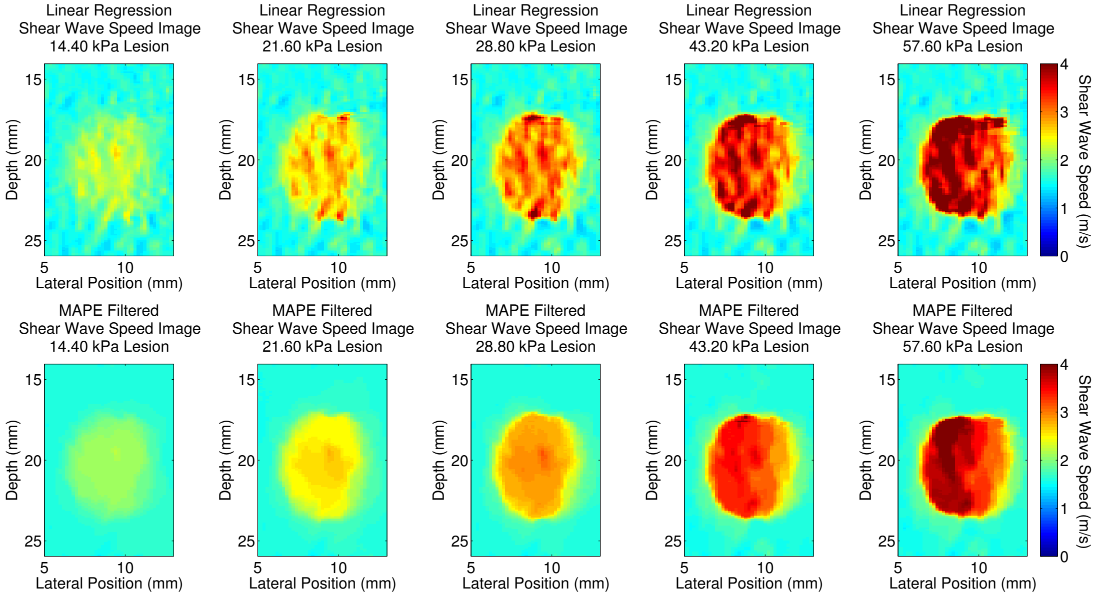

FIGURE 6.5: Example linear regression and MAPE filtered shear wave speed images of 6 mm diameter inclusions for a range of stiffnesses are shown using a 1.5 mm linear regression kernel. The different columns correspond to the different lesion stiffnesses, with Young's moduli ranging from 14.4 kPa (2x stiffer than the background) to 57.6 kPa (8x stiffer than the background). Similar to figure 6.4, the top row shows the least squares linear regression shear wave images and the bottom row depicts the MAPE filtered images. Again, the MAPE filtered images are much smoother both inside and outside the lesion, without significantly blurring the boundaries of the lesion.

regression images as the initial guess and the estimate for σ_i given by equation 6.11, the nonlinear constrained optimization of equation 6.10 was performed and resulted in the bottom row of images, the MAPE filtered images.

To analyze the impact of the MAPE filter on the shear wave speed images, the RMS shear wave speed error was computed, given in units of m/s. This error was computed as a function of regression kernel and neighborhood size (from equation 6.9) in figures 6.6 and 6.7 for the 6 mm, 28.8 kPa Young's modulus lesion. Since the regression kernel length is fixed in figure 6.6, the computed error of the least squares linear regression image is given as the dashed line, which is a fixed value as a function of γ, the width of the exponential prior distribution. However, depending on

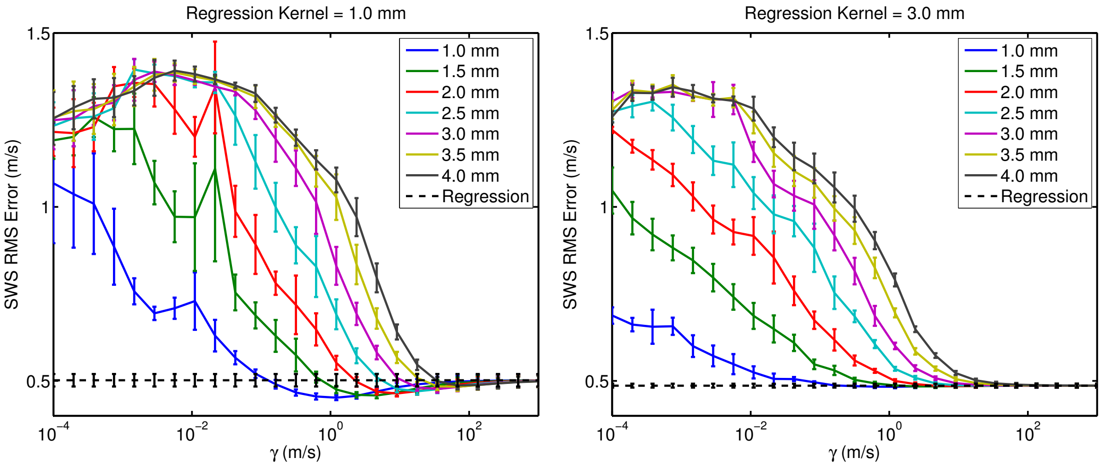

FIGURE 6.6: The shear wave speed error in the 6 mm, 28.8 kPa simulation is given as a function of γ, the width of the exponential prior distribution, and the size of the neighborhood for a 1.0 mm regression kernel (left) and a 3.0 mm regression kernel (right). The error bars indicate the standard deviation over the ten speckle realizations used for the ultrasonic tracking. Depending on the neighborhood size and the value of γ, the overall error in the image could be greater or less than the nominal error from the linear regression estimate. If γ is very small, the MAPE filter results in a uniform image with a single value; however, if γ is very large, the MAPE filtered images reduce to the original least squares linear regression images, resulting in them having the same value for the SWS error.

the neighborhood size and the value of γ, the overall error in the image could be greater or less than the nominal error from the linear regression estimate. Comparing the individual plots of figure 6.7, the optimal value of γ is most dependent on the neighborhood size, not the regression kernel size.

By taking the minimum error as a function of γ for each set of linear regression kernel, neighborhood size, and lesion size, the data in figure 6.8 is obtained. The error bars indicate the standard deviation of the shear wave speed error over the 10 speckle realizations that were simulated. Overall, for the 4 mm lesion (figure 6.8, left plot), there is little difference between the error achieved when using the MAPE filtered images as compared to the linear regression images; however, for the larger lesions, significant error reductions were achieved, such as the 25% shown for the 28.8 kPa lesion and over 40% for the 43.2 kPa and 57.6 kPa lesions (not shown).

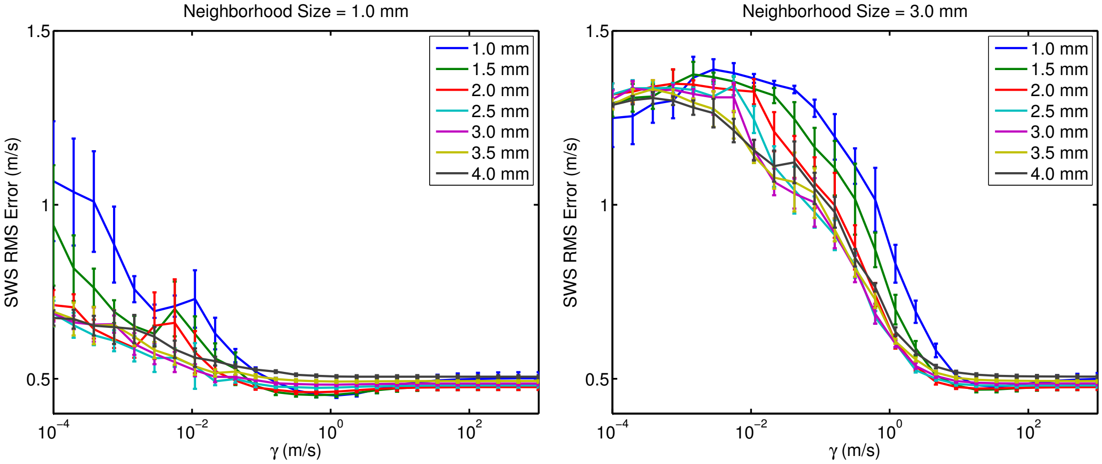

FIGURE 6.7: The shear wave speed error for the 6 mm, 28.8 kPa simulation is given as a function of γ, the width of the exponential prior distribution, and the regression kernel size for fixed neighborhood sizes of 1.0 mm (left) and a 3.0 mm (right). The error bars indicate the standard deviation over the ten speckle realizations used for the ultrasonic tracking. As seen in the comparison of the neighborhood sizes, the optimal value of γ is relatively independent of the regression kernel size, but depends greatly on the neighborhood size.

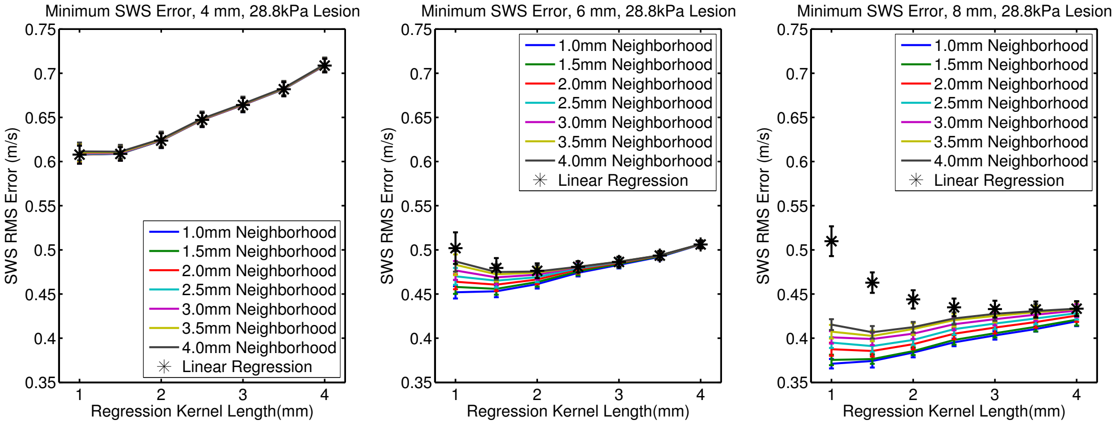

FIGURE 6.8: Shear wave speed error as a function of regression kernel length and neighborhood size is evaluated using the optimal value of γ for the 4 mm (left), 6 mm (center) and 8 mm (right) lesions. The error bars indicate the standard deviation over the ten speckle realizations used for the ultrasonic tracking. For the 4 mm, 28.8 kPa lesion (left), there was little difference in the SWS error between the linear regression and MAPE filtered images, however as the lesion size increases, the error significantly decreases, as much as 25% for the 8 mm lesion with a 1 mm regression kernel.

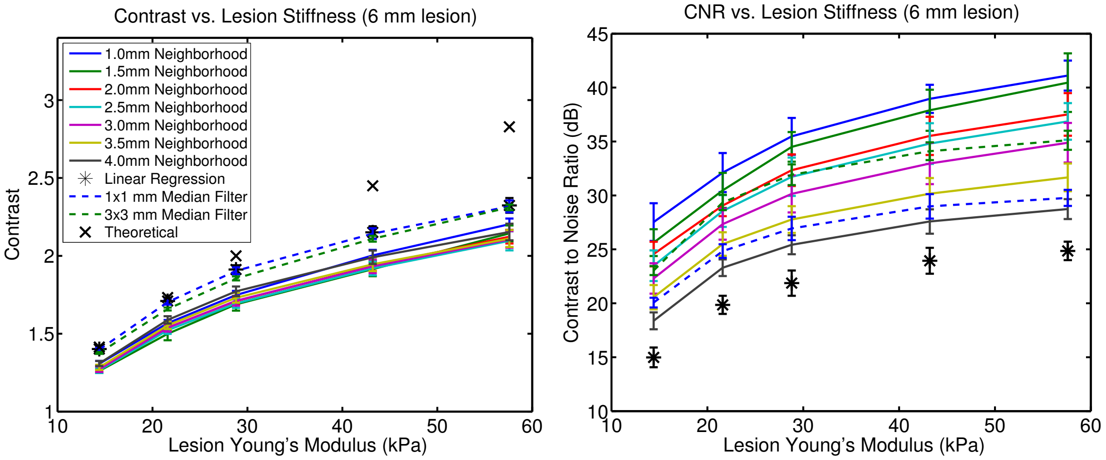

Figure 6.9: Contrast (left) and CNR (right) values are given, with the standard deviation for each, as a function of the lesion stiffness and neighborhood size for the 6 mm diameter lesion using the 1 mm linear regression kernel. The plot of the contrast (left figure) also includes the theoretical image contrast computed as S_{in}/S_{out}, where S_{in} is the shear wave speed inside the lesion and S_{out} is the shear wave speed outside of the lesion used in the FEM simulation. In all cases, the image contrast is less than the theoretical, as expected when using linear regression since there are multiple pixels included in the contrast computation whose regression kernel spans both the background material and lesion. Additionally, for all adaptive filter cases, the contrast is less than linear regression since the MAPE introduces additional bias into the shear wave speed estimate. However, for the CNR, the use of the adaptive filter increases the CNR in every case, by as much as 16 dB.

Although the computation of the total error in the shear wave speed image gives an indication of the accuracy of the shear wave speed image as compared to the true shear velocity, it does not indicate lesion conspicuity. For this purpose, the contrast and CNR were computed and are given in figure 6.9 for the 6 mm diameter lesion using the 1 mm linear regression kernel. In these plots, a single value of γ was chosen for each the neighborhood size, as the results from figure 6.7 indicated that was the most impactful parameter in choosing γ. Additionally, the contrast and CNR results were also compared to using a 2D median filter on the linear regression images. As expected, figure 6.9 demonstrates that the use of the MAPE filter reduces the image contrast, which is due to the filter increasing bias, but it also significantly increases the CNR, by as much as 16 dB, since the filter is designed to reduce the noise.

6.6 Discussion

As the popularity and utility of shear wave elasticity imaging has increased, so has the complexity of the targets it is being used to image. When imaging these more complex targets, smaller regression kernels are required to achieve the desired resolution, however the increased noise confounds image interpretation. In this work, we explored a formulation of a maximum *a posteriori* estimator to use as an adaptive filter for shear wave speed images, which yielded a reduction in the error as well as an increase in the CNR of the targets.

Demonstrated in figures 6.4 and 6.5, the MAPE filter is able to utilize the linear regression estimates and an estimate for the noise in the image in order to improve the overall image quality, independent of size or stiffness of the target being imaged. Because the MAPE filter uses independent noise estimates at each pixel, it retains high quality shear wave speed estimates, while filtering low quality estimates based upon surrounding data. Additionally, by utilizing the exponential prior distribution, the adaptive filter is able to retain sharp edges, as has been shown previously [14, 15].

The denoising effects of the MAPE filter are present in all of the examples given in figure 6.4 and 6.5; however, those images were generated using the optimal value for the width of the exponential distribution (γ) for a given regression kernel and neighborhood size. As detailed in figures 6.6, 6.7 and 6.8, the error resulting from the use of the MAPE filter is dependent on all of these parameters. Specifically, for figures 6.6 and 6.7, the interpretation as a function of γ can be based in two main groups. If γ is very small, the exponential prior distribution dominates equation 6.10 and essentially forces the entire image to have a single value, which has a high RMS error. Alternatively, if γ is very large, the exponential prior term is very small in equation 6.10, and the MAPE filtered images are essentially no different than the original least squares linear regression images, which results in them having the same value for the SWS error.

Interpreting the figures individually, figure 6.6 details the performance of the adaptive filter for a fixed regression kernel as a function of both the neighborhood size and the width of the prior distribution. For the small regression kernel (figure 6.6, left), the adaptive filter can reduce the overall shear wave speed error below the linear regression estimate, depending on the value of γ; however, for the larger regression kernel (figure 6.6, right), the minimum error is given by the linear regression estimate. The performance of the adaptive filter is therefore highly dependent on the amount of noise originally present in the data (i.e., a large regression kernel has low noise, therefore the filter does not improve image quality, whereas the small regression kernel has high noise, and thus the adaptive filter significantly improves the shear wave speed image).

Although the overall performance of the filter depends heavily on the regression kernel size, figure 6.7 demonstrates that the optimal value of γ is most highly dependent on the neighborhood size, which is expected since it scales the summation of the prior distribution. Additionally, figure 6.7 portrays the range of values of γ for which the MAPE filter improves image quality, which is most evident in the 1 mm regression kernel size. Since the error at the maximum value of γ corresponds to the linear regression estimate, all values of γ for which the error is less than the error at the maximum value of γ correspond to improvements in image quality. As demonstrated using both the 1.0 mm (figure 6.7, left) and 3.0 mm (figure 6.7, right) neighborhood sizes, γ can vary by upwards of an order of magnitude and still reduce the overall error in the shear wave speed images. This large range of useful values of γ demonstrates that this adaptive filter is stable and flexible for a wide variety of imaging scenarios.

However, to determine the peak performance of the adaptive filter, the width of the prior distribution was optimized in figure 6.8, which depicts the maximum possible reduction in the error achievable as a function of regression kernel, neighborhood size, and target size for a fixed target stiffness. Figure 6.8 shows quite a bit of variability with all of the parameters, however, in general, the minimum error is achieved with the smallest regression kernel and the smallest neighborhood size. This trend is also consistent across the different stiffnesses simulated, and is an expected result. Theoretically, by using the smallest possible regression kernels, the image bias is reduced because there are fewer pixels that span both the background and lesion material, but this typically results in higher amounts of noise or variance. The adaptive filter then provides denoising, allowing for the use of the smallest regression kernels without as much variance.

The quoted shear wave speed error takes into account both the bias and variance, and is therefore a fair estimate of the error in the image, but it does not take into account lesion conspicuity. Additionally, although error reductions were shown by obtaining the minimum error across all values of γ in figure 6.8, this is not a practical image processing scenario as it requires significant computing power to generate each image (10-30 seconds) depending on the nonlinear optimization algorithm.

Thus, to demonstrate the stability of the adaptive filter and its applicability to a more realistic imaging scenario, the contrast (figure 6.9, left) and CNR (figure 6.9, right) were computed for the 6 mm diameter lesion using the 1 mm linear regression kernel. In these plots, a single value of γ was chosen based only on the neighborhood size, as indicated by the results in figure 6.7. As expected, figure 6.9 demonstrates that the use of the adaptive filter reduces the image contrast, which is due to the filter increasing bias, but it also significantly increases the CNR, by as much as 16 dB, since the filter is designed to reduce the variance. Additionally, the adaptive filter had higher CNR as compared to applying an equivalently sized 2D median filter, which is expected since the adaptive filter accounts for spatially varying noise profiles.

Through the development of the adaptive filter, multiple choices were made to demonstrate the utility, but also limited the scope of this analysis. The use of the exponential prior, which is a specific choice of a generalized Gaussian prior distribution [14], allowed for more rapid computation of the final estimate because analytic functions for the gradient and the Hessian matrix could be computed. However, even with these functions, to perform the optimization requires significant computation power, typically taking 10-30 seconds for a single set of parameters with a 8000 pixel image. Additionally, this study was limited to one implementation of an adaptive filter, and investigation of other prior distributions as well as other optimization algorithms is warranted.

6.7 Conclusions

We have demonstrated that the MAPE adaptive filter can improve image quality by reducing the overall error in SWEI images as well as increasing the CNR, although the contrast in the images is slightly reduced. Challenges have also been identified with regards to implementation and computation time compared to least squares linear regression SWEI images. Additionally, by using a biased estimator such as the proposed MAPE filter, the ability to derive information from the quantitative values can be compromised since the estimator introduces a bias in the shear wave speed values. All of these benefits and challenges must be balanced; however, the current implementation of this adaptive filter was shown to be stable as the width of the prior varied over an order of magnitude and demonstrated increases in CNR by upwards of 16 dB, yielding promising results for the stability and flexibility of adaptive filters to improve shear wave images.

7

In Vivo 3D Prostate ARFI and SWEI Imaging

The following chapter describes the use of the tools, sequencing optimizations, and data processing algorithms developed in the previous chapters to acquire and evaluate volumetric *in vivo* ARFI and SWEI data sets.

7.1 Introduction

Acoustic radiation force impulse (ARFI) imaging and shear wave elasticity imaging (SWEI) are well established ultrasonic elasticity imaging modalities that have been used to image structures and pathologies in many organs including the breast, prostate, and liver [121, 7, 100, 105, 81, 68]. In the prostate, the primary imaging target is cancer which has been reported as stiffer than the surrounding tissue [25, 120]. However, other pathologies such as benign prostatic hyperplasia (BPH) and atrophy have been reported as confounding effects for detecting cancerous regions [120].

Both ARFI and SWEI imaging employ similar acoustic radiation force push excitations, but differ in the processing of the resulting displacement field. ARFI images provide qualitative information from the dynamic response of the tissue within the region of excitation of the pushing beam. SWEI images provide quantitative information by reconstructing the shear wave speed of the tissue in a region spatially offset from the region of excitation. The interpretation of ARFI images can be confounded by the focal geometry of the pushing beam and differences in the local attenuation of the tissue [71]; SWEI image interpretation can be confounded by reconstruction artifacts in heterogeneous media associated with reflected waves, which can be reduced with directional filters [95, 30]. Previous work in phantoms and simulation has demonstrated that ARFI and SWEI images differ in their resolution and contrast [95].

The prostate has a complex structure including three primary zones: peripheral, transition, and central, as well as ejaculatory ducts and urethra traversing the organ, and an anterior fibro-muscular stroma (figure 7.8, bottom left). Due to the structure within the prostate, for SWEI imaging, to accurately approximate the tissue as homogeneous and isotropic, small reconstruction kernels must be used, which lead to increased noise within the image. Additionally, the structure and pathology within the prostate cause multiple reflections of the shear waves, resulting in image artifacts. Thus, the adaptive filter presented in chapter 6 is used to obtain high quality SWEI images in this chapter.

In this work, a three-dimensional *in vivo* prostatic imaging system capable of concurrently acquiring ARFI and SWEI data was developed to determine their capability to visualize prostate cancer.

7.2 Methods

7.2.1 ARFI and SWEI Sequence Design

A modified Siemens Acuson SC2000™ ultrasound scanner (Siemens Healthcare, Ultrasound Business Unit, Mountain View, CA, USA) and the longitudinal array of an Acuson ER7B bi-plane endorectal transducer were used for this work. The sequences were designed and tested using the tools described in chapter 3.

Acquisitions were performed in a phantom with the ER7B while varying both the focal depth and frequency to determine the optimal radiation force excitation. After analysis, a push frequency of 4.6 MHz was chosen to give good depth penetration of the push, but still be within the bandwidth of the transducer; additionally, it was determined that the ER7B could not provide sufficient radiation force deeper than 30 mm. The push focal depths were then chosen within these constraints to provide high data quality throughout the prostate, which is nominally located 7-10 mm from the rectal wall and extends 20-40 mm anteriorly. The method detailed in chapter 5 was used with focal depths at 15 mm, 22.5 mm, and 30 mm with an F/2 focal configuration for each depth.

Hydrophone measurements were then made on this sequence to report the mechanical index (MI) of these acquisitions (figure 7.4). During the analysis of the hydrophone measurements, it was determined that the 15 mm focal depth had a MI over the FDA limit of 1.9. Therefore, the sequence was modified to use a 5.4 MHz push at 15 mm with a F/2.35 focal configuration to maintain the same beamwidth (0.67 mm) as the F/2 4.6 MHz pushes. This change reduced the MI to below 1.9 because it was higher frequency and less tightly focused. The other focal depths were not modified.

After determining the radiation force excitation, the tracking configuration was programmed with the goal being to acquire both ARFI and SWEI data concurrently. Sixteen parallel receive lines were chosen to observe both the on- and off-axis response of the tissue to the pushing pulses and are shown in figure 7.1. Four lines were dedicated to tracking the on-axis displacement, with all 4 beams located inside the beamwidth of the pushing pulses such that the beam spacing was 0.17 mm. The other twelve lines were separated into two groups to observe both the left and right propagating waves. For each sub-group of 6, the beams were located 1.89 mm laterally offset from the push and had an inter-beam spacing of 0.76 mm (each track line is an independent sample since 0.76 mm is greater than the beamwidth), covering 3.8 mm field of view. Due to bandwidth constraints when using the 16 parallel receive lines, the center frequency of the track lines was set 5.0 MHz. Additionally, the per-beam sampling of the IQ data for these acquisitions was chosen to be 4 MHz to accommodate the hardware buffer sizes on the Siemens Acuson SC2000™.

The sequence was also specified temporally to have an 125μs pulse repetition interval (PRI), corresponding to an 8 kHz PRF, and 40 tracks were acquired corresponding to 5 ms after force cessation. The PRI was chosen as the minimum time between transmits required by the front-end of the SC2000™ based on acquiring 35 mm of data. Additionally, 5 ms was chosen as the total tracking duration due to hardware buffer size limitations while acquiring the data.

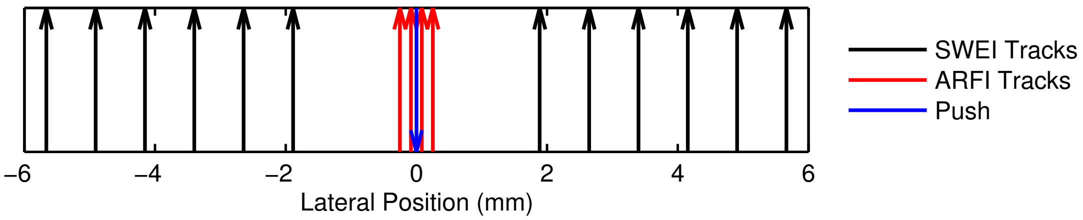

FIGURE 7.1: Diagram depicting the lateral locations of the ARFI and SWEI track beams relative to the push beam for the combined ARFI/SWEI acquisitions. The center four lines are dedicated to tracking the on-axis displacement for ARFI images, with an inter-beam spacing of 0.17 mm. Two sub-groups of 6 beams are used to generate the SWEI images and are located 1.89 mm laterally offset from the push and have an inter-beam spacing of 0.76 mm covering a 3.8 mm field of view.

7.2.2 Automated 3D ARFI, SWEI and B-Mode Volume Acquisition

A CIVCO™(CIVCO Medical Solutions, Coralville, Iowa) transperineal prostate transducer holder was modified for use during these studies. A custom mold of the ER7B was cast to mate with the CIVCO holder, and a stepper motor was added to allow the transducer to rotate along its elevation dimension to obtain multiple 2D planes. Additionally, an optical encoder was attached to the rotation stage to provide real-

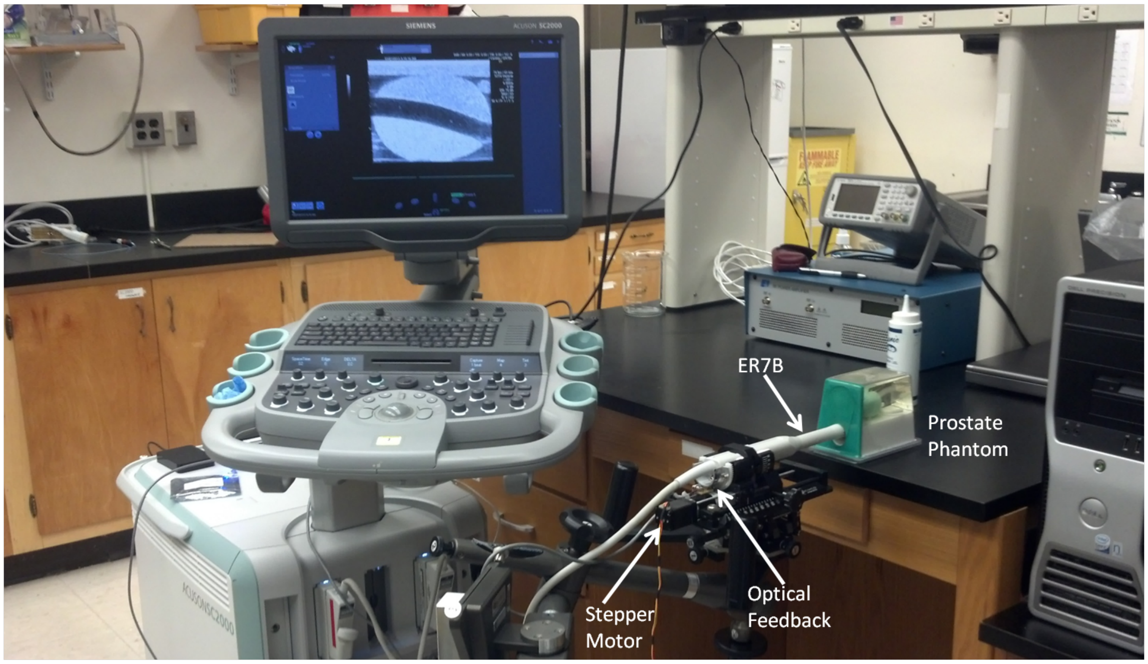

Figure 7.2: Picture of the acquisition setup with the Siemens Acuson SC2000™, ER7B, rotation stage, and optical feedback encoder.

time feedback of the current position of the transducer. All of these components are shown in the typical volumetric acquisition pictured in figure 7.2, which is controlled by Python code written to interface between the ultrasound scanner, stepper motor, and optical encoder.

The optical feedback mechanism is comprised of three components, a reflective strip, an optical encoder with circuit board, and a quadrature to USB adapter. The reflective strip is attached to the holder that rotates and contains 212 lines per inch. The relative position of the holder can then be measured by using the optical encoder, an Avago AEDR-8300-1W2 (Avago Technologies, San Jose, CA), which is mounted below the reflective strip. The encoder uses a custom circuit board to send the data to a US Digital QSB-S (US Digital, Vancouver, WA) quadrature to USB adapter. The software examples provided for reading the data from the QSB-S were given in both C# (C-Sharp) and LabVIEW (National Instruments, Austin, TX).

To interface the QSB-S with the Python code, the C# examples were modified to use Windows Shared Memory, which creates a virtual file in RAM that is able to be read and written by multiple separate programs, and compiled in Visual Studio (Microsoft Corporation, Redmond, WA). The Python driver script opens the shared memory space, then launches the separate, compiled C# program, and as necessary, the Python code writes a value to the shared memory space, indicating that the C# code should provide the current position of the transducer, which is then written back to the same shared memory space. The current position is provided as an integer, which is converted to the absolute position in degrees using the calibration of 4240 steps per full rotation (360°).

An Anaheim Automation 11YPG202S-LW4-R27 stepper motor (Anaheim Automation, Anaheim, CA) was used to drive the rotation of the transducer holder using a custom circuit board and attached via a USB serial interface to the ultrasound scanner. The Python code uses the PySerial package to interface with the motor through a series of basic commands: rotate to an absolute position, rotate a relative amount, wait for motor to stop, reset current position to zero, and read current motor position.

The primary Python driver script interfaces between these individual components to correctly acquire the volumetric data and is run on the Siemens Acuson SC2000™. The initialization phase of the code reads in the requested number of frames, sets up the Windows Shared Memory, resets the current position of the stepper motor to zero, and loads the imaging case and ARFI/SWEI parameters on the Siemens Acuson SC2000™. Once everything is prepared, a separate, compiled C program is launched, and the acquisition of the ARFI/SWEI data begins. For each frame that is acquired, the external program reads in the data, processes and displays a B-mode image on the screen to provide continuous visual feedback during the acquisition. After rotating through the entire volume, the external program closes, a high quality

B-mode imaging case is loaded onto the Siemens Acuson SC2000™. The transducer then rotates back through the volume saving the high quality B-mode data. For each frame of data acquired, the current angular position of the transducer is also saved in order to correctly reconstruct the volumetric data.

7.2.3 B-Mode Imaging Processing

During the volumetric acquisition, each high quality B-mode frame is saved separately and has 3 files associated with it: a beamformed IQ data file, a text file describing the binary data file, and a parameters file associated with the imaging sequence. The high quality B-mode data are read from the binary files as IQ data, then envelope detection and log-compression are performed before compiling the data into a single 3D matrix. A 0.25 mm×0.5 mm×0.5 mm (axial×lateral×elevation) median filter is then applied. Finally a time-gain compensation (TGC) curve is computed based on the mean B-mode brightness across the entire data set as a function of depth and applied to the volume of data.

7.2.4 ARFI Imaging Processing

Separate data and parameters files are saved for the radiation force image data, and after reading them into MATLAB, the data was separated into the on- and off-axis components. Displacement estimation was then performed for the on-axis data using a phase shift estimator to compare the pre-push reference to the post-push tracks [58, 89].

Once the displacements are estimated, multiple processing steps are applied to the data before generating ARFI images. The push data is removed along with the first time step after the push since these data are corrupted due to acoustic noise from the long duration pushing pulses. A 0.75 mm axial median filter is applied to the data, then the displacement between the references and the tracks is interpolated using cubic splines to provide uniform temporal sampling. A 20 - 1000 Hz fourth order Butterworth bandpass filter is applied using the *filtfilt* function in MATLAB, which provides zero-phase forward and reverse digital IIR filtering.

The data are then split into individual time steps and each temporal sample is compiled in 3D, a 0.25 mm×0.5 mm×0.5 mm (axial×lateral×elevation) median filter is applied, and they are normalized as a function of depth to account for attenuation and focal gain effects. The normalization profile was determined from phantom data sets by averaging data from both an $\alpha = 0.5$ db/cm/MHz and an $\alpha = 0.7$ db/cm/MHz phantom to approximate the attenuation as $\alpha = 0.6$ db/cm/MHz. The profile was low pass filtered with a cutoff of 0.19 mm^{-1} (corresponding to 16λ, where λ is the acoustic wavelength), then scaled to a [0 1] range, and all values below 0.2 were set to 0.2 to avoid amplifying noise. This normalization profile was then applied to each ARFI line before combining the data in a 3D matrix (axial×lateral×elevation angle).

7.2.5 SWEI Imaging Processing

The same data and parameters files used for the ARFI images are loaded again, except the off-axis data are now processed to generate the SWEI images. The previously described displacement estimation is performed and the data are split into the left and right propagating waves, with each frame of data now arranged in a 4D matrix (axial×parallel receive beams×push beam number×time).

All data prior to the first uncorrupted track line is removed and the axial depth is limited to 8-35 mm to remove data outside of the depth of field of the radiation force excitation since the shear wave propagation assumptions are not valid. A 20 - 1000 Hz fourth order Butterworth bandpass filter is then applied, again using the *filtfilt* function in MATLAB to achieve zero-phase forward and reverse digital IIR filtering.

The time-to-peak (TTP) displacement is extracted and taken as the wave arrival time [81]. If the maximum displacement occurs at the first time step, the data is differentiated to compute the curvature of the displacement through time curve to determine if the leading edge of the shear wave was missed, and therefore, only the recovery of the tissue was acquired. If so, the data point is rejected and no arrival time is used for that pixel (i.e., it is set to not a number, NaN). The valid wave arrival times for each frame are then combined into a 3D matrix (axial×parallel receive beams×push beam number) and a 0.75 mm axial median filter is applied along with a 3-pixel push beam median filter (i.e., across the third dimension of the matrix). Other methods were also considered to determine the wave arrival time such as time-to-peak velocity and cross-correlation of displacement or velocity profiles [21, 95]; however, it was determined that TTP displacement resulted in the most robust arrival time estimator for these data (figure 7.13)

After determining the wave arrival time, the data are compiled into a single 4D matrix (axial×parallel receive beams×push beam number×frame number) and a 1.2 mm axial median filter is applied along with a 5-pixel median filter between the frames (i.e., the fourth dimension of the matrix). To estimate the shear wave speed at every spatial location, it is necessary to combine the data from different push beams in the same frame (i.e., collapse the second and third dimensions of the matrix). However, because the push and track locations were translated across the field of view, no common starting point for the time of flight estimation exists, and therefore, the wave propagation time between pushing locations must be estimated to align the data as if it were all originating from a single pushing location.

After translating the push beam, the wave arrival times for the second push are offset by the time it takes for a shear wave to propagate between the push locations. Therefore, the time difference between each of the five overlapping track locations is computed and averaged together to estimate the propagation time between the push

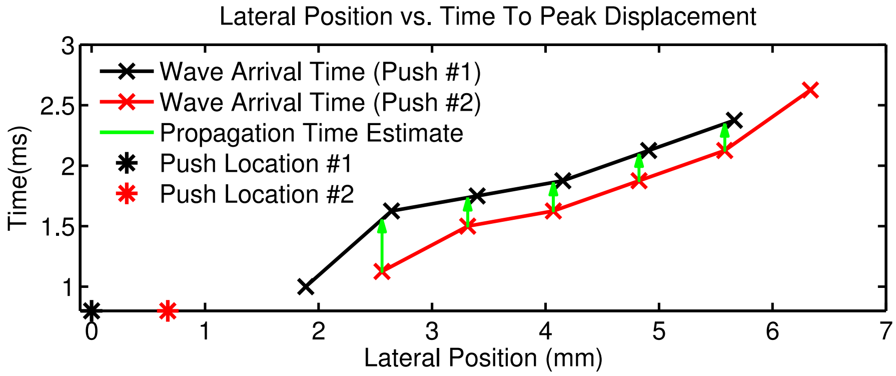

FIGURE 7.3: Estimation of the propagation time between the two push locations. After the five estimates are computed, they are averaged together to determine the shear wave propagation time between the push locations.

locations. This method is described in figure 7.3, where the black and red lines are the wave arrival times from the push locations indicated by the black and red $*$'s. The green arrows indicate the computed time difference at each track location. The values indicated by the green arrows are then averaged together and added to the red line to align the wave arrival time data as if it were all originating from the first push location.

During the wave arrival time alignment processing, the algorithm rejects data where a negative propagation time estimate was computed. This data rejection would occur, for example in figure 7.3, if some of the points on the black curve were below the red curve, they would be discarded as poor estimates. This arrival time alignment is performed for all of the pushes across the field of view at each depth independently and is used to increase the effective lateral sampling of the shear wave.

The wave arrival time data from the left and right waves were processed individually. The wave arrival times are then split into small (2.0 mm), overlapping lateral kernels to estimate the local shear wave speed and generate SWEI images using both linear regression and the maximum *a posteriori* estimator. The shear wave speed estimates from the individual left and right waves were then combined using two methods: computing the mean value or using the maximum value. Finally, the data from each frame is combined into a 3D matrix (axial×lateral×elevation angle).

An alternative approach to the data processing would be to estimate the shear wave speed for each push individually. The estimated shear wave speeds could then be averaged together, however the individual estimates would be very noisy as each estimate would result from fitting a line to 3 data points (2 mm). Additionally, if any of the data had been rejected earlier, the potential noise on the estimate would further increase. Thus, the arrival time alignment process improves the robustness through additional data rejection as well as avoids potential gaps in the data.

7.2.6 Scan Conversion and 3D Visualization

For each of the data sets compiled in 3D (i.e., B-mode, ARFI, and SWEI), to generate images with the correct dimensions, the data must be scan converted to have Cartesian grid spacing in all dimensions. Based on the axis of rotation and the distance from that axis to the face of the transducer, the precise polar grid coordinates in the axial-elevation planes can be computed. The *TriScatteredInterp* function is then used in MATLAB to interpolate the data to a Cartesian grid.

Once scan converted, the data are saved from MATLAB in a RAW image format that can be read by ImageJ (National Institutes of Health, Bethesda, MD). The data are then converted to the NIfTI-1 format and zipped to have smaller files allowing for more rapid loading of the images. Both ImageJ and Slicer3D [37] were then utilized to visualize the volumetric data.

7.2.7 In Vivo *Acquisitions*

Patients expecting radical robotic prostatectomy were consented for this study in Duke Medical Center under IRB approval. To date, 44 patients have been imaged using the previously detailed methodology over the past two years as part of an ongoing study. At the initiation of the study, only ARFI images were evaluated, as the SWEI processing has been developed while accruing the patient population.

During the study, all data were collected prior to the surgery after the patients had been anesthetized. Whole mount histology was performed on the excised organ to obtain 3D volumes of the pathology of the prostate by fixing the organ in formalin and slicing it into 3 mm thick sections, which were then read by a pathologist to determine the location of cancerous regions. The volumetric pathology data were then compared to the ultrasound volumes.

7.3 Acoustic Output and Thermal Safety Testing

Hydrophone measurements were performed to evaluate the acoustic output of the sequences using a Sonic Technologies Model 804 PVDF membrane hydrophone (Sonic Technologies, Hatboro, PA). For each focal depth, a 10-cycle excitation was transmitted at a low PRF (e.g., 100 Hz) through deionized water and the location of the maximum intensity was determined in free space. The pressure through time at this location was recorded to determine the mechanical index (MI), which is derated computed as the peak negative pressure divided by the square root of the center frequency. After low-pass filtering at 20 MHz (the upper bound of the bandwidth for the hydrophone), the data for all three focal depths are shown in figure 7.4, with the MI computed as 1.64, 1.40, and 1.22 for the 15 mm (5.4 MHz), 22.5 mm (4.6 MHz), and 30 mm (4.6 MHz) focal depths, respectively. All of the measured values are below the FDA threshold for MI.

The *in vivo* volumetric sequences were then evaluated for thermal safety using an Omega HYP1-30-1/2-T-G-60-SMP-M thermocouple and an Omega DAQ-3000 acquisition system (OMEGA Engineering, INC, Stamford, Connecticut). The ER7B was placed on a tissue-mimicking phantom using ultrasound gel to couple the ultrasonic energy into the phantom, and the thermocouple was placed between the

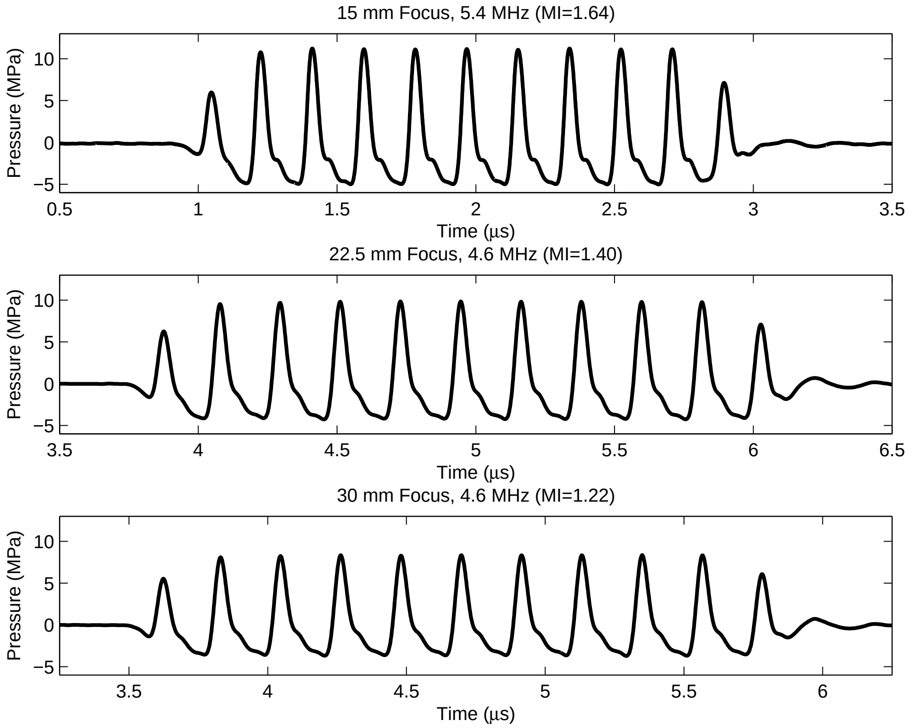
15 mm Focus, 5.4 MHz (MI=1.64)

22.5 mm Focus, 4.6 MHz (MI=1.40)

30 mm Focus, 4.6 MHz (MI=1.22)

FIGURE 7.4: Acoustic safety measurements for the *in vivo* acquisitions made with a Sonic Technologies PVDF membrane hydrophone for each of the 3 focal depths used. The pressure was measured after finding the location of maximum intensity in free space, and the mechanical index was computed after derating as 1.64, 1.40, and 1.22 for the 15 mm, 22.5 mm, and 30 mm focal depths, respectively, all of which are below the FDA threshold of 1.9.

transducer and the phantom. The temperature rise was recorded using custom LabVIEW code. The thermocouple was translated across the face of the transducer in order to determine the location of maximum temperature rise, and at that position, a full volumetric sequence (151 frames) was then initiated and the temperature was recorded and is shown in figure 7.5.

The resulting data were low-pass filtered at 2 Hz to remove the high frequency noise associated with the thermocouple and the maximum value was compared to the temperature before starting the sequence, resulting a temperature rise of 3.81°C. Because the transducer was not rotated, as it would be *in vivo*, this temperature rise is an upper bound, and is below the 6°C safety threshold stated in the IRB protocol.

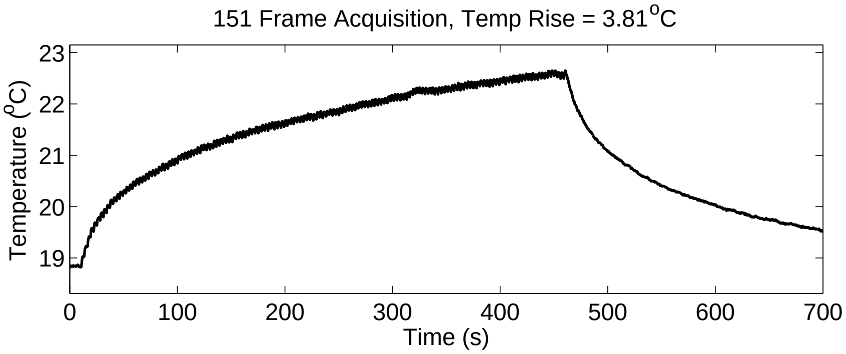

FIGURE 7.5: Thermal safety measurements for the *in vivo* acquisitions, demonstrating a maximum temperature rise of 3.81°C associated with a 151 frame acquisition. The transducer was held in a fixed position during the acquisition, and therefore, the expected *in vivo* temperature rise is less.

7.4 Phantom Results

Acquisitions using the previously designed sequence were performed in a custom CIRS tissue-mimicking phantom (CIRS, Norfolk, VA) to evaluate ARFI and SWEI image quality. Figures 7.6 and 7.7 show the ARFI and SWEI data collected from a single acquisition of a 10.4 mm diameter, 28 kPa cylindrical inclusion in a 8 kPa Young's modulus background.

Figure 7.6 displays ARFI images at two time steps (0.375 ms and 0.75 ms) with a 0.5 x 1.0 mm (axial x lateral) median filter applied. The displacement profiles across the lesion are also plotted after taking the mean value ±0.5mm axially around the lesion center (solid black line). The ARFI displacements are inversely proportional to the shear modulus, therefore they are compared to the analytic lesion profile. This profile was computed as $1/G$, where G is the shear modulus, and then the profile was scaled to match the background displacement value (dashed black line).

Matched SWEI images were generated retrospectively, after developing the processing algorithms detailed in chapter 6 and section 7.2.5, and are shown in figure 7.7. The left column of images are generated after performing linear regression and the

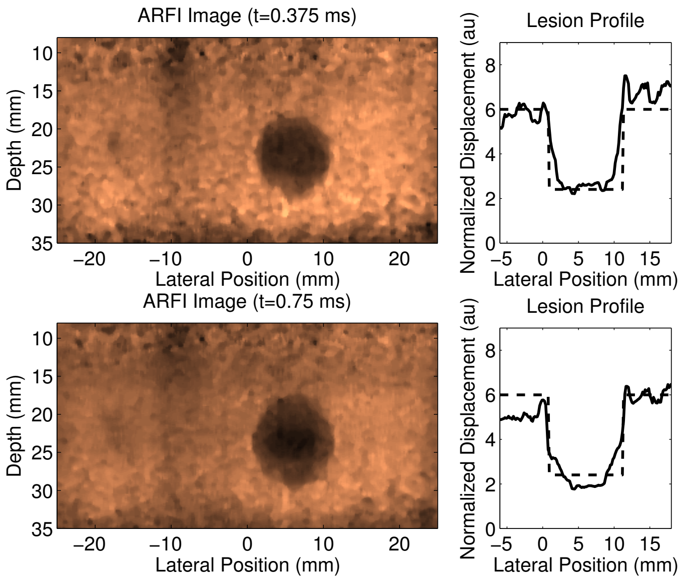

FIGURE 7.6: Normalized ARFI images at two time steps (0.375 ms and 0.75 ms) of a 28 kPa cylindrical target in a 8 kPa Young's modulus background using the *in vivo* radiation force image sequence with a 0.5 x 1.0 mm (axial x lateral) median filter applied. The displacement profiles across the lesion are also plotted after taking the mean value ±0.5mm axially around the lesion center (solid black line). The ARFI displacements are inversely proportional to the shear modulus, and therefore, they are plotted against the analytic lesion profile as computed from $1/G$, which was then scaled to match the background displacement (dashed black line).

right column is generated using the maximum *a posteriori* estimator (MAPE) to filter the shear wave images. The lateral profiles across the lesion are also shown, using the same method as for the ARFI images, where the experimental data were averaged ±0.5mm axially around the lesion center. For the SWEI data, the estimated parameter is shear wave speed, which is analytically computed as $v_s = \sqrt{G/\rho}$, where v_s is the shear wave speed, G is the quoted shear modulus, and ρ is the density (assumed to be 1 g/cm^3).

Figure 7.7 contains four rows of images: the top row corresponds to the left propagating wave, the second row is the right propagating wave, the third row is the result of taking the maximum value of the shear wave speed between the two top rows, and the last row is the mean value between the two top rows. After analyzing the

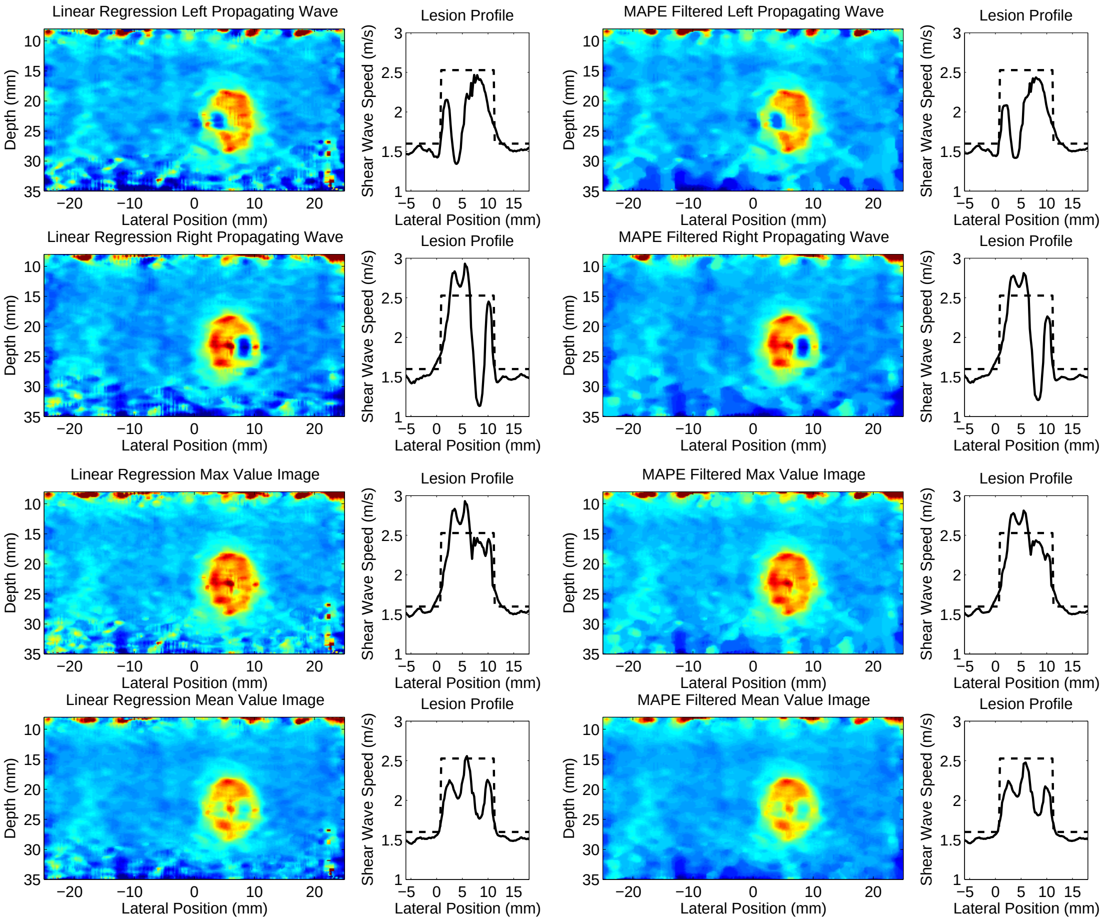

Figure 7.7: Matched SWEI images were generated from the same data set acquired in figure 7.6. The left column of figures is the linear regression SWEI images and profiles across the lesion, averaged ±0.5mm axially around the lesion center and plotted against the quoted shear wave speed of the lesion. The right column of images is the MAPE filtered data. The top row of images corresponds to the left propagating wave, the second row is the right propagating wave, the third row is the result of taking the maximum value of the shear wave speed between the two top rows, and the last row is the mean value between the two top rows. From the top two rows of the image, there are clearly soft-center artifacts present resulting from reflected shear waves; however, by utilizing the maximum value these artifacts are generally removed. Comparing the linear regression to the MAPE filtered images, the two images and profiles are generally similar, except deep to 30 mm, where there is low signal, and correspondingly high noise, the MAPE filtered images appear to reduce the noise, especially in the maximum value image.

top two rows of the figure, it is clear that soft-center artifacts are present, potentially due to reflected shear waves [30].

Given that the soft-center artifacts appear differently in the left and right propagating waves, two methods were investigated to combine the data, corresponding to the bottom two rows of figure 7.7. Since the artifact appears as a soft region, the first method investigated was to take the maximum value between the two individual images (figure 7.7, third row); however, this method also results in additional noise as seen deep to 30 mm in the linear regression image. Thus, the mean value between the left and right wave images was also evaluated in the fourth row of figure 7.7, which reduces the noise, but is not as efficient at removing the soft-center artifacts.

Comparing the linear regression to the MAPE filtered images, the two images and profiles are generally similar, except deep to 30 mm, where there is low signal, and correspondingly high noise; in these regions, the MAPE filtered images appear to reduce the noise. Additionally, given that the noise was the primary issue with the linear regression maximum value image, using the MAPE filtered maximum value image provides a low-noise, high image quality that also removes the soft-center artifacts; therefore, the SWEI images presented herein were generated using this processing.

7.5 Initial 3D *in vivo* Results

Using the previously described methodology, 44 patients have been imaged and the volumetric data has been analyzed after B-mode, ARFI and SWEI image processing and scan conversion. For each patient, the B-mode data is used to inform the reader to the location of the capsule of the prostate as it is most easily visualized in B-mode. A single time step (temporal sample) of the ARFI data was used for analysis and identification of suspicious regions after normalization and scan conversion. The maximum value MAPE filtered SWEI data was compared retrospectively to the

ARFI data to determine concordance of the imaging modalities.

The anatomical features of the prostate including the peripheral zone, central gland (transition and central zones), and urethra are well visualized in ARFI images, as shown in figure 7.8. As described in section 1.3.2, the central gland has been reported as stiffer (darker copper in the ARFI images) than the peripheral zone [122, 120]. Additionally, the ARFI images clearly portray linear structures between the base and apex of the prostate, which are believed to be the urethra and ejaculatory ducts. The matched SWEI images (figure 7.8) also delineate the central gland as stiffer (red/yellow in the SWEI images) than the peripheral zone, although the urethra is not well visualized. The anatomy visualization is consistent in all patients, and the images in figure 7.8 were chosen as an example that portrays typical anatomy.

Three case studies were then chosen after identifying suspicious regions in each of the ARFI image volumes based on 6 criteria assuming the cancer should be stiff (dark in the ARFI images): contrast of a target compared to surrounding tissue, the target cross-sectional area, the margins of the dark region, the texture of the region, the anatomical zone the region appears in, and the number of stiff regions in the prostate. For example, a region that was identified as highly suspicious had high contrast relative to surrounding tissue, had well circumscribed or partially circumscribed margins, appeared with a smooth or speckled texture, was located in peripheral zone, and there were at most 2 other dark regions in the prostate.

For each case, the B-mode, ARFI, and MAPE filtered SWEI images are presented alongside the corresponding pathology slide. For each case, the axial, sagittal, and coronal planes are presented with cross-hairs indicating where they intersect; the pathology slide is presented only in the axial view as that was the plane cut during the whole mount processing.

The three orthogonal planes are oriented such that the base of the prostate (near

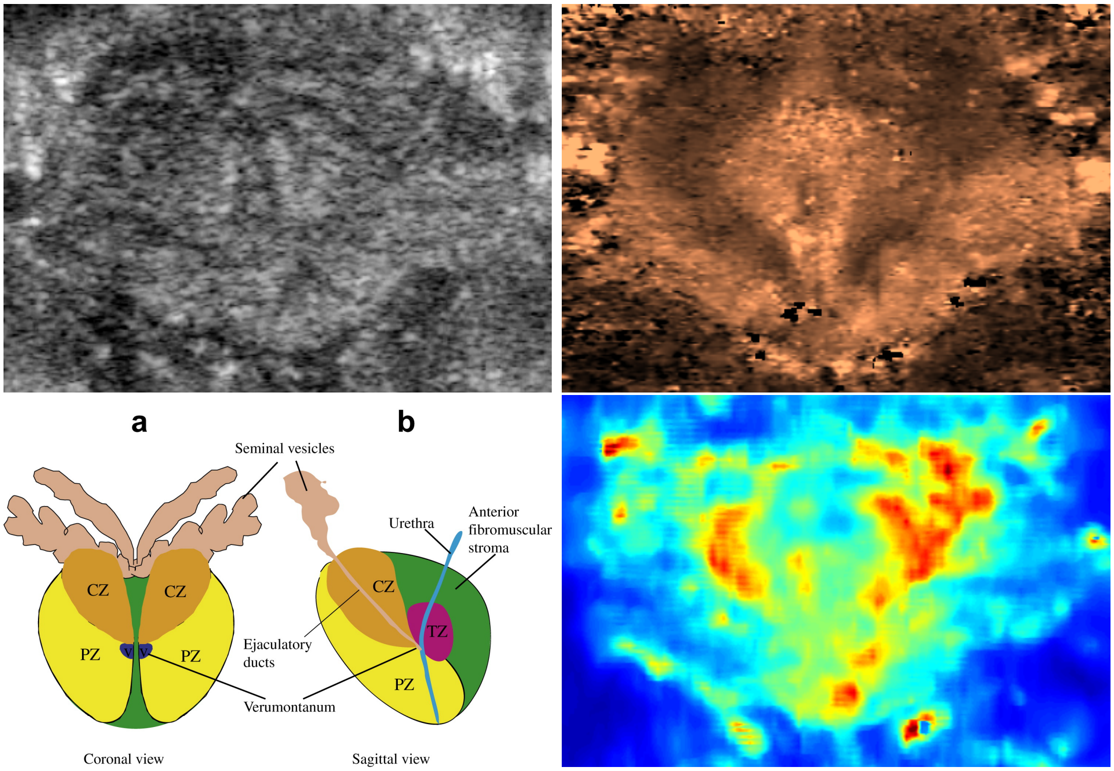

FIGURE 7.8: Coronal B-mode (top left), ARFI (top right), and maximum value MAPE filtered SWEI (bottom right) images showing typical anatomy of the prostate (bottom left, *reproduced with permission from [119].*). The B-mode image is low quality as this patient was acquired prior to developing the high quality B-mode acquisition. The ARFI and SWEI images both depict a softer peripheral zone and stiffer central gland that surrounds a softer region in the center of the prostate where the ductal structures are located.

the bladder) is at the top of the coronal sections and the left side of the sagittal sections, and the rectal wall is located at the bottom of the axial and sagittal planes. The left and right orientation of the prostate in the coronal and axial images is as seen from above the patient lying in the supine position, such that patient left is on the right side of the image and patient right is on the left side of the image.

The first case study, shown in figure 7.9, displays the images and pathology slide associated with a large Gleason 3 tumor primarily localized on one side of the prostate close to the apex, although a small amount of bilateral cancer is present. In the axial section of the ARFI image, a large dark (stiff) region is visible on the patient left

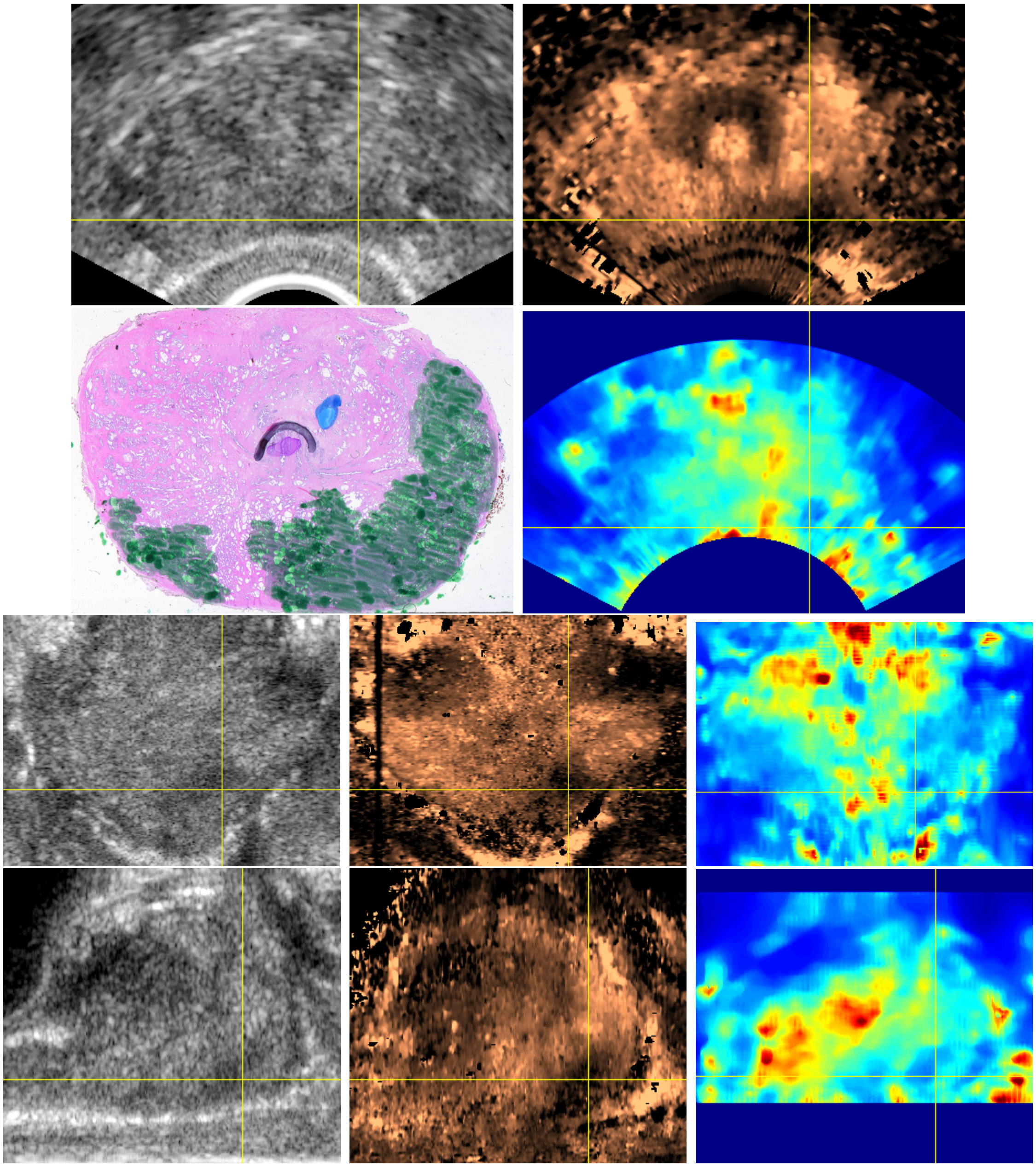

Figure 7.9: Whole mount pathology image (second row, left image) of a confirmed Gleason grade 3 tumor (green) with the corresponding axial B-mode (top row, left), ARFI (top row, right), and SWEI (second row, right) images. The third and fourth rows depict coronal and sagittal sections, respectively, of the B-mode, ARFI, and SWEI volumes from left to right. For all images, the yellow crosshairs indicate the orthogonal planes. A stiff region in the ARFI images is clearly visible in the posterior apex on the patient left, and correlates well with the cancerous region from the histology data. The B-mode images also show a slightly hypoechoic region where the cancer is located, but the ARFI images have better contrast and CNR. The SWEI images depict similar anatomical structure to the ARFI image, but the cancerous region exhibits slower speeds (i.e., appearing soft).

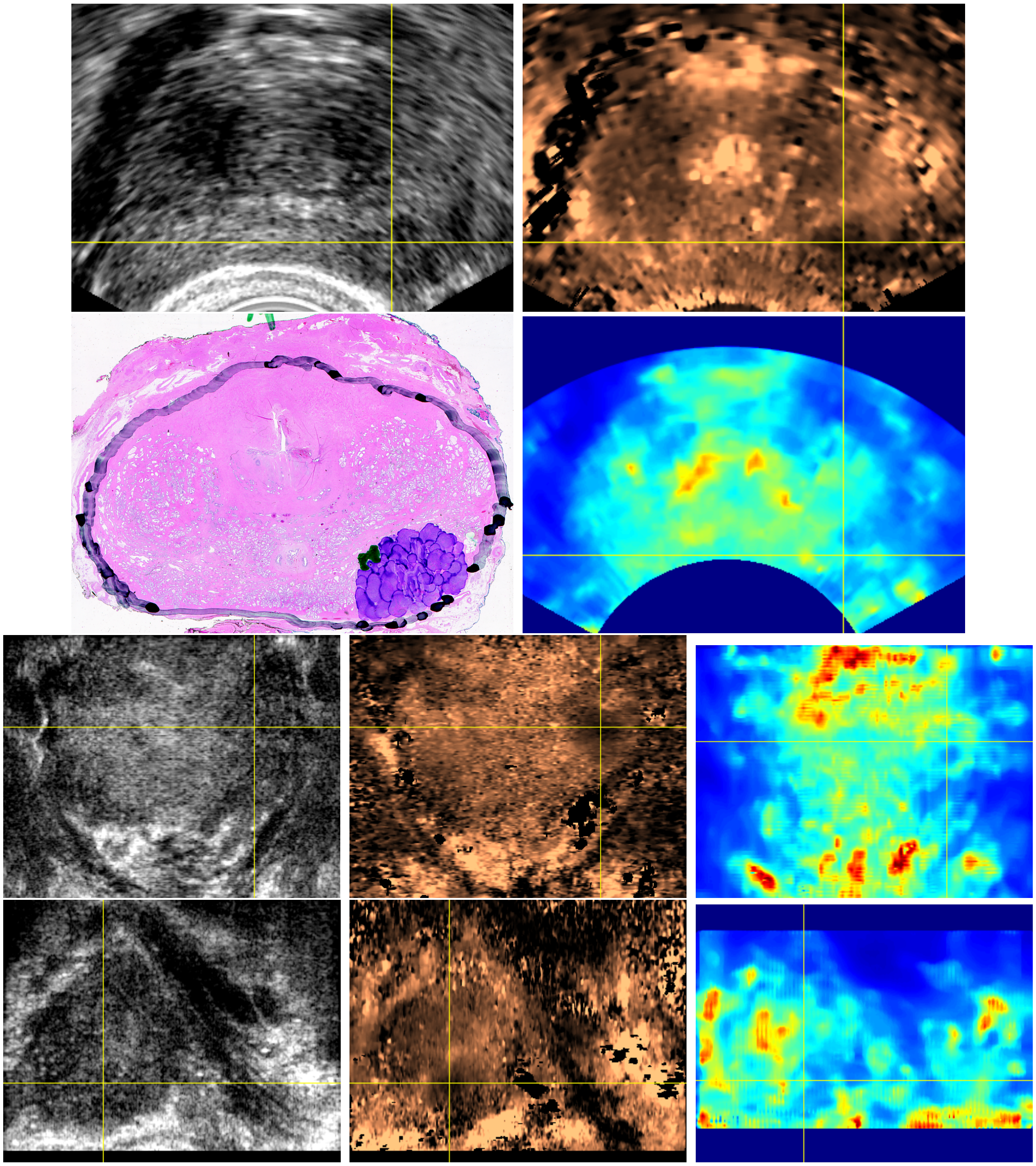

Figure 7.10: Whole mount pathology image (second row, left image) of a confirmed Gleason grade 4 tumor (purple) with the corresponding axial B-mode (top row, left), ARFI (top row, right), and SWEI (second row, right) images. The third and fourth rows depict coronal and sagittal sections, respectively, of the B-mode, ARFI, and SWEI volumes from left to right. For all images, the yellow crosshairs indicate the orthogonal planes. A small, stiff region is visible in all three orthogonal planes in the ARFI image and corresponds to the location of the cancer in the pathology volume. This region is also visible as hypoechoic in the B-mode volume, although many other hypoechoic regions are also visible. Similar to figure 7.9, the SWEI images do not show a stiff lesion in this region of the prostate.

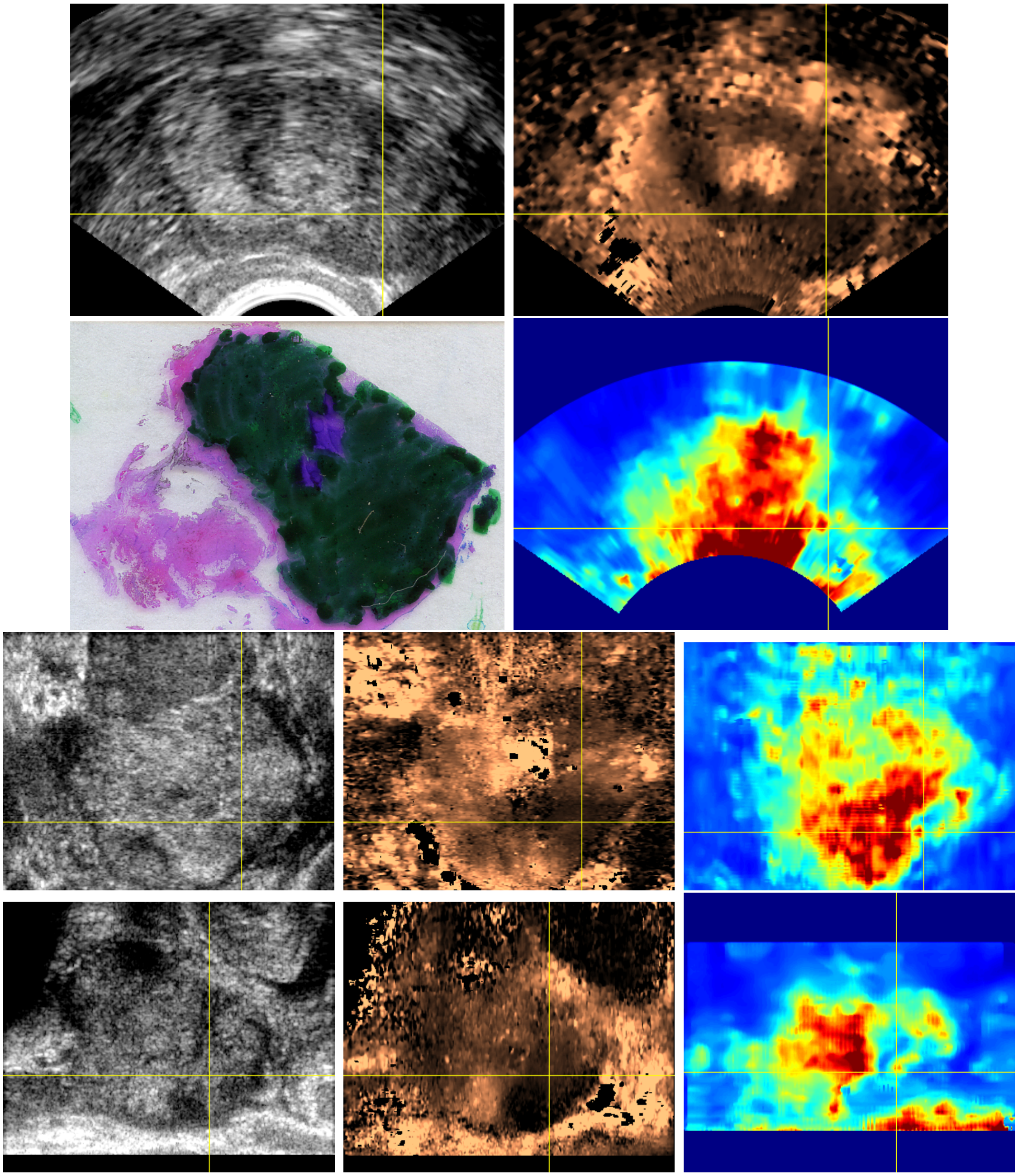

FIGURE 7.11: Whole mount pathology image (second row, left image) of a confirmed Gleason grade 4 (purple) and grade 3 (green) tumor with the corresponding axial B-mode (top row, left), ARFI (top row, right), and SWEI (second row, right) images. The third and fourth rows depict coronal and sagittal sections, respectively, of the B-mode, ARFI, and SWEI volumes from left to right. For all images, the yellow crosshairs indicate the orthogonal planes. A large stiff region is visible in the ARFI images on the patient left side that surrounds the urethra, which is the soft structure in the center of the prostate visible in the axial plane. In the SWEI images, the patient left appears as generally stiffer than the contralateral side, however, in the region chosen from the ARFI image, the cancer exhibits slower speeds (i.e., appearing soft).

side (right side of image) that corresponds to a slightly hypoechoic region in the B-mode image. In this patient, the B-mode image is low quality as this data set was acquired prior to developing the high quality B-mode acquisition. In the axial SWEI image, no obvious structure corresponding to the stiff region in the ARFI image is visible. Analyzing the coronal and sagittal planes in figure 7.9, the hypoechoic region is visible in all three planes as is the stiff structure in the ARFI images; however, the SWEI image does not show a stiff region.

A second case study, shown in figure 7.10, was chosen with the pathology report detailing a small Gleason 4 tumor localized on one side of the prostate close to the base. In the axial section of the ARFI image, a stiff region is visible on the patient left side (right side of image) that corresponds with the hypoechoic region in the B-mode image. The B-mode image also shows a hypoechoic region located on the patient right side, anterior to the prostate, which is likely a large blood vessel. Again, for this patient, in the axial SWEI image, no obvious structure corresponding to the stiff region in the ARFI image is visible. Analyzing the coronal and sagittal planes as well, the hypoechoic region is visible only in the axial and coronal B-mode planes, but the stiff structure in the ARFI images has very good agreement between all three planes. The SWEI images, however, do not indicate a stiff region where the cancer was located.

The final case study, shown in figure 7.11, has a very large tumor consisting of both Gleason 3 and Gleason 4 cancer. The ultrasound data in this case was not well oriented along the apex-to-base axis of the prostate, as seen in the coronal sections, and therefore, the pathology slide is likely not in the same plane as the axial ultrasound data. Additionally, the pathology slide used in this case was slightly torn and the capsule is not completely intact; however, the tumor in this slice occupies over 50% of the area on the slide. As seen in all three sections of the ARFI data, the tumor is very stiff relative to the background and appears as almost zero displacement in some regions. The SWEI coronal image for this patient indicates that the patient left (right side of the images) is stiffer than the patient right side, however, in visualizing the cancerous region in all three planes, there is a significant portion of the cancer that appears soft in the SWEI images.

7.6 SWEI Image Quality

Based on the *in vivo* images, it is hypothesized that both high shear wave speeds and reflection artifacts are contributing to a degradation in SWEI image quality. Thus, multiple experiments were performed using a phantom with a stiff spherical inclusion (88 kPa, 10 mm diameter, 10 kPa Young's modulus background). Initially, images (figure 7.12) were acquired with the combined ARFI/SWEI *in vivo* sequence. As compared to target imaged in figures 7.6 and 7.7, the shear wave speed of both the background and lesion are higher, and the stiffness ratio of the lesion to the background is much higher (8.8 versus 3.5), which results in more energy being reflected at the boundary. Both of these changes result in a much more challenging imaging condition for the SWEI data as the faster wave propagation is more difficult to image and the reflection artifacts will be more pronounced.

As seen in the left column of figure 7.12, the ARFI images at two time steps after force cessation (0.375 ms and 0.75 ms top and bottom images, respectively) both clearly depict the correct target geometry with high contrast. The top row of SWEI images corresponds to the MAPE filtered images and the bottom row of SWEI images is the linear regression images. The left propagating wave, right propagating wave, and maximum value images are displayed from left to right in the three columns. Based on the poor image quality portrayed by the SWEI images, three primary issues are henceforth investigated: the maximum and minimum observable shear wave speed, the conditions necessary to apply a directional filter, and the impact of a restricted lateral field of view.

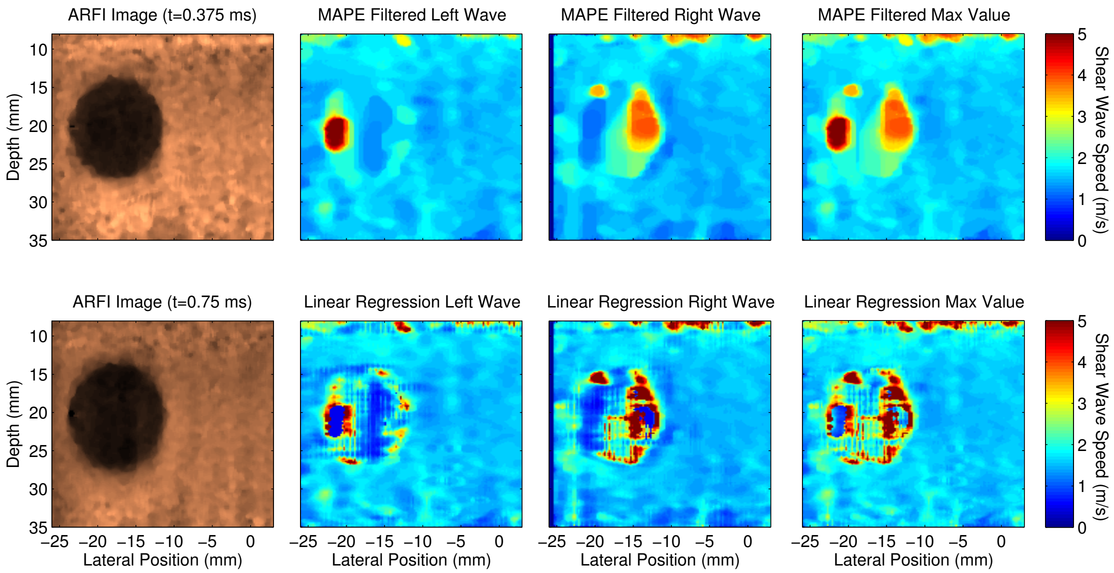

FIGURE 7.12: Matched ARFI and SWEI images of a 88 kPa, 10 mm diameter spherical lesion target in a 10 kPa Young's modulus background. The left column of figures is the ARFI images at two time steps after force cessation (0.375 ms and 0.75 ms top and bottom images, respectively). The top row of SWEI images corresponds to the MAPE filtered images and the bottom row of SWEI images is the linear regression images. The left, right, and maximum value images are displayed from left to right in the three columns. The ARFI images clearly visualize a very stiff structure with well defined boundaries, however, the SWEI images are all corrupted by reflection artifacts, and are therefore very low quality compared to the ARFI images.

7.6.1 Observable Shear Wave Speed Range

To estimate the maximum and minimum observable shear wave speeds, the lateral positions of the tracks as well as the first and last temporal sample must be considered. The track lines for the off-axis data were located beginning at 1.89 mm from the push location and had an inter-beam spacing of 0.76 mm such that the last lateral position was at 5.69 mm. Additionally, the first temporal sample is 0.5 ms after radiation force is first applied, and the last temporal sample is 5 ms after force cessation. Lastly, it is further assumed that for a certain lateral location to observe a shear wave, both the leading edge of the shear wave and the maximum displacement must occur within the temporal tracking window (0.5 - 5 ms).

Table 7.1: The minimum and maximum observable shear wave speeds for the *in vivo* SWEI sequence as a function of the number of lateral locations the shear wave must propagate though. For the minimum shear wave speed, the wave must be observed at the N positions closest to the radiation force excitation, whereas for the maximum shear wave speed, the wave must be observed at the furthest N positions.

Number of Lateral Locations	6	5	4	3	2
Minimum Shear Wave Speed (m/s)	1.14	0.99	0.83	0.68	0.53
Maximum Shear Wave Speed (m/s)	2.44	3.96	5.48	7.00	8.52

The leading edge of the shear wave is defined as originating at the first zero crossing of the far-field representation of the radiation force excitation (i.e., a sinc function with the first zero crossing at $+\lambda z/D = 0.67$ mm). Additionally, the maximum displacement is assumed to originate from the center of the radiation force excitation (i.e., 0 mm laterally). The minimum and maximum shear wave speed are also dependent on the number of track locations used to observe the shear wave, such that at least 2 lateral locations are required. Since values for the distance the shear wave needs to travel and the required temporal range have been defined, $c = x/t$ can be utilized, where c corresponds to the shear wave speed, x is the required propagation distance, and t is the first or last temporal sample.

The resulting minimum and maximum observable shear wave speeds are given in table 7.1 as a function of the required number of track locations. By necessitating the shear wave to be fully observed at all 6 lateral locations, only a narrow range of shear wave speeds can be imaged (1.14, 2.44) m/s; however, if the shear wave only needs to be observed at two lateral locations, the shear wave speed range is much larger (0.53, 8.52) m/s.

The data in table 7.1 are also supported by figure 7.13, which depicts displacement and velocity through time profiles from the shear wave data set collected in figure 7.12. In figure 7.13, the left column corresponds to data from push and track

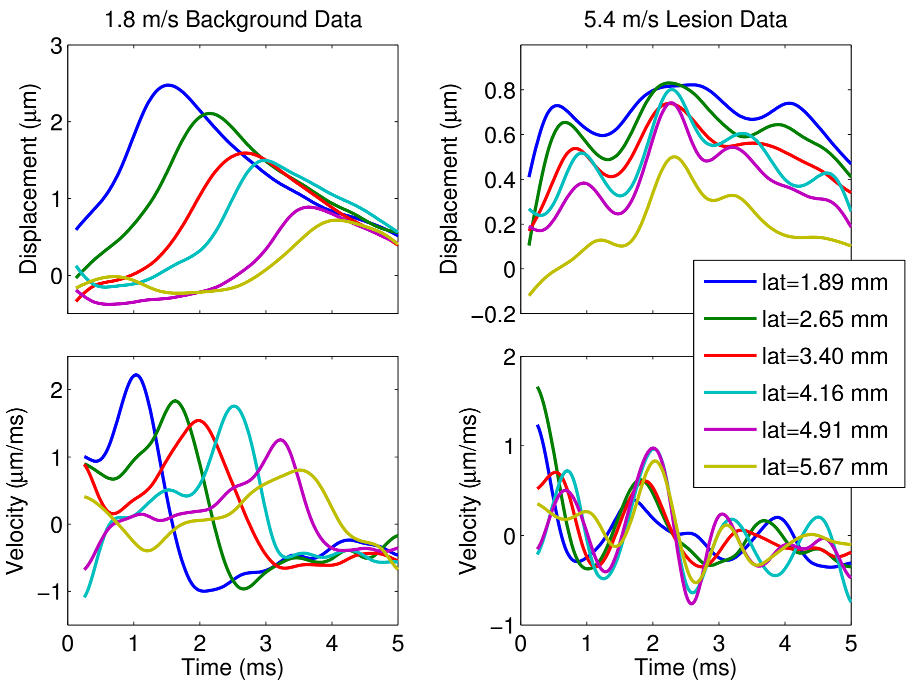

FIGURE 7.13: Displacement (top) and velocity (bottom) through time profiles acquired in both a soft background (1.8 m/s, left) and a stiff lesion (5.4 m/s, right) using the *in vivo* sequence. In the background material (left), the arrival time of the wave is apparent in both the displacement and velocity data; however, in the lesion (right), multiple reflected shear waves confound both the displacement and velocity data. Additionally, the arrival time for the velocity data cannot be determined at the first two lateral locations since the peak velocity is associated with the first temporal sample.

locations all within the background material, which has a speed of 1.8 m/s. The arrival time of the wave is apparent in both the displacement (figure 7.13, top left) and velocity (figure 7.13, bottom left) data. The peak in the velocity data occurs earlier in time than the displacement data since the velocity peak corresponds to time required for the leading edge of the shear wave to arrive at a given location, whereas the displacement peak corresponds to the propagation time from the center of the excitation (i.e., 0 mm laterally).

Data from the region with the lesion (5.4 m/s shear wave speed) are also presented (figure 7.13, right column). The displacement data (figure 7.13, top right) has multiple peaks through time, which correspond to multiple shear waves propagating through each location as they are reflected within the lesion; however, the first peak in time is distinct and corresponds to the propagation from the push rather than reflected waves. The velocity data (figure 7.13, bottom right) portray the issues with identifying the leading edge of a fast shear wave as compared to using the peak displacement. Specifically, for the first two lateral locations, the peak velocity occurs at the first time step, which indicates that the true peak velocity potentially occurred earlier than the first temporal sample; thus, these lateral locations must be discarded if using the velocity data.

7.6.2 Directional Filter

In addition to determining the range of observable shear wave speeds, the conditions necessary for applying a directional filter were investigated. The filter is applied by taking a two-dimensional fast Fourier transform (2DFFT) in the lateral-time domain, zeroing out data in the second and fourth quadrants (corresponding to backwards propagating waves), and obtaining the real component of the inverse 2DFFT [30]. To investigate when a directional filter can be appropriately applied, data sets with high spatial (Δx = 0.1 mm) and temporal (Δt = 0.1 ms, upsampled with cubic spline interpolation to 50 kHz) sampling were acquired using a prototype 12L4 linear array with the same push parameters as the ER7B (4.6 MHz center frequency, 300 cycles, F/2 focal geometry).

Eight data sets were acquired with different speckle realizations in a uniform phantom that has a Young's modulus of 10 kPa. After displacement estimation, each data set was averaged ±1.3 mm around the focal depth (corresponding to a quarter of the depth of field), and then the eight data sets were averaged together to reduce noise. The resulting velocity data are shown in the left image of figure 7.14, which portrays shear wave propagation as a function of time and lateral position.

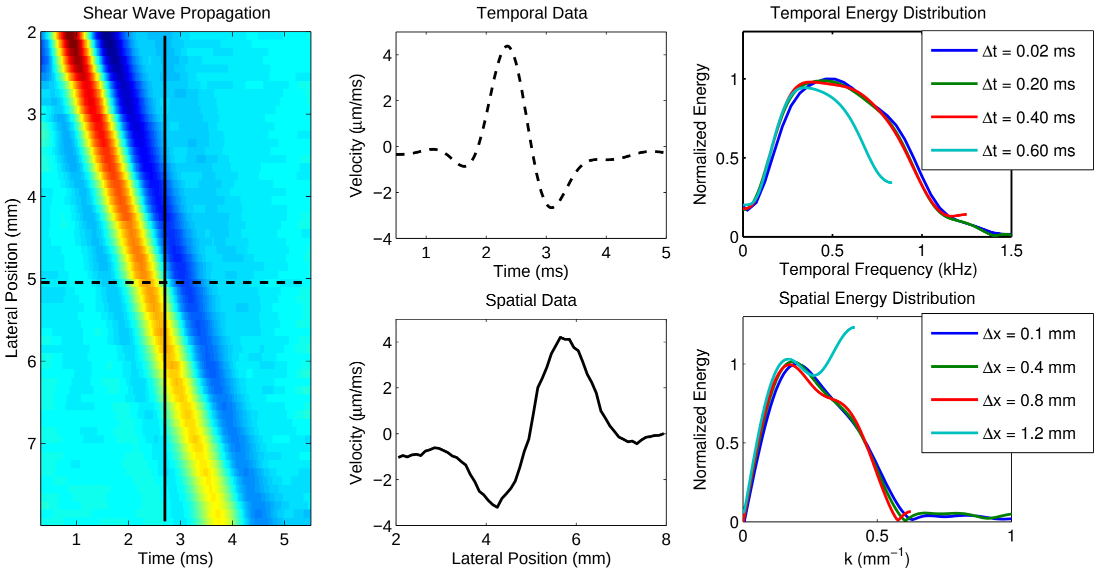

FIGURE 7.14: Shear wave propagation in a uniform medium as a function of time and lateral position (left) is presented along with the velocity data at a fixed lateral location (middle column, top) and fixed time (middle column, bottom). The spectral content both temporally (right column, top) and spatially (right column, bottom) are depicted as a function of the sampling rate, indicating corruption of the spectral data when sampled below the Nyquist criteria (e.g., $\Delta t \leqslant 0.33$ ms and $\Delta x \leqslant 0.83$ mm).

The middle column of figure 7.14 depicts data at either a fixed lateral location through time (top, dashed line in left image) or at a fixed time after the push as a function of distance from the push (bottom, solid line in left image). Utilizing this low-noise, highly sampled data set, it is possible to investigate the spectral content both temporally (figure 7.14, top right) and spatially (figure 7.14, bottom right). Since the signal starts from baseband (i.e., zero frequency), the bandwidth is defined as the maximum frequency present in the data set, which was determined to be ±1.5 kHz temporally and ± 0.6 mm^{-1} spatially. Correspondingly, based on Nyquist theory, the minimum sampling frequency must be twice the maximum frequency to avoid aliasing in the data; thus, the data should be sampled with a $\Delta t \leqslant 0.33$ ms and $\Delta x \leqslant 0.83$ mm.

In addition to depicting the original spectral content of the data set, the right column of figure 7.14 also depicts the spatial and temporal spectral content after the data in the center column were downsampled either laterally or temporally. When the data are downsampled temporally (figure 7.14, top right), slight distortion is seen at the high frequency content for Δt = 0.4 ms and significant distortion of the energy is apparent at Δt = 0.6 ms, which is expected when sampling below the Nyquist criteria. The spatial downsampling (figure 7.14, bottom right) has both subtle (Δx = 0.8 mm) and more apparent (Δx = 1.2 mm) effects, such that even if sampled below the suggested Nyquist criteria of $\Delta x \leqslant 0.83$ mm, there is some deviation from the highly sampled case, indicating that spatial frequencies higher than ± 0.6 mm^{-1} are contained within the data.

Although figure 7.14 demonstrates the effect of downsampling in 1D, the directional filter is applied after a 2DFFT. Thus, the 2D spectral content is depicted in figure 7.15, demonstrating the effects of downsampling laterally (rows) and temporally (columns). When sufficiently sampled (figure 7.15, top left), the Fourier domain representation of the data is a diagonal cloud of energy orientated in the first and third quadrants, where the slope corresponds to the shear wave speed. As the data are downsampled either in space or time, aliasing is introduced as the data appear off the main diagonal in the incorrect (second and fourth) quadrants. To apply the directional filter, data in the second and fourth quadrants are set to zero and the inverse Fourier transform is obtained. Therefore, when aliasing is present due to undersampling (i.e., bottom row and rightmost column of figure 7.15), by applying the directional filter, some of the signal is removed.

This loss of signal energy is demonstrated in figure 7.16, which depicts the velocity through time profiles at a fixed lateral position (5.2 mm) before (dashed line) and after (solid line) applying the directional filter. When sampled above the Nyquist criteria spatially (top 3 rows), the filtered data appear similar to the raw data; however, when undersampled spatially (bottom row), significant morphology changes

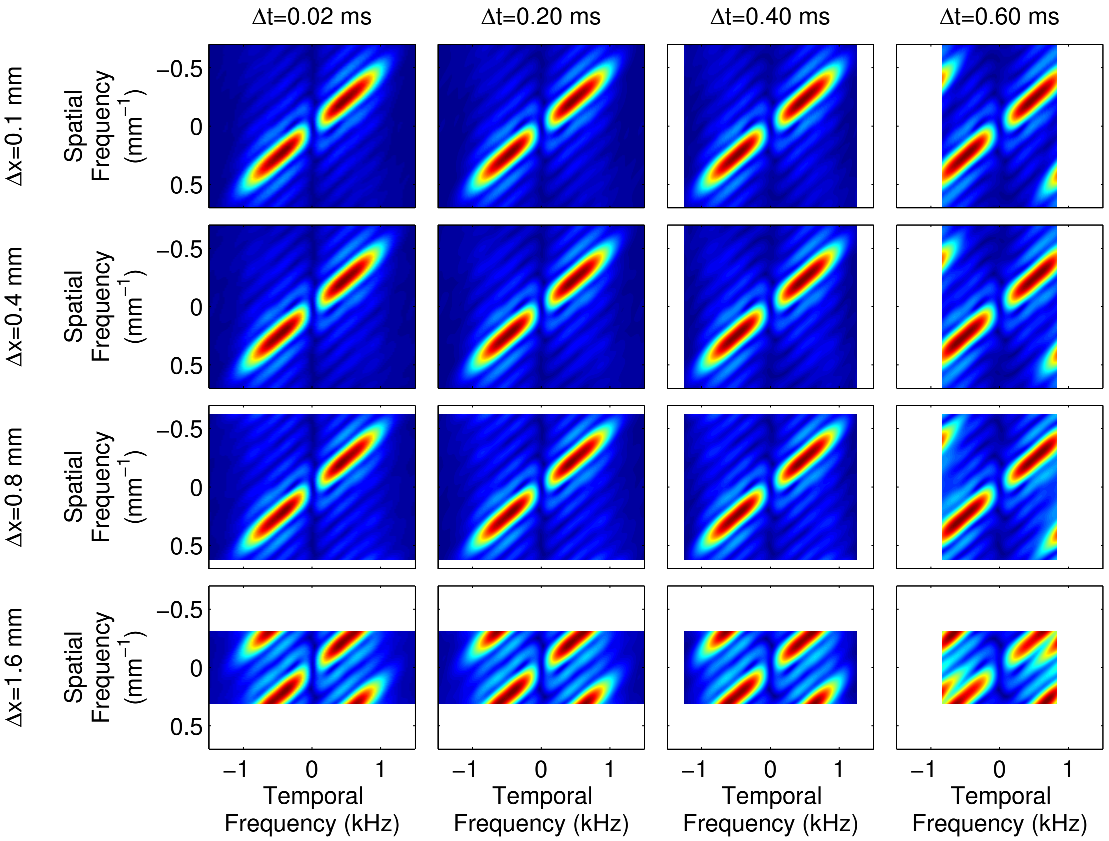

Figure 7.15: The 2D spectral of shear wave propagation is depicted, demonstrating the effects of downsampling laterally (rows) and temporally (columns). When the data are undersampled laterally or temporally, aliasing is introduced as energy appears off the main diagonal in the incorrect (second and fourth) quadrants.

are apparent in the velocity profile, including a shift of the time when the peak velocity occurs.

Although the loss of shear wave energy and change in the morphology shown in the velocity profiles in figure 7.16 are not desirable, it is still possible to accurately estimate the shear wave speed. Thus, a separate data set was acquired to demonstrate the effect of the directional filter in a region when a reflected wave is present. The spherical lesion phantom shown in figure 7.12 was again utilized with a similar sequence to figure 7.14. In this case, however, the averaging across different speckle realizations was not practical since any small shift in the lesion location would cor-

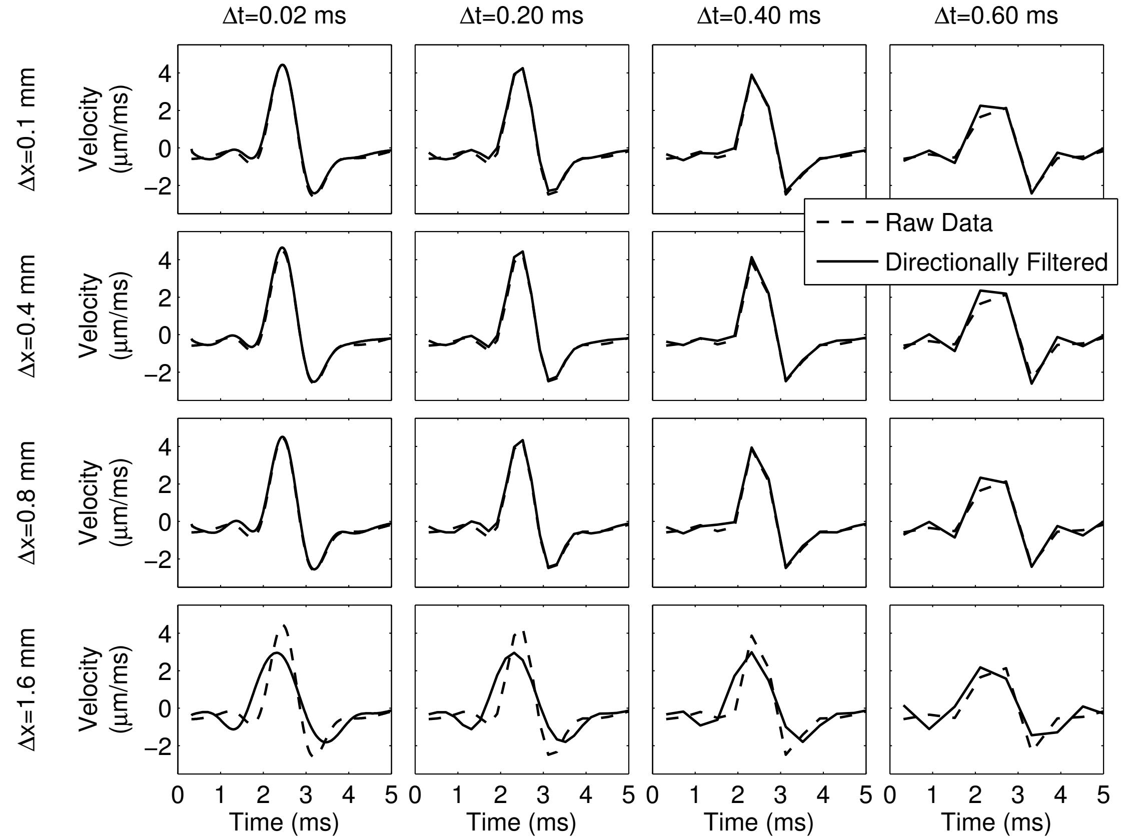

FIGURE 7.16: Velocity through time profiles at a fixed lateral location (5.2 mm) before and after applying a directional filter with varying amounts of downsampling both spatially (rows) and temporally (columns). When undersampled spatially (bottom row), a significant amount of energy is removed by the directional filter and the time of peak velocity is modified.

rupt the averaging; therefore, to reduce the noise laterally, a 2 mm^{-1} low-pass filter was applied spatially to a single acquisition before performing any data analysis.

The resulting velocity data, shown in figure 7.17, depict much more complicated shear wave behavior than the uniform region imaged in figure 7.14. The lesion is 10 mm in diameter and the push was approximately centered in the lesion, such that the boundary is located at 6 mm in the left image of figure 7.17. The lesion shear wave speed (5.4 m/s) is also much greater than the background material (1.8 m/s), which results in a strong reflection at the boundary. Additionally, the shear

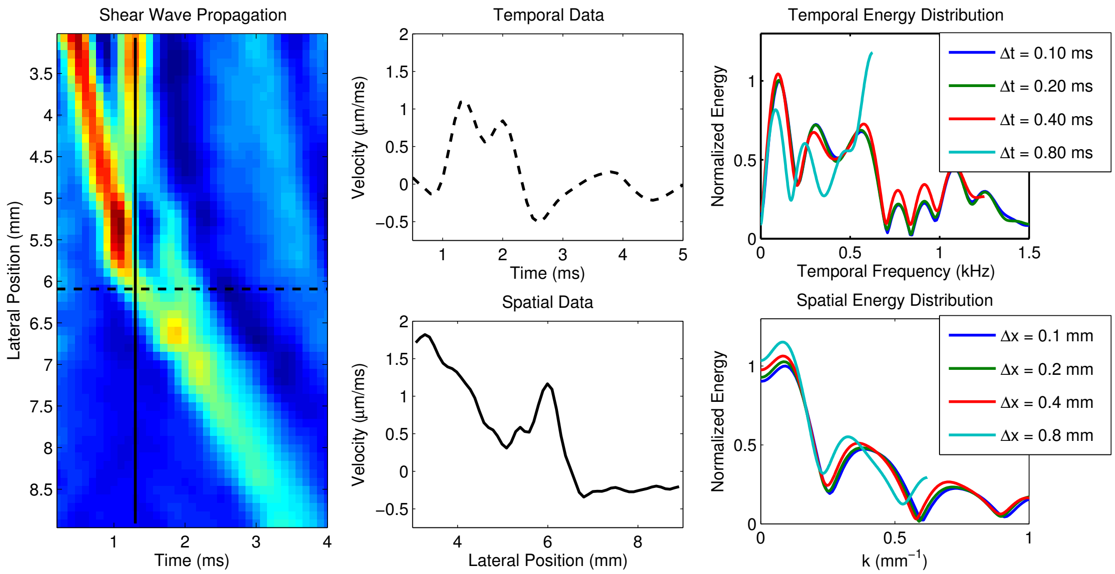

FIGURE 7.17: Shear wave propagation (left image) resulting from a radiation force excitation originating inside a stiff lesion with the lesion boundary at 6 mm laterally depicting both a incident and reflected wave at the boundary. The velocity data at a fixed lateral location (middle column, top) and fixed time (middle column, bottom) as well as the spectral content both temporally (right column, top) and spatially (right column, bottom) are depicted as a function of the sampling rate.

wave that propagates in the negative lateral direction also reflects off of the lesion boundary on that side, thus, there are multiple forward going waves.

The right plots of figure 7.17 depict the spatial and temporal energy distributions as well as the downsampled energy distributions and indicate that this data set has higher spatial frequency content than the data in figure 7.14. Specifically, when downsampled to $\Delta x = 0.8$mm, the data are clearly aliased in the Fourier domain, as seen in the bottom right plot of figure 7.17.

The directional filter was then applied to the original data as well as spatially downsampled data, with the resulting velocity profiles show in figure 7.18. When the data are sufficiently sampled, the directional filter emphasizes the first peak in the velocity profile; however, with insufficient sampling, the second peak in the velocity profile is emphasized incorrectly. Thus, by using the time to peak tissue velocity as

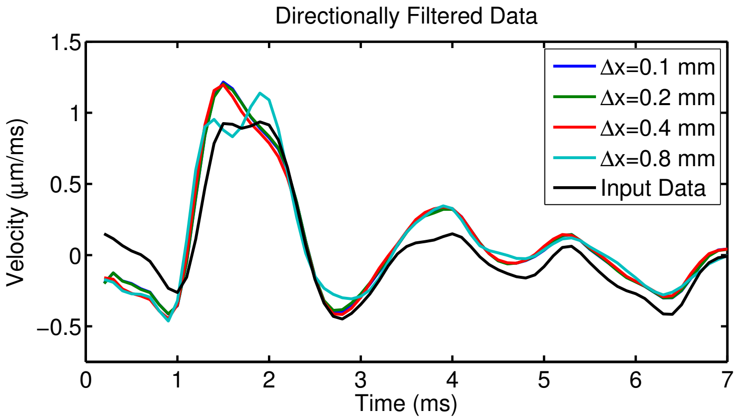

FIGURE 7.18: Velocity data through time are presented before and after applying a directional filter as a function of the lateral sampling frequency. When the data are undersampled laterally, the directional filter incorrectly emphasizes the second peak in the velocity profile, thereby corrupting the wave arrival time estimate.

the wave arrival time, this data set would incorrectly identify the arrival time at this lateral position.

7.6.3 Lateral Field of View

The previous analysis in the Fourier domain looked at the impact of undersampling both laterally and temporally, however, it did not investigate another limitation of the *in vivo* sequence, specifically that it has a restricted lateral field of view (3.8 mm between the first and last lateral location). To determine the impact of this restricted field of view, the data from figure 7.14 was utilized while reducing the lateral and temporal ranges used for the 2DFFT. Figure 7.19 portrays the resulting images for restricting the lateral field of view to 10 mm, 7 mm, 4 mm, and 1 mm (top to bottom rows, respectively) and the total sampling time to 4.7 ms, 3.7 ms, 2.7 ms, and 1.7 ms (left to right columns, respectively).

The use of finite lateral and temporal ranges is equivalent to multiplying by a rect function to the data, which in the Fourier domain corresponds to a convolving with a sinc function. As the range is restricted, the sinc function broadens, resulting in

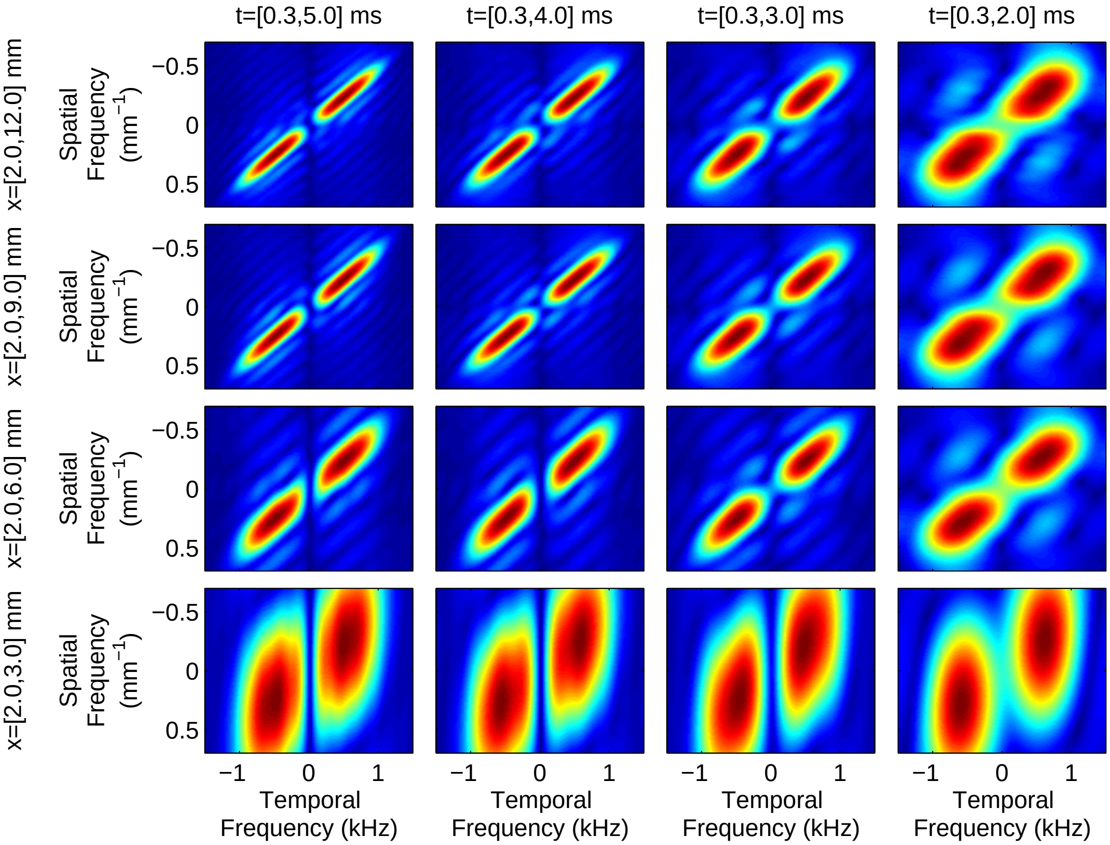

Figure 7.19: The spectral content of the shear wave data from figure 7.14 is presented as a function of the size of the lateral (rows) and temporal (columns) windows. As the window size is reduced, the spectral energy distribution broadens in the respective dimension, which is expected based on the convolution of the spectral data with an increasingly broad sinc function.

blurring in the Fourier domain, as seen in figure 7.19. For estimating a single shear wave speed from the data, this broadening of the energy has little impact. However, once the lateral field of view becomes very restricted (figure 7.19, bottom row), some energy appears in the second and fourth quadrants, so applying a directional filter would inappropriately remove some of the true signal. Additionally, broadening of the Fourier domain profiles restricts the ability to determine any information about the shear wave speed as a function of frequency, such as in the case of dispersion analysis. Lastly, if there are multiple speeds present within a restricted field of view due to heterogeneity, it would be difficult to differentiate the speeds due to the broad energy profile in the Fourier domain.

7.7 Discussion

Although previous work using a curvilinear endfire endocavity transducer has demonstrated the potential of ARFI imaging to visualize prostate cancer, multiple challenges were identified including depth penetration and radiation force excitation beam width [119, 121]. To address these challenges, a three-dimensional *in vivo* prostatic imaging system capable of concurrently acquiring ARFI and SWEI data was developed using the longitudinal array of a biplanar endorectal transducer to achieve tight push beams and increase depth penetration.

After creating the tool set to allow for custom radiation force imaging sequencing on the Siemens Acuson SC2000™ as described in chapter 3, a sequence capable of concurrently acquiring ARFI and SWEI data was created, as shown in figure 7.1. This radiation force sequence was then tested for both thermal (figure 7.5) and acoustic safety (figure 7.4), and it was determined that acoustic exposure was below the standard FDA threshold for mechanical index and the transducer heating was less than the 6°C safety threshold stated in the IRB protocol.

In addition to evaluating the radiation force imaging sequence for safety, the image quality was also determined, and as demonstrated in figure 7.6, the ARFI images have high contrast and resolution. SWEI images were reconstructed retrospectively after developing new algorithms detailed in section 7.2.5 and are shown in figure 7.7. Although the lesion is clearly visible in these images as well, both the noise and soft-center artifacts reduce the lesion conspicuity.

Two methods were employed to improve the shear wave speed image quality. First, the MAPE adaptive filter detailed in chapter 6 was utilized to reduce the noise. This filter clearly improves image quality deep to 30 mm where the noise is the worst due to lower signal. Second, the maximum shear wave speed value between the left and right propagating waves was portrayed to reduce the impact of the soft-center artifact. By utilizing these two methods, the SWEI image quality was significantly improved, as seen in the right column of the third row of figure 7.7.

In the SWEI images, it was also identified that data shallow to 10 mm is not valid, which is demonstrated in figure 7.7, since the data shallow to 10 mm contains high shear wave speeds not consistent with the phantom calibration. This cutoff depth is expected since 10 mm corresponds to the minimum depth of field of the push beam (computed as $8F^2\lambda$, where F is the $F/\#$ of the push and λ is the wavelength); thus, any depths shallow to 10 mm violate the assumption about a known direction of wave propagation [81].

Based on the improvements made to the SWEI data and the high quality ARFI data that the ER7B was capable of collecting, as seen in figures 7.6 and 7.7, 44 patients expecting robotic radical prostatectomy were imaged using the combined ARFI/SWEI sequence. The resulting B-mode, ARFI and SWEI data were processed and scan converted as detailed in section 7.2. The primary image evaluation was performed using the ARFI data.

The ARFI volumes were first evaluated for their ability to correctly depict known anatomical features with high contrast (figure 7.8, top right) including the peripheral zone and central gland as well as ductal structures. These features are consistently visualized in all of the patients and correlate well with the anatomy visualized in T2-weighted MRI images [86].

Additionally, as demonstrated by the case studies shown in figures 7.9, 7.10, and 7.11, cancerous regions in the prostate tended to appear as stiff, asymmetric regions in the volumetric data. Thus, the ARFI images were evaluated using 6 criteria to determine suspicion for a cancerous region. Three readers collectively reviewed the ARFI image volumes to determine suspicion for cancer, with the results compared to the whole mount pathology.

Only clinically significant tumors were evaluated, defined as tumors >0.5 cm^3 or combined Gleason grade $\geqslant 7$ [60]. In these tumors, the readers correctly identified 24/38 (63%); in the posterior region of the prostate, where ARFI image quality is best, 23/31 (74%) were identified. Tumors were designated as clinically significant based on the whole mount pathology, but, currently, whole mount pathology is only available on a subset of the total patients imaged (29/44, 66%); thus, the images will continue to be evaluated as additional cases are processed with whole mount pathology.

A secondary, retrospective analysis, was performed on the MAPE filtered, maximum value SWEI images. As compared to the ARFI image volumes, the SWEI images largely appear to have lower resolution and worse image quality. However, as seen in figure 7.8, both the ARFI and SWEI images portray the general anatomy, although the ductal structures are not visible in the SWEI image. In the case studies chosen based on the suspicion of cancer in the ARFI images, the SWEI images generally depict slower shear wave speeds in the cancerous regions (i.e., appearing soft).

Based on these *in vivo* SWEI images, a further investigation into parameters affecting the quality of the shear wave data was performed. Specifically, it was shown in figure 7.18 that the lateral sampling of the current SWEI sequence prevents the use of a directional filter due to the Nyquist sampling criteria. However, it is expected that reflected waves are contained with the SWEI data set, especially close to the boundary of the prostate, which should reflect the shear wave almost completely. Additionally, the maximum and minimum shear wave speeds that can be observed with this sequence are given in table 7.1, indicating a limited ability for the sequence to image fast shear wave speeds depending on the number of lateral locations used in the computation. Lastly, it was determined that the limited lateral field of view for the SWEI data does not have a large impact on the image quality.

7.8 Conclusions

In this work, a 3D imaging system was developed to address the resolution and depth penetration limitations of previous studies, which have shown the ability for ARFI imaging to detect cancerous regions in the prostate. After optimization for ARFI image quality, patients scheduled to undergo a robotic radical prostatectomy procedure were imaged. When the study was initiated, it was recognized that by using the Siemens Acuson SC2000™, the off-axis response to the radiation force excitation could concurrently be recorded without losing ARFI image quality. The volumetric imaging system developed has demonstrated the ability to reliably acquire high quality ARFI image volumes of the prostate clearly depicting anatomical features of the prostate [86]; however, multiple challenges to using the current SWEI sequence in the prostate were identified and should be addressed in future studies if quantitative shear wave speed information is desired. After a blinded evaluation of the ARFI image volumes for suspicion of prostate cancer, three readers correctly identified 63% of the clinically significant tumors and 74% of the clinically significant tumors in the posterior region, showing great promise for using ARFI to detect prostate cancer.

8

Conclusions

The aim of this thesis is to contribute to both the technical development and clinical applications of ARFI and SWEI imaging, specifically in the early detection of prostate cancer, which is the most common non-cutaneous cancer in men in the United States [1]. To accomplish these goals, new ultrasound technology and data processing hardware were utilized to allow for concurrent acquisition and generation of high quality ARFI and SWEI images in real-time. Additionally, new ARFI and SWEI imaging and processing methods were developed to improve image quality, which are currently being utilized in a pilot study to determine the sensitivity of ARFI imaging for detecting prostate cancer.

The SC2000™ radiation force prototyping tools developed in chapter 3 and GPU processing methods detailed in chapter 4 provided the means to generate flexible ARFI and SWEI imaging sequences allowing for acquisition and evaluation of clinical images in real-time. This powerful tool set was then used to develop a new multi-focal zone ARFI imaging method in chapter 5, which provided improved ARFI image quality throughout an extended depth of field as compared to previous methods. Additionally, a new algorithm for SWEI image processing was developed using an adaptive filter based on a maximum *a posteriori* estimator as detailed in chapter 6, demonstrating increases in the contrast to noise ratio of lesion targets upwards of 50% in FEM simulated, ultrasonically-tracked data.

These methods for acquisition and processing were then applied to volumetric *in vivo* ARFI and SWEI data in patients undergoing robotic radical prostatectomy procedures in chapter 7. Multiple challenges were identified with the SWEI sequence, however the ARFI image volumes portrayed anatomical structures with high contrast, which correlated well with T2 MRI images [86]. After a blinded evaluation of the ARFI image volumes for suspicion of prostate cancer, three readers correctly identified 74% of posterior clinically significant tumors, showing great promise for using ARFI to visualize prostate cancer.

8.1 Future work

The work presented in this dissertation provides evidence that ARFI imaging can be used to accurately identify cancerous regions in the prostate, with the potential to guide procedures such as needle biopsy and focal therapy. However, several challenges have been identified with the implementation and image quality for both ARFI and SWEI that should be addressed to improve the research and clinical capability of prostate radiation force imaging.

The radiation force prototyping tool set should continue to be developed and expanded. One primary issue with the current tool set is the time required to acquire a radiation force sequence. Although the data are saved very quickly using the IQ data pipeline, the total acquisition time for a single frame is at least 5 seconds since the scanner must switch between the live B-mode and radiation force imaging cases. The ability to stage the sequence parameters in memory while in live B-mode would significantly reduce the time it takes between starting the acquisition and returning to live B-mode. Additionally, the loading of the parameter tables could be improved through new tools available in the scanner software. Lastly, the real-time processing and display tools developed in chapter 4 should be integrated into the sequence prototyping tool set to allow for real time visualization of the acquired data.

The MAPE adaptive filter for improving SWEI image quality could also be investigated further. Chapter 6 provided a model for using a maximum *a posteriori* estimator to improve image quality, however the prior chosen in this work was limited to comparing shear wave speed estimates at nearby pixels. The estimator could be explored further including investigation into other prior distributions as well as the incorporation of other data types into the shear wave speed estimate. For example, incorporating B-mode data could provide automated boundary detection, which would influence the use of directional filters and preferential weighting of left versus right propagating shear waves. Additionally, because ARFI images are typically higher resolution and have fewer artifacts at a fixed depth, the displacement data, which is inversely proportional to the shear modulus, could be used directly in the estimation of the SWEI data.

Additional image sequence and data processing optimization should be performed for both the ARFI and SWEI data sets. Specifically for ARFI images, additional depth penetration is necessary as 74% of posterior clinically significant tumors were identified, but only 63% throughout the whole gland, indicating poorer image quality at depth. ARFI image quality could be improved throughout the prostate by using tighter F/# pushing beams with the method developed in chapter 5 as well as adding both shallower and deeper focal depths. Additionally, depth penetration could be improved by optimizing the transducer geometry and bandwidth to improve elevation focusing and to use lower frequency pushes. These sequence improvements would also be applicable to the SWEI data sets, although other modifications are necessary as well. Primarily, additional parallel receive beams per push should be acquired to improve the lateral sampling and field of view of the off-axis data, which would permit a directional filter to be applied.

8.2 Clinical and Technical Contributions and Implications

The aim of the work in this thesis was to contribute to both the technical development and clinical applications of ARFI and SWEI, specifically to improve visualization of prostate cancer. Significant contributions were made to technical aspects of radiation force imaging in the form of a new method of multi-focal zone ARFI imaging and an adaptive filter algorithm for SWEI that had not been previously used in the field. If widely adopted, these methods and algorithms could provide significant image quality improvements in many imaging scenarios, not just prostate imaging.

With regards to clinical applications, the goal of the work in this thesis was to correctly identify clinically significant prostate cancer, and, as detailed in chapter 1 there currently are multiple imaging technologies being investigated, of which radiation force based ultrasound elasticity imaging is one. Multi-parametric MRI has demonstrated high sensitivities and specificities for visualizing clinically significant prostate cancer; however, to obtain the best image quality requires the use of an endorectal coil and the imaging can take over 45 minutes to complete the T2, DCE, DWI, and ADC imaging sequences, which results in high cost as well as significant patient discomfort. Therefore, ultrasound-based methods, such as ARFI and SWEI, are highly desirable to reduce cost, patient discomfort, and examination duration, but only if they similarly provide high sensitivity and specificity for detection of clinically significant prostate cancer.

The work in this thesis has demonstrated a method for acquiring high quality ARFI images of the prostate capable of portraying cancer with significant contrast; however, this was a pilot study performed using prototype ARFI imaging tools along with obsolete transducer technology, and it is therefore expected that additional optimization and effort towards commercialization would significantly improve the results presented in this thesis. Additionally, this dissertation provided a method for concurrently acquiring SWEI data along with the ARFI data, and although the current SWEI sequence had flaws, if these challenges are addressed, SWEI images could provide confirmation of suspicious regions. Lastly, as was identified in chapter 7, B-mode ultrasound images often portray cancerous regions as hypoechoic. Therefore, ARFI, SWEI, and B-mode images could all be utilized to generate a combined index of suspicion for a region in the prostate, in a similar manner to the multiple sequences used in multi-parametric MRI. If implemented using this proposed scheme, and shown to have high sensitivity and specificity, ultrasound imaging could potentially provide a fast, low cost screening tool for men suspected of having prostate cancer, which would have an immense clinical impact.

Bibliography

[1] Prostate cancer home page - national cancer institute.

[2] *NVIDIA CUDA Programming Guide v2.3.* NVIDIA Co., Santa Clara, CA, 2009.

[3] *NVIDIA CUDA Programming Guide v3.0.* NVIDIA Co., Santa Clara, CA, 2010.

[4] Sarfraz Ahmad, Rui Cao, Tomy Varghese, Luc Bidaut, and Ghulam Nabi. Transrectal quantitative shear wave elastography in the detection and characterisation of prostate cancer. *Surgical endoscopy*, March 2013.

[5] Herbert Augustin, Andreas Erbersdobler, Peter G Hammerer, Markus Graefen, and Hartwig Huland. Prostate cancers in the transition zone: Part 2; clinical aspects. *BJU international*, 94(9):1226–9, December 2004.

[6] Paul E Barbone and Nachiket H Gokhale. Elastic modulus imaging: on the uniqueness and nonuniqueness of the elastography inverse problem in two dimensions. *Inverse Problems*, 20(1):283–296, February 2004.

[7] Richard G Barr, Richard Memo, and Carl R Schaub. Shear Wave Ultrasound Elastography of the Prostate: Initial Results. *Ultrasound Quarterly*, 28(1), 2012.

[8] Eric Bavu, Jean-Luc Gennisson, Mathieu Couade, Jeremy Bercoff, Vincent Mallet, Mathias Fink, Anne Badel, Anaïs Vallet-Pichard, Bertrand Nalpas, Mickaël Tanter, and Stanislas Pol. Noninvasive in vivo liver fibrosis evaluation using supersonic shear imaging: a clinical study on 113 hepatitis C virus patients. *Ultrasound in medicine & biology*, 37(9):1361–73, October 2011.

[9] John Benson and Liexiang Fan. Tissue strain analytics: A complete ultrasound solution for elastography. Siemens, Dec 2012.

[10] J Bercoff, M Tanter, and M Fink. Supersonic shear imaging: a new technique for soft tissue elasticity mapping. *Ultrasonics, Ferroelectrics and Frequency Control, IEEE Transactions on*, 51(4):396–409, April 2004.

[11] Jeremy Bercoff. Shearwave™ elastography. SuperSonic Imagine, 2008.

[12] Wendie A Berg, David O Cosgrove, Caroline J Doré, Fritz K W Schäfer, William E Svensson, Regina J Hooley, Ralf Ohlinger, Ellen B Mendelson, Catherine Balu-maestro, Martina Locatelli, Christophe Tourasse, Barbara C Cavanaugh, Anne Tardivon, Joel Gay, and Jean-pierre Henry. Shear-wave Elastography Improves the Specifi city of Study of 939 Masses 1 Purpose : Methods : Results :. 262(2), 2012.

[13] Kunwar S S Bhatia, Cina S L Tong, Carmen C M Cho, Edmund H Y Yuen, Yolanda Y P Lee, and Anil T Ahuja. Shear wave elastography of thyroid nodules in routine clinical practice: preliminary observations and utility for detecting malignancy. *European radiology*, 22(11):2397–406, November 2012.

[14] C Bouman and K Sauer. A generalized Gaussian image model for edge-preserving MAP estimation. *IEEE transactions on image processing : a publication of the IEEE Signal Processing Society*, 2(3):296–310, January 1993.

[15] C A Bouman and K Sauer. A unified approach to statistical tomography using coordinate descent optimization. *IEEE transactions on image processing : a publication of the IEEE Signal Processing Society*, 5(3):480–92, January 1996.

[16] Chuck Bradley. ACUSON SC2000 Volume Imaging Ultrasound System Retrospective Transmit Beamformation.

[17] David P. Bradway, Peter J. Hollender, Robi Goswami, Patrick D. Wolf, and Gregg E. Trahey. Feasibility and safety of transthoracic cardiac acoustic radiation force impulse imaging methods. In *2012 IEEE International Ultrasonics Symposium*, pages 2027–2030. IEEE, October 2012.

[18] Brett Byram, Gregg E Trahey, and Mark Palmeri. Bayesian speckle tracking. Part I: an implementable perturbation to the likelihood function for ultrasound displacement estimation. *IEEE transactions on ultrasonics, ferroelectrics, and frequency control*, 60(1):132–43, January 2013.

[19] Brett Byram, Gregg E Trahey, and Mark Palmeri. Bayesian speckle tracking. Part II: biased ultrasound displacement estimation. *IEEE transactions on ultrasonics, ferroelectrics, and frequency control*, 60(1):144–157, January 2013.

[20] B. Castaneda, K. Hoyt, K. Westesson, L. An, J. Yao, L. Baxter, J. Joseph, J. Strang, D. Rubens, and K. Parker. Performance of three-dimensional sonoelastography in prostate cancer detection: A comparison between ex vivo and in vivo experiments. *2009 IEEE International Ultrasonics Symposium*, pages 519–522, September 2009.

[21] I. Cespedes, Y. Huang, J. Ophir, and S. Spratt. Methods for Estimation of Subsample Time Delays of Digitized Echo Signals. *Ultrasonic Imaging*, 17(2):142–171, April 1995.

[22] Li-wen Chang, Ke-hsin Hsu, and Pai-chi Li. Graphics processing unit-based high-frame-rate color doppler ultrasound processing. *Ultrasonics, Ferroelectrics and Frequency Control, IEEE Transactions on*, 56(9):1856–1860, September 2009.

[23] Richard S. C. Cobbold. *Foundations of Biomedical Ultrasound.* Oxford University Press, 2006.

[24] D.Ll Cochlin, R.H Ganatra, and D.F.R Griffiths. Elastography in the Detection of Prostatic Cancer. *Clinical Radiology*, 57(11):1014–1020, November 2002.

[25] J-M Correas, a M Tissier, a Khairoune, G Khoury, D Eiss, and O Hélénon. Ultrasound elastography of the prostate: State of the art. *Diagnostic and interventional imaging*, pages 1–10, April 2013.

[26] David O Cosgrove, Wendie A Berg, Caroline J Doré, Danny M Skyba, Jean-Pierre Henry, Joel Gay, and Claude Cohen-Bacrie. Shear wave elastography for breast masses is highly reproducible. *European radiology*, 22(5):1023–32, May 2012.

[27] Jeremy Dahl, Gianmarco Pinton, Mark Palmeri, Vineet Agrawal, Kathryn Nightingale, and Gregg Trahey. A parallel tracking method for acoustic radiation force impulse imaging. *IEEE Transactions on Ultrasonics, Ferroelectrics and Frequency Control*, 54(2):301–312, February 2007.

[28] Jeremy J Dahl, Douglas M Dumont, Jason D Allen, Elizabeth M Miller, and Gregg E Trahey. Acoustic radiation force impulse imaging for noninvasive characterization of carotid artery atherosclerotic plaques: a feasibility study. *Ultrasound in medicine & biology*, 35(5):707–16, May 2009.

[29] Angelo M De Marzo, Elizabeth A Platz, Siobhan Sutcliffe, Jianfeng Xu, Henrik Grönberg, Charles G Drake, Yasutomo Nakai, William B Isaacs, and William G Nelson. Inflammation in prostate carcinogenesis. *Nature reviews. Cancer*, 7(4):256–69, April 2007.

[30] Thomas Deffieux, Jean-Luc Gennisson, Jeremy Bercoff, and Mickael Tanter. On the effects of reflected waves in transient shear wave elastography. *IEEE transactions on ultrasonics, ferroelectrics, and frequency control*, 58(10):2032–5, October 2011.

[31] Joshua R Doherty, Jeremy J Dahl, and Gregg E Trahey. Harmonic tracking of acoustic radiation force-induced displacements. *IEEE transactions on ultrasonics, ferroelectrics, and frequency control*, 60(11):2347–58, November 2013.

[32] Joshua R Doherty, Gregg E Trahey, Kathryn R Nightingale, and Mark L Palmeri. Acoustic radiation force elasticity imaging in diagnostic ultrasound. *IEEE transactions on ultrasonics, ferroelectrics, and frequency control*, 60(4):685–701, April 2013.

[33] Joshua R Doherty, Gregg E Trahey, Kathryn R Nightingale, and Mark L Palmeri. Acoustic Radiation Force Elasticity Imaging in Diagnostic Ultrasound. *IEEE transactions on ultrasonics, ferroelectrics, and frequency control*, in press.

[34] Scott Eggener, Georg Salomon, Peter T Scardino, Jean De la Rosette, Thomas J Polascik, and Simon Brewster. Focal therapy for prostate cancer: possibilities and limitations. *European urology*, 58(1):57–64, July 2010.

[35] Stephanie A Eyerly, Tristram D Bahnson, Jason I Koontz, David P Bradway, Douglas M Dumont, Gregg E Trahey, and Patrick D Wolf. Intracardiac acoustic radiation force impulse imaging: a novel imaging method for intraprocedural evaluation of radiofrequency ablation lesions. *Heart rhythm : the official journal of the Heart Rhythm Society*, 9(11):1855–62, November 2012.

[36] B J Fahey, R C Nelson, D P Bradway, S J Hsu, D M Dumont, and G E Trahey. In vivo visualization of abdominal malignancies with acoustic radiation force elastography. *Physics in Medicine and Biology*, 53(1):279, 2008.

[37] Andriy Fedorov, Reinhard Beichel, Jayashree Kalpathy-Cramer, Julien Finet, Jean-Christophe Fillion-Robin, Sonia Pujol, Christian Bauer, Dominique Jennings, Fiona Fennessy, Milan Sonka, John Buatti, Stephen Aylward, James V Miller, Steve Pieper, and Ron Kikinis. 3D Slicer as an image computing platform for the Quantitative Imaging Network. *Magnetic resonance imaging*, 30(9):1323–41, November 2012.

[38] J Fehrenbach. Influence of Poisson's ratio on elastographic direct and inverse problems. *Physics in medicine and biology*, 52(3):707–16, February 2007.

[39] E. J. Feleppa, C. R. Porter, J. Ketterling, P. Lee, S. Dasgupta, S. Urban, and a. Kalisz. Recent Developments in Tissue-Type Imaging (TTI) for Planning and Monitoring Treatment of Prostate Cancer. *Ultrasonic Imaging*, 26(3):163–172, July 2004.

[40] Ernest J. Feleppa, Jeffrey a. Ketterling, Christopher R. Porter, John Gillespie, Cheng-Shie Wuu, Stella Urban, Andrew Kalisz, Ronald D. Ennis, and Peter B. Schiff. Ultrasonic tissue-type imaging (TTI) for planning treatment of prostate cancer. *Medical Imaging 2004*, 5373:223–230, April 2004.

[41] Ernest J Feleppa, Jonathan Mamou, Christopher R Porter, and Junji Machi. Quantitative ultrasound in cancer imaging. *Seminars in oncology*, 38(1):136–50, February 2011.

[42] Jean-Luc Gennisson, Thomas Deffieux, Emilie Macé, Gabriel Montaldo, Mathias Fink, and Mickaël Tanter. Viscoelastic and anisotropic mechanical properties of in vivo muscle tissue assessed by supersonic shear imaging. *Ultrasound in medicine & biology*, 36(5):789–801, May 2010.

[43] Hongyu Guo, Jianping Dai, and Jinquan Shi. Fast iterative reconstruction method for PROPELLER MRI. In Jianguo Liu, Kunio Doi, Aaron Fenster, and S C Chan, editors, *MIPPR 2009: Medical Imaging, Parallel Processing of Images, and Optimization Techniques*, volume 7497, page 74972O. SPIE, 2009.

[44] Yan Guorui, Tian Jie, Zhu Shouping, Dai Yakang, and Qin Chenghu. Fast cone-beam CT image reconstruction using GPU hardware. *Journal of X-Ray Science & Technology*, 16(4):225–234, 2008.

[45] V E Gusev, A A Karabutov, and K Hendzel. *Laser optoacoustics*. American Institute of Physics, 1993.

[46] Ethan J Halpern, Leonard G Gomella, Flemming Forsberg, Peter a McCue, and Edouard J Trabulsi. Contrast enhanced transrectal ultrasound for the detection of prostate cancer: a randomized, double-blind trial of dutasteride pretreatment. *The Journal of urology*, 188(5):1739–45, November 2012.

[47] Magnus Rudolph Hestenes and Eduard Stiefel. Methods of conjugate gradients for solving linear systems, 1952.

[48] Kenneth Hoyt, Benjamin Castaneda, Man Zhang, Priya Nigwekar, P Anthony di Sant'agnese, Jean V Joseph, John Strang, Deborah J Rubens, and Kevin J Parker. Tissue elasticity properties as biomarkers for prostate cancer. *Cancer biomarkers : section A of Disease markers*, 4(4-5):213–25, January 2008.

[49] H Ito. Visualization of prostate cancer using dynamic contrast-enhanced MRI: comparison with transrectal power Doppler ultrasound. *British Journal of Radiology*, 76(909):617–624, September 2003.

[50] Byunghyun Jang, David Kaeli, Synho Do, and Homer Pien. Multi GPU implementation of iterative tomographic reconstruction algorithms. In *ISBI'09: Proceedings of the Sixth IEEE international conference on Symposium on Biomedical Imaging*, pages 185–188, Piscataway, NJ, USA, 2009. IEEE Press.

[51] J A Jensen and N B Svendsen. Calculation of pressure fields from arbitrarily shaped, apodized, and excited ultrasound transducers. *IEEE transactions on ultrasonics, ferroelectrics, and frequency control*, 39(2):262–7, January 1992.

[52] Kazumi Kamoi, Koji Okihara, Atsushi Ochiai, Osamu Ukimura, Yoichi Mizutani, Akihiro Kawauchi, and Tsuneharu Miki. The utility of transrectal real-time elastography in the diagnosis of prostate cancer. *Ultrasound in medicine & biology*, 34(7):1025–32, July 2008.

[53] Atul Kapoor, Aprajita Kapoor, Goldaa Mahajan, and Bholla Singh Sidhu. Real-time elastography in the detection of prostate cancer in patients with raised PSA level. *Ultrasound in medicine & biology*, 37(9):1374–81, September 2011.

[54] C Kasai, K Namekawa, A Koyano, and R Omoto. Real-Time Two-Dimensional Blood Flow Imaging Using an Autocorrelation Technique. *Sonics and Ultrasonics, IEEE Transactions on*, 32(3):458–464, May 1985.

[55] Gwangseong Kim, Sheng-Wen Huang, Kathleen C Day, Matthew O'Donnell, Rodney R Agayan, Mark A Day, Raoul Kopelman, and Shai Ashkenazi. Indocyanine-green-embedded PEBBLEs as a contrast agent for photoacoustic imaging. *Journal of biomedical optics*, 12(4):044020, January 2007.

[56] Kui Lin, Joyce McLaughlin, Daniel Renzi, and Ashley Thomas. Shear wave speed recovery in sonoelastography using crawling wave data. *The Journal of the Acoustical Society of America*, 128(1):88–97, July 2010.

[57] Frederic L. Lizzi, Michael Greenebaum, Ernest J. Feleppa, Marek Elbaum, and D. Jackson Coleman. Theoretical framework for spectrum analysis in ultrasonic tissue characterization. *The Journal of the Acoustical Society of America*, 73(4):1366, April 1983.

[58] T Loupas, J T Powers, and R W Gill. An axial velocity estimator for ultrasound blood flow imaging, based on a full evaluation of the Doppler equation by means of a two-dimensional autocorrelation approach. *Ultrasonics, Ferroelectrics and Frequency Control, IEEE Transactions on*, 42(4):672–688, July 1995.

[59] Sara Mahdavi, Mehdi Moradi, Xu Wen, William J Morris, and Septimiu E Salcudean. Evaluation of visualization of the prostate gland in vibro-elastography images. *Medical image analysis*, 15(4):589–600, August 2011.

[60] Roberta Mazzucchelli, Francesca Barbisan, Marina Scarpelli, Antonio Lopez-Beltran, Theodorus H van der Kwast, Liang Cheng, and Rodolfo Montironi. Is incidentally detected prostate cancer in patients undergoing radical cystoprostatectomy clinically significant? *American journal of clinical pathology*, 131(2):279–83, February 2009.

[61] S. A. McAleavey, M. Menon, and J. Orszulak. Shear-Modulus Estimation by Application of Spatially-Modulated Impulsive Acoustic Radiation Force. *Ultrasonic Imaging*, 29(2):87–104, April 2007.

[62] Joyce McLaughlin and Daniel Renzi. Shear wave speed recovery in transient elastography and supersonic imaging using propagating fronts. *Inverse Problems*, 22(2):681–706, April 2006.

[63] J E McNeal. Cancer volume and site of origin of adenocarcinoma in the prostate: relationship to local and distant spread. *Human pathology*, 23(3):258–66, March 1992.

[64] J V Miller, J B Farison, and Y Shin. Spatially invariant image sequences. *IEEE transactions on image processing : a publication of the IEEE Signal Processing Society*, 1(2):148–61, January 1992.

[65] Michael Josef Mitterberger, Friedrich Aigner, Wolfgang Horninger, Hanno Ulmer, Silvio Cavuto, Ethan J Halpern, and Ferdinand Frauscher. Comparative efficiency of contrast-enhanced colour Doppler ultrasound targeted versus systematic biopsy for prostate cancer detection. *European radiology*, 20(12):2791–6, December 2010.

[66] Tomoaki Miyagawa, Masakazu Tsutsumi, Takeshi Matsumura, Natsui Kawazoe, Satoru Ishikawa, Tatsuro Shimokama, Naoto Miyanaga, and Hideyuki Akaza. Real-time elastography for the diagnosis of prostate cancer: evaluation of elastographic moving images. *Japanese journal of clinical oncology*, 39(6):394–8, June 2009.

[67] Naoto Miyanaga, Hideyuki Akaza, Makoto Yamakawa, Takehiro Oikawa, Noritoshi Sekido, Shiro Hinotsu, Koji Kawai, Toru Shimazui, and Tsuyoshi Shiina. Tissue elasticity imaging for diagnosis of prostate cancer: a preliminary report. *Int J Urol*, 13(12):1514–1518, December 2006.

[68] Marie Muller, Jean-Luc Gennisson, Thomas Deffieux, Mickaël Tanter, and Mathias Fink. Quantitative viscoelasticity mapping of human liver using supersonic shear imaging: preliminary in vivo feasibility study. *Ultrasound in medicine & biology*, 35(2):219–29, February 2009.

[69] Eric D Nelson, Craig B Slotoroff, Leonard G Gomella, and Ethan J Halpern. Targeted biopsy of the prostate: the impact of color Doppler imaging and elastography on prostate cancer detection and Gleason score. *Urology*, 70(6):1136–40, December 2007.

[70] K R Nightingale, M Palmeri, R Nightingale, and G Trahey. On the feasibility of remote palpation using acoustic radiation force. *J Acoust Soc Am*, 110:625–634, 2001.

[71] K R Nightingale, M L Palmeri, and G E Trahey. Analysis of contrast in images generated with transient acoustic radiation force. *Ultrasound Med Biol*, 32:61–72, 2006.

[72] K R Nightingale, M Soo, R Nightingale, and G E Trahey. Acoustic radiation force impulse imaging: In vivo demonstration of clinical feasibility. *Ultrasound Med Biol*, 28:227–235, 2002.

[73] W L M Nyborg, T Litovitz, and C Davis. Acoustic Streaming. In W P Mason, editor, *Physical Acoustics*, volume IIA, chapter 11, pages 265–331. Academic Press Inc, New York, 1965.

[74] T E Oliphant, A Manduca, R L Ehman, and J F Greenleaf. Complex-valued stiffness reconstruction for magnetic resonance elastography by algebraic inversion of the differential equation. *Magnetic resonance in medicine : official journal of the Society of Magnetic Resonance in Medicine / Society of Magnetic Resonance in Medicine*, 45(2):299–310, February 2001.

[75] J Ophir. Elastography: A quantitative method for imaging the elasticity of biological tissues. *Ultrasonic Imaging*, 13(2):111–134, April 1991.

[76] Alexander Oraevsky and A Karabutov. Optoacoustic tomography. *Biomedical photonics handbook*, pages 31–34, 2003.

[77] Leo Pallwein, Fritz Aigner, Ralph Faschingbauer, Eva Pallwein, Germar Pinggera, Georg Bartsch, Georg Schaefer, Peter Struve, and Ferdinand Frauscher. Prostate cancer diagnosis: value of real-time elastography. *Abdominal imaging*, 33(6):729–35, 2008.

[78] Leo Pallwein, Michael Mitterberger, Alexandre Pelzer, Georg Bartsch, Hannes Strasser, Germar M Pinggera, Friedrich Aigner, Johann Gradl, Dieter Zur Nedden, and Ferdinand Frauscher. Ultrasound of prostate cancer: recent advances. *European radiology*, 18(4):707–15, April 2008.

[79] Leo Pallwein, Michael Mitterberger, Germar Pinggera, Friedrich Aigner, Florian Pedross, Johann Gradl, Alexandre Pelzer, Georg Bartsch, and Ferdinand Frauscher. Sonoelastography of the prostate: comparison with systematic biopsy findings in 492 patients. *European journal of radiology*, 65(2):304–10, February 2008.

[80] M L Palmeri, A C Sharma, R R Bouchard, R W Nightingale, and K R Nightingale. A finite-element method model of soft tissue response to impulsive acoustic radiation force. *Ultrasonics, Ferroelectrics and Frequency Control, IEEE Transactions on*, 52(10):1699–1712, 2005.

[81] M L Palmeri, M H Wang, J J Dahl, K D Frinkley, and K R Nightingale. Quantifying hepatic shear modulus in vivo using acoustic radiation force. *Ultrasound in medicine & biology*, 34(4):546–58, April 2008.

[82] M L Palmeri, M H Wang, J J Dahl, K D Frinkley, K R Nightingale, and L Zhai. Quantifying Hepatic Shear Modulus In Vivo Using Acoustic Radiation Force. *Ultrasound Med Biol*, 34(4):546–558, April 2008.

[83] Mark L Palmeri, Jeremy J Dahl, David B MacLeod, Stuart A Grant, and Kathryn R Nightingale. On the feasibility of imaging peripheral nerves using acoustic radiation force impulse imaging. *Ultrasonic imaging*, 31(3):172–82, July 2009.

[84] Mark L Palmeri, Stephen A McAleavey, Gregg E Trahey, and Kathryn R Nightingale. Ultrasonic tracking of acoustic radiation force-induced displacements in homogeneous media. *IEEE transactions on ultrasonics, ferroelectrics, and frequency control*, 53(7):1300–1313, July 2006.

[85] Mark L Palmeri, Student Member, Amy C Sharma, Richard R Bouchard, Roger W Nightingale, and Kathryn R Nightingale. A Finite-Element Method Model of Soft Tissue Force. *IEEE transactions on ultrasonics, ferroelectrics, and frequency control*, 52(10):1699–1712, 2005.

[86] Mark L Palmeri, Zachary A Miller, Tyler J Glass, Kirema Garcia-Reyesy, Rajan T Gupta, Stephen J Rosenzweig, Christopher Kauffman, Thomas J Polascik, Andrew Buck, Samantha L Lipman, Ned C Rouze, and Kathryn R Nightingale. B-mode and Acoustic Radiation Force Impulse (ARFI) Imaging of Prostate Zonal Anatomy: Comparison with 3T T2-Weighted MR Imaging (T2WI). *Ultrasonic Imaging*, in press.

[87] K J Parker, M M Doyley, and D J Rubens. Imaging the elastic properties of tissue: the 20 year perspective. *Physics in Medicine and Biology*, 56(2):513–513, February 2011.

[88] A Pesavento, C Perrey, M Krueger, and H Ermert. A time-efficient and accurate strain estimation concept for ultrasonic elastography using iterative phase zero estimation. *IEEE transactions on ultrasonics, ferroelectrics, and frequency control*, 46(5):1057–67, January 1999.

[89] G F Pinton, J J Dahl, and G E Trahey. Rapid tracking of small displacements with ultrasound. *IEEE Trans Ultrason, Ferroelect, Freq Contr*, 53:1103–1117, 2006.

[90] William H Press, Saul A Teukolsky, William T Vetterling, and Brian P Flannery. Numerical Recipes in C: The Art of Scientific Computing. Second Edition, 1992.

[91] Stephen Rosenzweig, Mark Palmeri, and Kathryn Nightingale. GPU-based real-time small displacement estimation with ultrasound. *IEEE transactions on ultrasonics, ferroelectrics, and frequency control*, 58(2):399–405, February 2011.

[92] Stephen Rosenzweig, Mark Palmeri, Ned Rouze, Samantha Lipman, Evan Kulbacki, John Madden, Thomas Polascik, and Kathryn Nightingale. Comparison

of Concurrently Acquired In Vivo 3D ARFI and SWEI Images of the Prostate. In *IEEE Ultrasonics Symposium*, pages 97–100, 2012.

[93] Veronica Rotemberg, Mark L Palmeri, Ned C Rouze, Roger Nightingale, and Kathryn R Nightingale. Comparison between Acoustic Radiation Force Impulse (ARFI)-based hepatic stiffness quantification in deformed and undeformed pressurized canine livers. In *2011 IEEE International Ultrasonics Symposium*, pages 2090–2093. IEEE, October 2011.

[94] Ned C Rouze, Michael H Wang, Mark L Palmeri, and Kathryn R Nightingale. Robust estimation of time-of-flight shear wave speed using a radon sum transformation. *IEEE transactions on ultrasonics, ferroelectrics, and frequency control*, 57(12):2662–70, December 2010.

[95] Ned C Rouze, Michael H Wang, Mark L Palmeri, and Kathryn R Nightingale. Parameters affecting the resolution and accuracy of 2-D quantitative shear wave images. *IEEE transactions on ultrasonics, ferroelectrics, and frequency control*, 59(8):1729–40, August 2012.

[96] S E Salcudean, Daniel French, S Bachmann, R Zahiri-Azar, X Wen, and W J Morris. Viscoelasticity modeling of the prostate region using vibro-elastography. *Medical image computing and computer-assisted intervention : MICCAI ... International Conference on Medical Image Computing and Computer-Assisted Intervention*, 9(Pt 1):389–96, January 2006.

[97] G Salomon, J Kollerman, I Thederan, F Chun, L Budaus, T Schlomm, H Isbarn, H Heinzer, H Huland, and M Graefen. Evaluation of Prostate Cancer Detection with Ultrasound Real-Time Elastography: A Comparison with Step Section Pathological Analysis after Radical Prostatectomy. *European Urology*, 2008.

[98] A P Sarvazyan, O V Rudenko, S D Swanson, J B Fowlkes, and S Y Emelianov. Shear wave elasticity imaging: a new ultrasonic technology of medical diagnostics. *Ultrasound in medicine & biology*, 24(9):1419–35, November 1998.

[99] Thomas Schiwietz, Ti-chiun Chang, Peter Speier, and Rüdiger Westermann. MR image reconstruction using the GPU. In Michael J Flynn and Jiang Hsieh, editors, *Medical Imaging 2006: Physics of Medical Imaging*, volume 6142, page 61423T. SPIE, 2006.

[100] A C Sharma, M S Soo, G E Trahey, K R Nightingale, and A N Congdon. Acoustic Radiation Force Impulse (ARFI) imaging of in vivo breast masses. In *IEEE Ultrasonics,Ferroelectrics and Frequency Control Joint Symposium*, number 1, pages 728–731, 2004.

[101] Amy Sharma, Gregg Trahey, Kristin Frinkley, Mary Scott Soo, Mark Palmeri, and Kathryn Nightingale. Image processing and data acquisition optimization for Acoustic Radiation Force Impulse imaging of in vivo breast masses. In William F. Walker and Stanislav Y. Emelianov, editors, *SPIE Proceedings: Medical Imaging*, pages 205–215. International Society for Optics and Photonics, April 2005.

[102] G C Sharp, N Kandasamy, H Singh, and M Folkert. GPU-based streaming architectures for fast cone-beam CT image reconstruction and demons deformable registration. *Physics in Medicine and Biology*, 52(19):5771, 2007.

[103] Siemens. Echo Made Easy. Results You Can Trust. ACUSON SC2000 Ultrasound System.

[104] J Tang, JC Yang, and Y Li. Peripheral Zone Hypoechoic Lesions of the Prostate Evaluation With Contrast-Enhanced Gray Scale Transrectal Ultrasonography. *Journal of ultrasound in medicine : official journal of the American Institute of Ultrasound in Medicine*, pages 1671–1679, 2007.

[105] Mickael Tanter, Jeremy Bercoff, Alexandra Athanasiou, Thomas Deffieux, Jean-Luc Gennisson, Gabriel Montaldo, Marie Muller, Anne Tardivon, and Mathias Fink. Quantitative assessment of breast lesion viscoelasticity: initial clinical results using supersonic shear imaging. *Ultrasound in medicine & biology*, 34(9):1373–86, September 2008.

[106] Lawrence S Taylor, Deborah J Rubens, Brian C Porter, Zhe Wu, Raymond B Baggs, P Anthony, Sant Agnese, Gyongyi Nadasdy, David Pasternack, Edward M Messing, Priya Nigwekar, and Kevin J Parker. Radiology Prostate Cancer : Sonoelastography for in Vitro. (2):981–985, 2005.

[107] G R Torr. The Acoustic Radiation Force. *Am. J. Phys.*, 52:402–408, 1984.

[108] Masakazu Tsutsumi and Tomoaki Miyagawa. Real-time balloon inflation elastography for prostate cancer detection and initial evaluation of clinicopathologic analysis. *American Journal of Roentgenology*, (June):471–476, 2010.

[109] Masakazu Tsutsumi, Tomoaki Miyagawa, Takeshi Matsumura, Natsui Kawazoe, Satoru Ishikawa, Tatsuro Shimokama, Tsuyoshi Shiina, Naoto Miyanaga, and Hideyuki Akaza. The impact of real-time tissue elasticity imaging (elastography) on the detection of prostate cancer: clinicopathological analysis. *Int J Clin Oncol*, 12(4):250–255, August 2007.

[110] Emre Turgay, Septimiu Salcudean, and Robert Rohling. Identifying the mechanical properties of tissue by ultrasound strain imaging. *Ultrasound in medicine & biology*, 32(2):221–35, February 2006.

[111] W Walker and G Trahey. A Fundamental Limit on Delay Estimation Using Partially Correlated Speckle Signals. *IEEE Trans. Ultrason.,Ferroelec.,Freq. Contr.*, 42(2):301–308, 1995.

[112] Michael H Wang, Mark L Palmeri, Veronica M Rotemberg, Ned C Rouze, and Kathryn R Nightingale. Improving the robustness of time-of-flight based shear wave speed reconstruction methods using RANSAC in human liver in vivo. *Ultrasound in medicine & biology*, 36(5):802–13, May 2010.

[113] Michael H Wang, Mark L Palmeri, Veronica M Rotemberg, Ned C Rouze, and Kathryn R Nightingale. Improving the robustness of time-of-flight based shear wave speed reconstruction methods using RANSAC in human liver in vivo. *Ultrasound in medicine & biology*, 36(5):802–13, May 2010.

[114] Xueding Wang, William W Roberts, Paul L Carson, David P Wood, and J Brian Fowlkes. Photoacoustic tomography: a potential new tool for prostate cancer. *Biomedical optics express*, 1(4):1117, 2010.

[115] D.G. Wildes, R.Y. Chiao, C.M.W. Daft, K.W. Rigby, L.S. Smith, and K.E. Thomenius. Elevation performance of 1.25D and 1.5D transducer arrays. *IEEE Transactions on Ultrasonics, Ferroelectrics and Frequency Control*, 44(5):1027–1037, September 1997.

[116] Fang Xu and Klaus Mueller. Real-time 3D computed tomographic reconstruction using commodity graphics hardware. *Physics in Medicine and Biology*, 52(12):3405, 2007.

[117] Liang Zhai, Jeremy Dahl, John Madden, Vladimir Mouraviev, Thomas Polascik, Mark Palmeri, and Kathryn Nightingale. Three-dimensional acoustic radiation force impulse (ARFI) imaging of human prostates in vivo. *2008 IEEE Ultrasonics Symposium*, pages 540–543, November 2008.

[118] Liang Zhai, John Madden, Wen-Chi Foo, Vladimir Mouraviev, Thomas J Polascik, Mark L Palmeri, and Kathryn R Nightingale. Characterizing stiffness of human prostates using acoustic radiation force. *Ultrasonic Imaging*, 32(4):201–213, 2010.

[119] Liang Zhai, John Madden, Wen-Chi Foo, Mark L Palmeri, Vladimir Mouraviev, Thomas J Polascik, and Kathryn R Nightingale. Acoustic radiation force impulse imaging of human prostates ex vivo. *Ultrasound in medicine & biology*, 36(4):576–88, April 2010.

[120] Liang Zhai, John Madden, Vladimir Mouraviev, Thomas Polascik, and Kathryn Nightingale. Correlation Between SWEI and ARFI Image Findings in ex vivo Human Prostates. pages 523–526, 2009.

[121] Liang Zhai, Thomas J Polascik, Wen-Chi Foo, Stephen Rosenzweig, Mark L Palmeri, John Madden, and Kathryn R Nightingale. Acoustic radiation force impulse imaging of human prostates: initial in vivo demonstration. *Ultrasound in medicine & biology*, 38(1):50–61, January 2012.

[122] Man Zhang, Priya Nigwekar, Benjamin Castaneda, Kenneth Hoyt, Jean V Joseph, Anthony di Sant'Agnese, Edward M Messing, John G Strang, Deborah J Rubens, and Kevin J Parker. Quantitative characterization of viscoelastic properties of human prostate correlated with histology. *Ultrasound in medicine & biology*, 34(7):1033–42, July 2008.

[123] Q Zhang, X Huang, R Eagleson, G Guiraudon, and T M Peters. Real-time dynamic display of registered 4D cardiac MR and ultrasound images using a GPU. In Kevin R Cleary and Michael I Miga, editors, *Medical Imaging 2007: Visualization and Image-Guided Procedures*, volume 6509, page 65092D. SPIE, 2007.

[124] Heng Zhao, Pengfei Song, Armando Manduca, Randall R. Kinnick, Matthew W. Urban, James F. Greenleaf, Shigao Chen, and Stefan Catheline. Two-dimensional shear elasticity imaging using external mechanical vibration. In *2013 IEEE International Ultrasonics Symposium (IUS)*, pages 1256–1259. IEEE, July 2013.

[125] Mingchang Zhao and Shanjue Mo. A GPU based high-definition ultrasound digital scan conversion algorithm. In Kenneth H Wong and Michael I Miga, editors, *Medical Imaging 2010: Visualization, Image-Guided Procedures, and Modeling*, volume 7625, page 76252M. SPIE, 2010.

Biography

Name Stephen Rosenzweig
Date and Place of Birth July 22, 1986 New York City, NY
Degrees Earned B.S.E. Biomedical Engineering and Mathematics, Duke University

Awards and Fellowships

1. James B. Duke Fellowship
2. NIH Training Grant Fellow (T32-EB-001040)
3. Thurstone Medical Imaging Fellowship

Publications

1. G. F. Pinton, J. J. Dahl, S. J. Rosenzweig, and G. E. Trahey, A heterogeneous nonlinear attenuating full-wave model of ultrasound., IEEE Trans Ultrason Ferroelectr Freq Control, vol. 56, no. 3, pp. 474488, Mar. 2009.
2. G. P. Howles, K. F. Bing, Y. Qi, S. J. Rosenzweig, K. R. Nightingale, and G. A. Johnson, Contrast-enhanced in vivo magnetic resonance microscopy of the mouse brain enabled by noninvasive opening of the blood-brain barrier with ultrasound., Magnetic resonance in medicine: official journal of the Society of Magnetic Resonance in Medicine / Society of Magnetic Resonance in Medicine, vol. 64, no. 4, pp. 9951004, Oct. 2010.
3. V. Rotemberg, M. Palmeri, S. Rosenzweig, S. Grant, D. Macleod, and K. Nightingale, Acoustic Radiation Force Impulse (ARFI) Imaging-Based Needle Visualization, Ultrasonic Imaging, vol. 33, no. 1, pp. 116, Jan. 2011.
4. Rosenzweig SJ, Palmeri, ML, Nightingale KR. GPU-Based Real-Time Displacement Estimation for Acoustic Radiation Force Impulse (ARFI) Images, IEEE UFFC, 58:399-405, 2011.
5. L. Zhai, T. J. Polascik, W.-C. Foo, S. Rosenzweig, M. L. Palmeri, J. Madden, and K. R. Nightingale, Acoustic radiation force impulse imaging of human prostates: initial in vivo demonstration., Ultrasound in medicine & biology, vol. 38, no. 1, pp. 5061, Jan. 2012.

6. G. P. Howles, Y. Qi, S. J. Rosenzweig, K. R. Nightingale, and G. A. Johnson, Functional neuroimaging using ultrasonic blood-brain barrier disruption and manganese-enhanced MRI., Journal of visualized experiments : JoVE, no. 65, p. e4055, Jan. 2012.
7. Palmeri ML, Miller ZA, Glass TJ, Garcia-Reyes K, Gupta RT, Rosenzweig SJ, Kauffman C, Polascik TJ, Buck A, Passoni N, Lipman SLL, Rouze NC, Nightingale KR. Acoustic Radiation Force Impulse (ARFI) Imaging Prostate Zonal Anatomy: Comparison with 3T T2-Weighted MR Imaging (T2WI)., Ultrasonic Imaging, in press.
8. Nightingale K, Rouze N, Rosenzweig S, Wang M, Abdelmalek M, Palmeri M. Derivation and Analysis of Viscoelastic Properties in Human Liver: Impact of Frequency on Fribrosis and Steatosis Staging., IEEE UFFC, in review.
9. Rosenzweig SJ, Palmeri ML, Nightingale KR. ”Analysis of Rapid Multi-Focal Zone ARFI Imaging.,” IEEE UFFC, in submission.